UNIVERSITÀ DEGLI STUDI DI PADOVA

Dipartimento di Fisica e Astronomia "Galileo Galilei"

Master Degree in Physics

Final Dissertation

Study of H→WW reconstruction and coupling precision determination at Muon Collider

Thesis supervisor

Prof. Donatella Lucchesi

Thesis co-supervisor

Dr. Lorenzo Sestini

Candidate

Luca Castelli

Academic Year 2021/2022

Contents

Chapter 1

Introduction

1.1 Overview of the thesis

The purpose of this thesis is the study of the single Higgs boson production at Muon Collider at a center of mass energy of 3 TeV. The Higgs boson is reconstructed via the decay into two W bosons. In particular it will be considered the following channel:

$$\mu^+\mu^- \to H + X \to W^*W + X \to qq\mu\nu + X,\ \sqrt{s} = 3\ TeV \tag{1.1}$$

The Higgs boson, discovered in 2012 at the Large Hadron Collider (LHC), still has many aspects unknown. It has to be proven that it is the particle predicted by the Standard Model (SM), therefore experimental measurements of its properties are needed. In particular, it is important to measure the coupling constants, i.e. the parameters that determine the strength of the interaction of the Higgs boson with SM bosons and fermions that are the elementary constituents of matter. In addition, the determination of the self-couplings which determine the shape of the Higgs Boson potential, will shed light on New Physics. In order to accomplish this research program, it is necessary to investigate the multi-TeV energy scale.

LHC and its upgrade HL-LHC will not be able to perform all these measurements with the necessary precision, therefore a next-generation of particle accelerators are needed.

Among the projects currently under studies, the Muon Collider represents a unique machine which is able to provide lepton collisions at energies of several TeV.

In this thesis the study on the precision achievable on the measurement on the cross section $\sigma(\mu^+\mu^- \to H + X \to WW^* + X \to qq\mu\nu + X)$ is presented.

This measurement, combined with the measurement of the Higgs boson width Γ_H, will allow to determine the precision on the coupling constant of the Higgs boson to the W boson.

The thesis is organized as follow:

- In Chapter 2 a theoretical introduction on Higgs physics will be given. The measurements available as of today at the existing colliders will be presented. The physics goals of future colliders will be discussed with a focus on the Muon Collider.

- Chapter 3 will illustrate the Muon Collider project including the accelerator complex and its challenges.

- In Chapter 4 the detector will be presented as used in this thesis.

- Chapter 5 will discuss the Beam Induced Background, which is one of main issues to be faced by the Muon Collider detector design. Strategies to mitigate the effects of the beam-induced background are also presented.

- In Chapter 6 simulation tools and reconstruction algorithms will be described including the effects of the beam-induced-background.

- Chapter 7 concerns the study of the $H \to WW^*$ process at the Muon Collider, in particular the kinematics and spatial characteristics of the events will be compared to those of the physical backgrounds, in order to define the observables that provide the best discrimination.
- Chapter 8 describes the multivariate analysis performed to estimate the precision on the measurement of the cross section $\sigma(\mu^+\mu^- \to H + X \to WW^* + X)$ at the Muon Collider.
- In Chapter 9 the analysis performed in this thesis is summarized and the estimation of the precision on the measurement of the cross section $\sigma(\mu^+\mu^- \to H + X \to WW^* + X)$ is compared to the result obtained by other future accelerator projects.

Chapter 2

Physics case

2.1 Higgs physics in the Standard Model

The Standard Model (SM) is the theory which describes quantum-mechanically three of the four fundamental interaction: electromagnetic, weak, strong and gravity. According to the SM the particles interact via vector bosons which are the force carriers: photons γ for electromagnetic interaction, $W^{\pm}$ and Z bosons for weak interaction and gluons g for strong interaction.

The mathematical description is based on the gauge symmetry $SU(3)_C \times SU(2)_L \times U(1)_Y$. The first group concerns the strong interaction, while $SU(2))_L \times U(1)_Y$ is related to the electro-weak interaction and it is spontaneously broken by the higgs mechanism (SSB).[1] This is a key concept because it is responsible for the mass of elementary particles and the flavor mixing. Thus, a careful study on the Higgs boson and its interaction with the other particles is crucial to understand the SM and to find evidences of new physics.

The Higgs Boson is added to the SM through its lagrangian:

$$\mathcal{L}_{Higgs} = (D^{\mu}\Phi)^{\dagger} D_{\mu}\Phi - V(\phi) \tag{2.1}$$

Where Φ is Higgs doublet defined as

$$\Phi = \frac{1}{\sqrt{2}} \begin{pmatrix} \phi_1 + i\phi_2 \\ \phi_3 + i\phi_4 \end{pmatrix} \tag{2.2}$$

with ϕ_i real scalar fields. D_{μ} is the covariant derivative:

$$D_{\mu} = \partial_{\mu} + \frac{i}{2} g \tau_j W_{\mu}^{j} + \frac{i}{2} g' B_{\mu},\ j = 1,\ 2,\ 3 \tag{2.3}$$

with τ_j the Pauli matrices, g and g' are the coupling constants related respectively to $SU(2)_L$ and $U(1)_Y$ gauge symmetry, W_{μ}^{j} and B_{μ} are the gauge fields and $V(\Phi)$ is the Higgs potential, defined as:

$$V(\Phi) = \mu^2 \Phi^{\dagger}\Phi + \lambda(\Phi^{\dagger}\Phi)^2 \tag{2.4}$$

with λ and μ parameters of the theory. To require the stability of the vacuum state, $\lambda > 0$ is a necessary condition, while to not have a vacuum expectation value equal to zero, it need to be $\mu^2 < 0$. Thus, the Higgs potential assume the shape reported in figure 2.1. It is clear that there is not an uniquely defined minimum for the potential, but an infinite set of values that differ by a phase. By choosing a particular state as the minimum, the symmetry is spontaneously broken. The ground state doublet is:

$$\langle \Phi \rangle = \frac{1}{\sqrt{2}} \begin{pmatrix} 0 \\ \upsilon \end{pmatrix} \tag{2.5}$$

where

$$\upsilon = \sqrt{\frac{-\mu^2}{\lambda}} \tag{2.6}$$

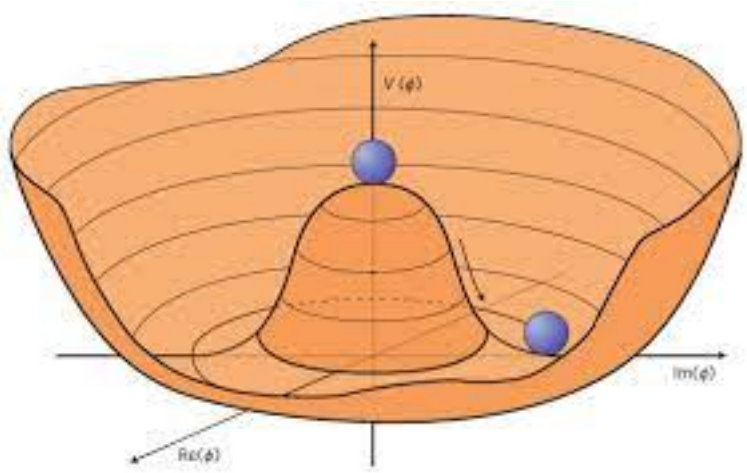

Figure 2.1: Higgs potential, picture taken from [2]

Then, the Higgs field can be expressed as its expansion around the minimum:

$$\langle \Phi \rangle = \frac{1}{\sqrt{2}} \begin{pmatrix} 0 \\ v + h(x) \end{pmatrix} \tag{2.7}$$

with $h(x)$ the real scalar field of the Higgs Boson. [3] By rewriting equation 2.1 using equation 2.7 it becomes:

$$\mathcal{L}_{Higgs} = \frac{1}{2}\partial_\mu h \partial^\mu h + (v+h)^2 \left[\frac{g^2}{4} W_\mu^\dagger W^\mu + \frac{(g^2+g'^2)}{8} Z_\mu^\dagger Z^\mu \right] - \lambda v^2 h^2 - \lambda v h^3 - \frac{\lambda}{4} h^4 \tag{2.8}$$

In this equation, there are the physical fields corresponding the bosons, that can be expressed as combination of gauge ones. After SSB several terms can be individuated in equation 2.8, starting from the masses of the bosons:

$$m_{W^\pm} = \frac{gv}{2} \tag{2.9}$$

$$m_Z = \frac{v}{2}\sqrt{g^2+g'^2} \tag{2.10}$$

$$m_H = \sqrt{2\lambda v^2} \tag{2.11}$$

And the coupling constants of interactions between higgs and vector bosons:

$$g_{HWW} = \frac{g^2}{2} v \tag{2.12}$$

that is the object of this thesis,

$$g_{HZZ} = \frac{g^2+g'^2}{4} v \tag{2.13}$$

$$g_{HHWW} = \frac{g^2}{4} \tag{2.14}$$

$$g_{HHZZ} = \frac{g^2+g'^2}{8} \tag{2.15}$$

And the last two terms of equation 2.8 are the trilinear and quadrilineaer higgs self-interaction terms.

The SSB of the Higgs field gives mass also to quarks and charged lepton. The detailed description can be found in [4].

So far, a theoretical expression of some physical quantities has been given. In the next sections, the measurement done is summarized and then a panoramic of what could be measure in future colliders is given.

Measuring the coupling constants and the Higgs potential with high precision is crucial to verify the Standard Model predictions and to put constrains on new physics. In fact, the couplings are

fully determine within the SM, therefore deviations would be evidence of physics beyond the SM. The investigation of the Higgs potential is even more interesting because it can reveal the nature of the Higgs sector, explaining the reasons behind the SSB, and it can give evidence of new physics as well [5].

2.2 Higgs physics at present colliders

The discover of the Higgs boson at LHC were announced in July, 2012. It was just the beginning of several studies which aim is to find answers to many open questions about the Higgs itself. To understand the Higgs boson is necessary to investigate its properties and how it interacts with other particles.

In this section a panoramic of the measurements performed and their precision on the parameters described above is given.

For the purpose of this thesis it is interesting to deepen the discussion on the coupling measurement performed at LHC, in particular by ATLAS and CMS collaboration.

First of all, it is important to underline how the Higgs boson can be produced at a colliders. There are five production processes: gluon fusion (ggF), vector boson fusion (VBF), associated production with vector bosons (WH and ZH) and top quarks (ttH). Their cross section depends on the kind of collider and on the center-of-mass energy of the collision. At LHC, the most relevant process is the gluon fusion, as it can be seen in figure 2.4 [6].

In figure 2.2 the results obtained for the μ parameter, called "signal strength modifier" defined as follow are shown:

$$\mu_i^f = \frac{\sigma_i BR^f}{(\sigma_i BR^f)_{SM}} \tag{2.16}$$

and it is computed for specif processes $i \to H \to f$, where $i \to H$ is the Higgs production method, with σ_i its cross section, and $H \to f$ is the decay channel, with BR^f its branching ratio. $(\sigma_i)_{SM}$ and $(BR_i)_{SM}$ are the correspondent SM expectation values. The production process studied are the ones mentioned above, while the decay channels are clearly reported in figure 2.2. The equation 2.16 can be rewritten in the so-called κ-framework as follow:

$$\mu_i^f = \frac{\kappa_i^2 \kappa_f^2}{\kappa_H^2} \tag{2.17}$$

where κ are called "coupling modifier" and they are defined in this way:

$$\begin{aligned} \kappa_i^2 &= \frac{\sigma_i}{(\sigma_i)_{SM}} \\ \kappa_f^2 &= \frac{\Gamma_f}{(\Gamma_f)_{SM}} \\ \kappa_H^2 &= \frac{\sum_f \Gamma_f}{(\Gamma_H)_{SM}} \end{aligned} \tag{2.18}$$

with Γ_f the partial decay with of the final state f and Γ_H the Higgs total width.

In this formalism, it became:

$$\sigma_i BR_f = \frac{\kappa_i^2 \kappa_f^2}{\kappa_H^2} (\sigma_i BR_f)_{SM} \tag{2.19}$$

and so the deviation from the SM are given by the κ factors. The results obtained by ATLAS and CMS, together with the expectation for HL-LHC are shown in figure 2.3.

These results show that LHC allows measurement with precision of few % at HL-LHC on several parameters. The goal is to reach the precision of 1% on the couplings, therefore HL-LHC is not enough. Also, it will be challenging to study the Higgs self-coupling. Figure 2.4 helps to understand why: at $\sqrt{s} = 14\ TeV$ proton-proton interactions, the double Higgs production cross section is suppressed by three order of magnitude with respect to the single Higgs, therefore the expected number of events is too small to measure couplings [6]. This is the reason why new facility which will allow a precise measurement of the Higgs self-interaction are needed.

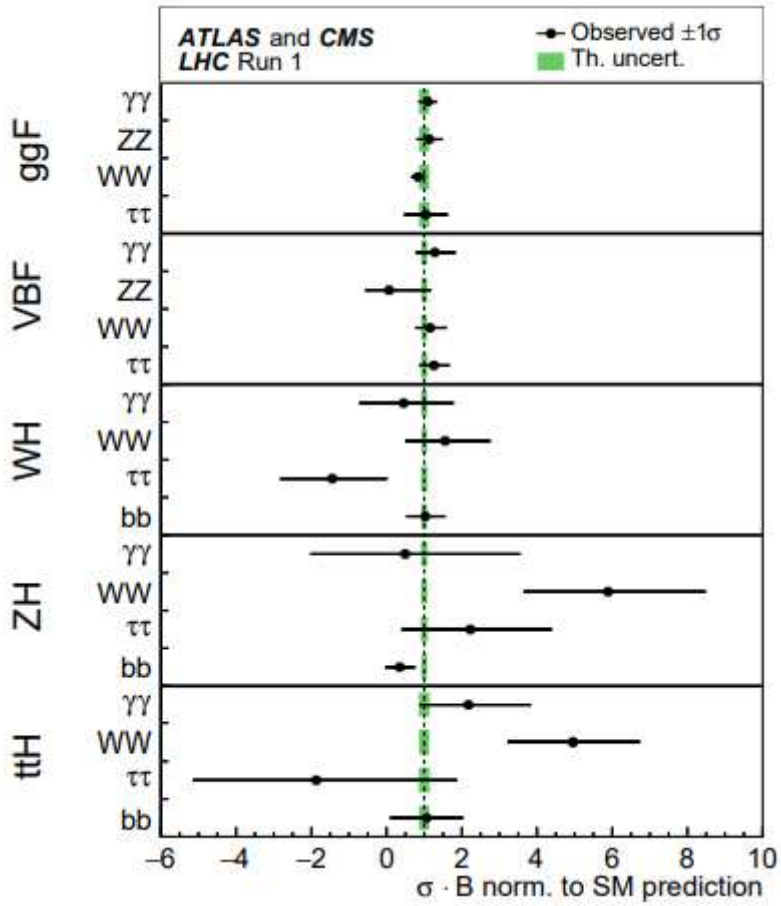

Figure 2.2: ATLAS and CMS measurements and predictions on the signal strength modifiers. Plot from [7]

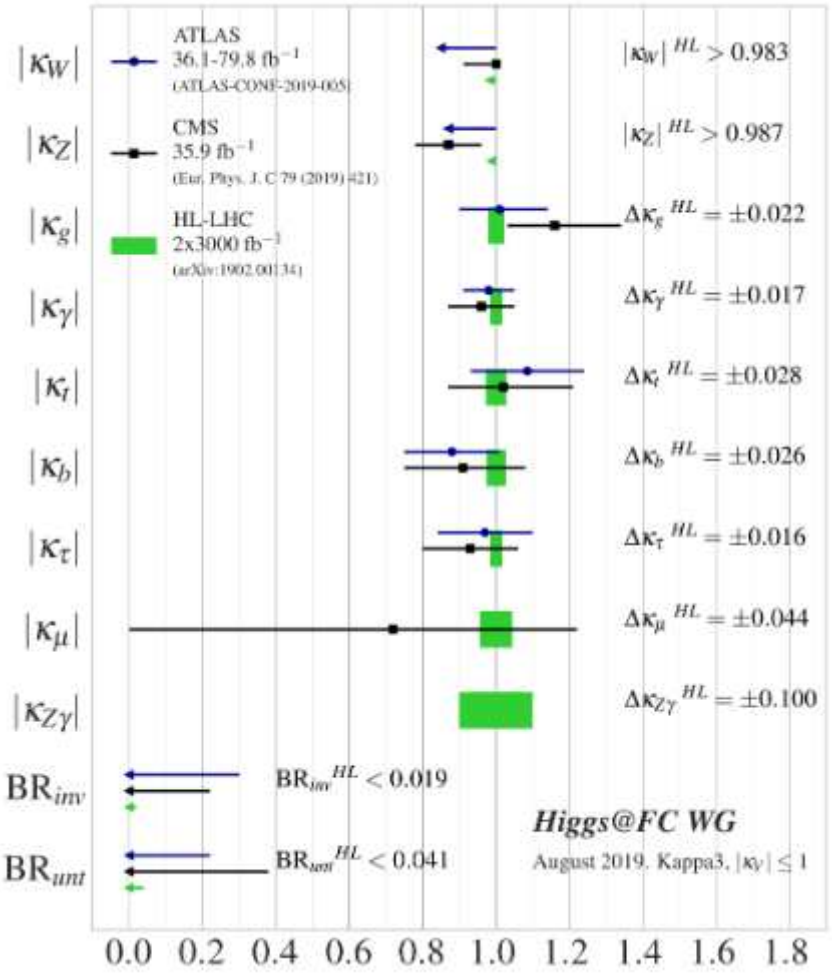

Figure 2.3: ATLAS (blue) and CMS (black) relative precision on κ parameters and constrains on BR_{inv} and BR_{unt} compared to the expected values for HL-LHC. Plot taken from [8]

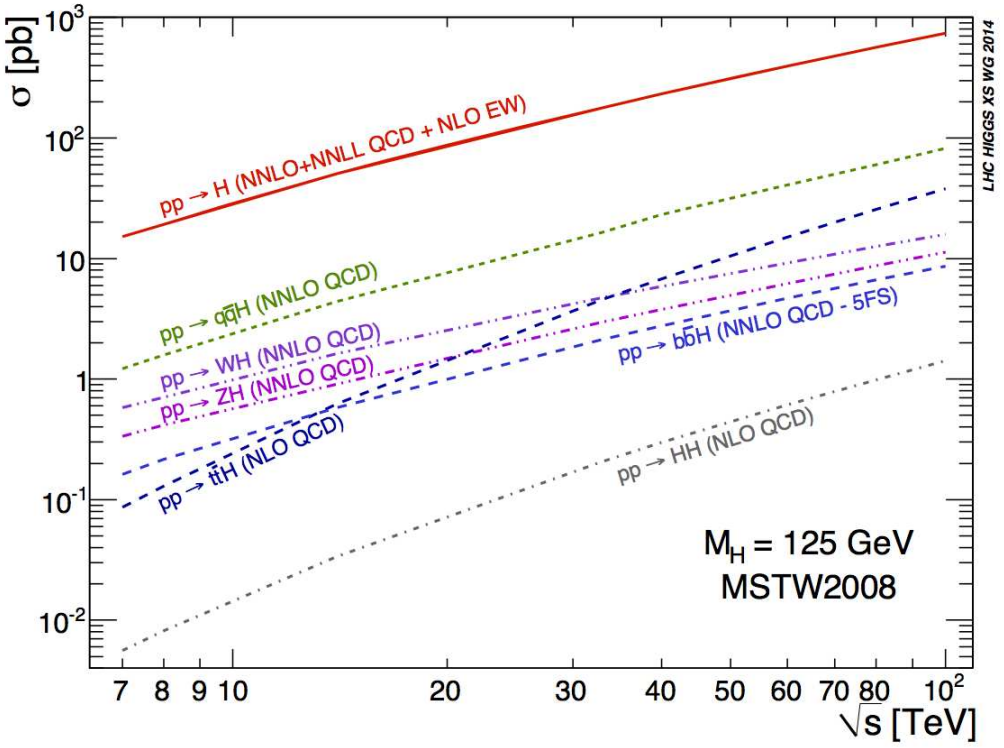

Figure 2.4: Cross section of Higgs production at pp collider. Figure taken from [6]

2.3 Higgs physics at future colliders

The purpose of future colliders are to reach the precision of 1% on the Higgs coupling, in order to verify the SM predictions, to determine the trilinear and quadrilinear Higgs self-coupling and to search for new particles with masses at the TeV scale.

In order to increase the number of events it is necessary to have machine with high luminosity and high center of mass energy.

Others then Muon Collider, that will be described later, some proposed projects are listed below:

- Future Circular Collider (**FCC**): it is the evolution of LHC. It is supposed to be a 100 km tunnel. Three different designs are under studies: FCC-ee ($\sqrt{s}$ from 91 to 365 GeV), a e^+e^- collider, FCC-hh ($\sqrt{s}$ up to 100 TeV), a proton-proton collider, and FCC-he, collisions between a proton beam (50 TeV) and electron beam (60 GeV) [9];
- Circular Electron Positron Collider (**CEPC**): as the name suggest, it is a proposed e^+e^- circular collider, with a tunnel about 100 km long [10];
- International Linear Collider (**ILC**): e^+e^- linear collider working at $\sqrt{s}$ from 250 GeV to 1 TeV [11];
- Compact Linear Collider (**CLIC**): e^+e^- linear collider working at $\sqrt{s}$ from 380 GeV to 3 TeV [12].

Muon Collider and CLIC will have one experiment on their collider, FCC, instead, will have two of them. Further details can be found in [13], while in table 2.1 are reported the machine parameters including the Muon Collider.

As enlightened in the previous section, the future colliders are needed to deeply investigate Higgs sector. As shown in figure 2.4 for p-p machines and in figure 2.5 for lepton colliders, the Higgs production cross section at different center-of-mass energies is sufficiently large to produce a large amount of Higgs Bosons.

The expected precision that the colliders could reach on the measurement of the κ parameters are reported in table 2.2.

Collider	**Type**	$\sqrt{s}$	$\mathcal{L}_{\mathbf{inst}}[10^{34}cm^{-2}s^{-1}]$	$\mathcal{L}[ab^{-1}]$	**Time [years]**
FCC-ee	e^+e^-	91 GeV	100/200	150	4
FCC-ee	e^+e^-	160 GeV	25	10	1/2
FCC-ee	e^+e^-	240 GeV	7	5	3
FCC-ee	e^+e^-	365 GeV	0.8/1.4	1.5	5
FCC-hh	pp	100 TeV	30	30.0	25
FCC-he	e^-p	3.5 TeV	1.5	2.0	25
CEPC	e^+e^-	91 Gev	17/32	16	2
CEPC	e^+e^-	160 Gev	10	2.6	1
CEPC	e^+e^-	240 Gev	3	5.6	7
ILC	e^+e^-	250 Gev	1.35/1.7	2.0	11.5
ILC	e^+e^-	350 Gev	1.6	0.2	1
ILC	e^+e^-	500 Gev	1.8/3.6	4.0	8.5
ILC	e^+e^-	1 Tev	3.6/7.2	8.0	8.5
CLIC	e^+e^-	380 Gev	1.5	1.0	8
CLIC	e^+e^-	1.5 Tev	3.7	1.5	7
CLIC	e^+e^-	3.0 Tev	6.0	5.0	8
Muon Collider	$\mu^+\mu^-$	1.5 TeV	1.25	0.3	2.0
Muon Collider	$\mu^+\mu^-$	3.0 TeV	4.4	1.0	2.0
Muon Collider	$\mu^+\mu^-$	10 TeV	20	12.0	5.0

Table 2.1: Parameters of proposed future colliders taken from [11](ILC), [9](FCC), [14] (CLIC), [10](CEPC) and [15] (Muon Collider)

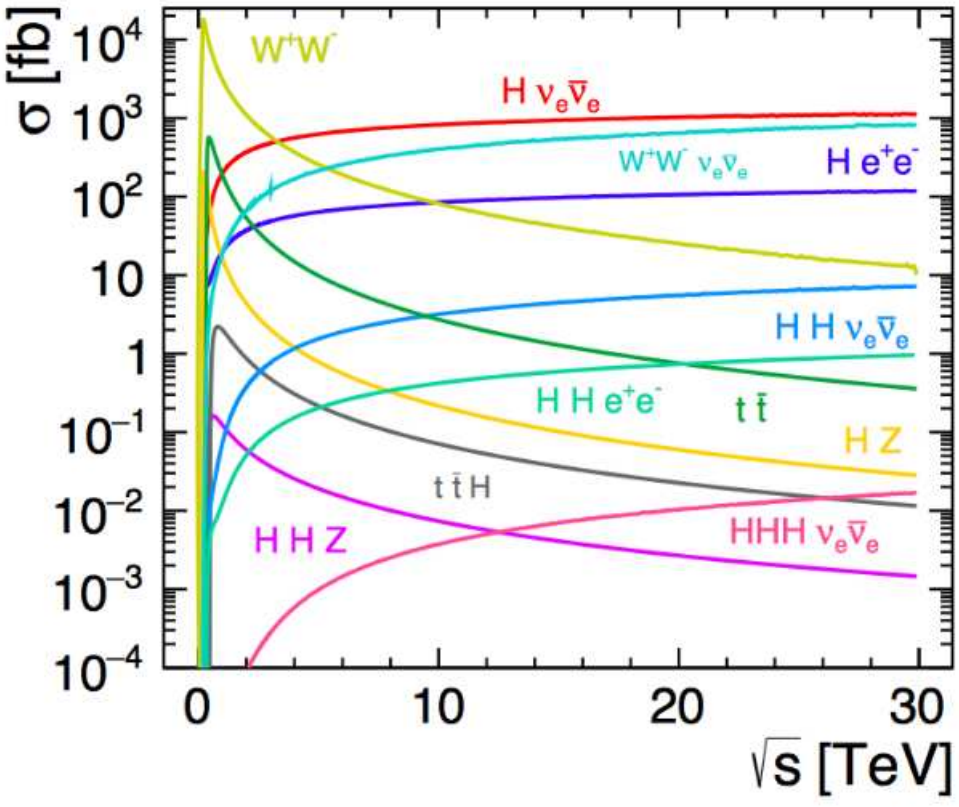

Figure 2.5: Cross section for $l^+l^- \to X$, for this thesis the processes containing the Higgs are the ones of interest. In case of the Muon Collider, the ν_e are ν_μ . Figure taken from [16]

Par.	**HL-LHC**	**MuColl** (10 TeV)	**CLIC** (= 3 TeV)	**CEPC**	**FCC**	**ILC**(= 1 TeV)
κ_W	1.7	0.06	0.11	1.3	0.14	0.24
κ_Z	1.5	0.23	0.23	0.14	0.12	0.22
κ_g	2.3	0.15	0.9	1.5	0.49	0.66
κ_γ	1.9	0.64	2.2	3.7	0.29	1.9
$\kappa_{Z\gamma}$	10.	1	6.9	8.2	0.69	85
κ_c	-	0.89	1.4	2.2	0.95	0.9
κ_t	3.3	6.0	2.7	-	1.0	1.6
κ_b	3.6	0.16	0.37	1.2	0.43	0.48
κ_μ	4.6	2.0	5.8	8.9	0.41	6.2
κ_τ	1.9	0.31	0.88	1.3	0.44	0.57
λ_3	~ 50	6 (2σ)	10	-	5	-
λ_4	-	~ 50	~ 500	-	~ 300	-

Table 2.2: Expected precision expressed in % on κ and λ_3 parameters for future colliders (1σ C.L. if not specified otherwise). In this table only the values expected for the last stage of each collider are reported. For further details see [17], [18] and [19]

In the last rows of table 2.2 are reported also the expected sensitivity on λ_3 and λ_4. For what concern the Higgs self-couplings, the parameters are usually expressed in the SM Effective Field Theory, instead of the κ one, so:

$$\lambda_{3,4} = \kappa_{3,4}(\lambda_{3,4})_{SM} \tag{2.20}$$

The table clearly shows the potential of the Muon Collider with respect to the other future colliders. For most of the parameters it returns the best estimation or it is very close to the best one. For the Higgs self-couplings, instead, it appears as the only machine able to investigate the quadrilinear coupling and the best one for the trilinear one.

2.4 Goal of the thesis

The Muon Collider is the most recent proposal among the future colliders, therefore many studies have not been done yet. The goal of this thesis is to estimate the sensitivity on the cross section $\sigma(H \to WW^*)$ in order to determine the sensitivity on g_{HWW} at Muon Collider. This parameter is particularly important, because, as figure 2.5 shows, the WW-fusion is the main production process of the Higgs in a lepton collider, thus the parameter g_{HWW} appears in almost every calculation concerning the Higgs boson decay.

To find this estimation a simulated sample of the signal $\mu^+\mu^- \to H+X \to W^*W+X \to qq'\mu\nu+X$ will be studied in order to determine the characteristics. Then, it will be compared to the physical background. The considered processes are shown in Chapter 7. The comparison will show which observables are the most suited to separate signal from background.

Then, a Boosted Decision Tree algorithm will be trained using the selected observables and its performance will be studied. This process allows to compute how many events are expected for both signal and background in the Muon Collider, at a given integrated luminosity, and from those the sensitivity on $\sigma(\mu^+\mu^- \to H + X \to W^*W + X \to qq'\mu\nu + X)$ can be calculated.

2.5 Physics at Muon Collider

As discussed above, the Muon Collider could be a powerful tool for the Higgs physics, but this is not the only field that can be explored. Here are reported some examples:

- Direct searches: the collision of elementary particles prevents energy loss due to parton distribution functions, thus Muon Collider allows the direct exploration of physics at 10 TeV. This

means that EW particles pairs that would require a $\sqrt{s} \sim 100\ TeV$ in a pp-collider can be produced. Also, information about WIMP Dark Matter can be achieved, because many candidate have mass in the multu-TeV range [19];

- High-rate measurement: this category includes the Higgs production and its decays, but also the top quark and others;
- High-energy probes: the Muon Collider can study the sensitivity of th EFT for high-energy di-boson and di-fermion production [19];
- Muon physics: several hints of new physics are related to muons and at Muon Collider problems such as the Lepton Flavor Universality, the B meson decay and the magnetic moment g-2 can investigated [20].

Chapter 3

Muon Collider Complex

3.1 Overview

The Higgs physics panorama presented in the previous chapter shows that many aspects are still to be investigated. For example, it is not known if the particle identified as Higgs is the only one existing or if it is just the first of many others. Neither the reason why the electroweak symmetry is broken is fully understood. To answer these questions new facilities are needed, in order to reach high energies and high luminosity to obtain higher precision on the measurements.

Thus, the answer to the question: "Do we need a next generation collider?" is "Of course we do". It is just to decide which facility better suits the purposes.

The most relevant characteristics is that muons are sufficiently heavy elementary particle. With respect to a p-p collider, muons collisions have the great advantage that all the energy of the beams is available for the physic process, because there is no energy share among partons. In addiction they are more clean, the amount of physics background is largely reduced because there are no interaction between other partons [21]. With respect to e^+e^- colliders, the main advantage arise from the mass of the muon which is heavy enough to reduce the energy losses by synchrotron and bremsstrahlung emission, allowing to build a circular facility.

However, also the Muon Collider has its challenges to face [22]. First, it is complex to obtain a high collimated and compact beam, because the muons are produced as secondary decay products with high energy spread. Second, even if the muon are accelerated to relativistic energies and their lifetime increase, they decay along the beam pipe and this produce the so-called "Beam induced background" [23].

In the following section the main characteristics of the collider complex are shown.

3.2 Muon Collider Framework

3.2.1 Luminosity

A key parameter for a collider is the instantaneous luminosity that can be expressed as follow [24]:

$$\mathcal{L}_{inst} = \frac{f n_1 n_2}{4\sigma_x \sigma_y} \tag{3.1}$$

Where the parameters are defined as follow:

- f: frequency of collision;
- $n_i,\ i = 1, 2$: number of particle in each bunch;
- $\sigma_j\ j = x, y$: under the assumption that the spacial distribution of beam particles have a gaussian profile, σ_j is the width in the j-direction. It can be written as:

$$\sigma_j = \sqrt{\beta_j^* \epsilon_j} \tag{3.2}$$

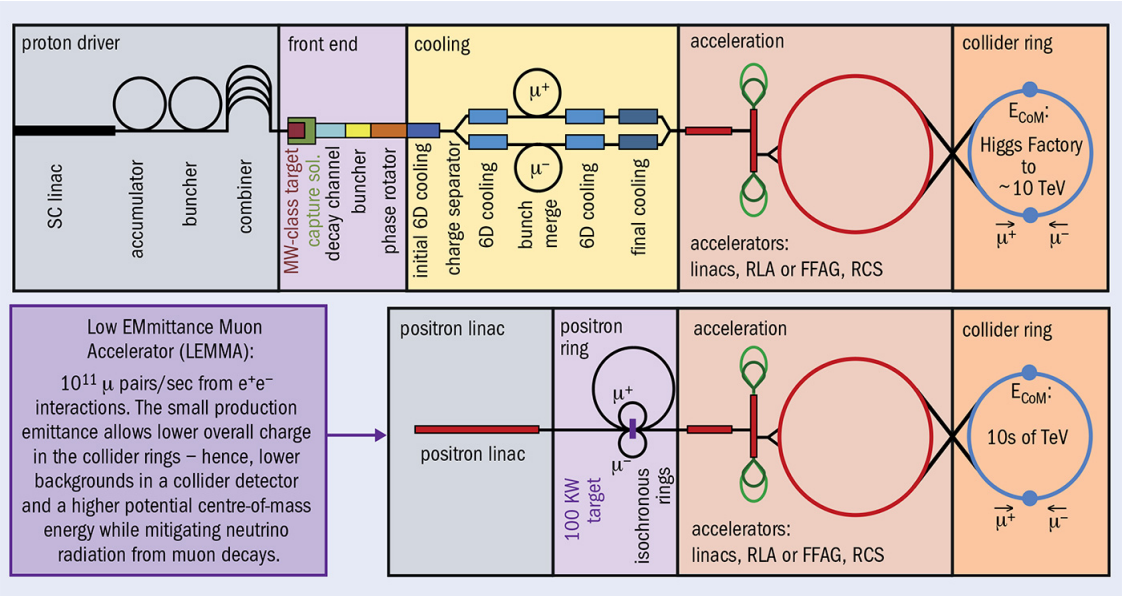

Figure 3.1: Layout of the Muon Collider proposed by MAP (top) and LEMMA (bottom)

where β^* is the amplitude function β evaluated at the interaction point (IP) [25], and ϵ is the emittance along the axis. Each particle along the beam is considered as a point in the six-dimension phase space and the emittance is a measure of the average spread of particles coordinates in both position and momentum phase space [26].

The expected $\mathcal{L}_{inst}$ values for the three stages of the Muon Collider are reported in table 2.1.

In order to obtain high $\mathcal{L}$ the parameters must be properly tuned. In the Muon Collider case the main challenge is to produce beams with low emittance. A solution will be briefly discussed in section 3.2.3.

3.2.2 Muon production

Two methods have been proposed to produce muon beams:

- Proton beam hitting a thick target. Thus, $\pi^{\pm}$ are produced and they decay into muons, $\pi^{\pm} \rightarrow \mu^{\pm} + \overset{(-)}{\nu}$. This method have been extensively investigated by Muon Accelerator Program (MAP) [27];
- Positron beam hitting a target. The muons are produced by the reaction $e^+e^- \rightarrow \mu^+\mu^-$. This method is proposed by Low Emittance Muon Accelerator (LEMMA) collaboration [28].

The latter case, a 45 GeV positron beam hits the target and the annihilation process happens at $\sqrt{s} \sim 0.212\ GeV$, close to the energy threshold for muon pair production. This allows the production of a high collimated and low emittance muon beam. However, the low cross section of the process, $\sigma(e^+e^- \rightarrow \mu^+\mu^-) \sim 1\ \mu b$ for $\sqrt{s} \sim 0.230\ GeV$, implies that to obtain enough muons, the intensity of the proton beam source needs to be very high, inducing a high stress on the target. This scheme, shown in the bottom part of figure 3.1, needs further development. This thesis refers to the MAP configuration that will be now illustrated.

3.2.3 Accelerator scheme

The accelerator scheme developed by MAP is reported in the top part of figure 3.1 [29].

- **Proton Driver:** Through a chain of accelerator developed by Project X [30], an 8 GeV proton beam, characterized by $\sim$ 2 ns bunches, $2 \cdot 10^{14}$ protons at a 15 Hz repetition, is obtained;

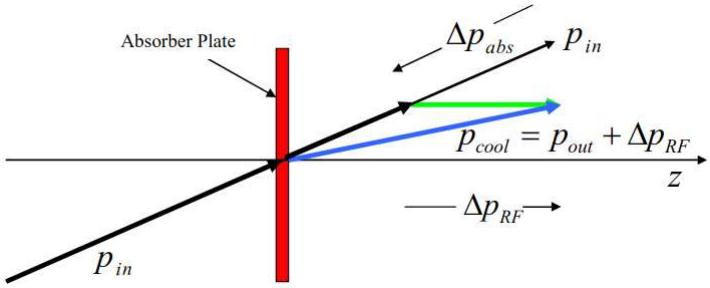

Figure 3.2: Schematic view of ionization cooling. Figure taken from [33]

- **Front end:** Here the beam hits an high-Z target to product the pions ($\sigma \sim mb.$) A transversal confinement is obtained by a magnetic field of ∼20 T at the target, which slows down to 1.5-2 T in the decay channel. Here the pions decay into muons to form a beam with high emittance. At this point, muons have a momentum of 100-200 MeV/c. After the decay channel there is the buncher, made by a system of RF cavities, in where the beam is splitted in a train of bunches. Last, in the phase rotator section, the leading high-energy bunches are decelerated and the late low-energy bunches are accelerated . So far, the normalized r.m.s. emittance of muons captured in a bunch is ∼ 2 cm in all planes [31];

- **Cooling:** In this part of the Muon Collider the emittance is reduced by at least six orders of magnitude by ionization cooling [32]. First, an absorber reduces the initial momentum (p_{in} to $p_{out} = p_{in} - \Delta p_{abs}$) along every direction, while a system of radio-frequency cavities (RS) restores only the component along the beam direction (Δp_{RF}) [33]. A schematic representation of the process is shown in figure 3.2. In this way a cooling along the transversal plane is achieved, but a full reduction of emittance in 6D phase space is needed. The next step consists on a bending magnet which separates particles with different momentum [34]. The particles hit an absorber with a proper geometry such that particles with higher momentum lose more energy. In this way there is a reduction of momentum dispersion along the beam axis, at the prize of a larger position spread in the transversal plane. For this reason, this method is called emittance exchange and a schematic representation is reported in figure 3.3 [35]. In the Front End, an initial 6D cooling is applied, then the muon of opposite charge are separated and then another cooling procedure allows to form the single bunches. Last, another 6D cooling is performed;

- **Acceleration:** In this step, the beam is accelerated by a series of acceleration stages till the desired energies. So far, a final design for this step is not available and three different approaches are under studies: Recirculating Linacs Accelerators (RLA) [36] or Fixed Field Alternating Gradient (FFAG) [37] and Rapid Cycling Synchrotron(RCS) [38];

- **Collider ring:** Last part of the collider facility is the collider ring, in which the beams are injected and collide. In order to minimize the muon losses by decay, it is necessary to minimize the circumference of the ring and so to maximize the magnetic field used to curve the beams. So far, the collider ring has been designed for center of mass energies of $\sqrt{s} = 125\ GeV$ [39], $\sqrt{s} = 1.5\ TeV$ [40], $\sqrt{s} = 3\ TeV$ [41] and $\sqrt{s} = 6\ TeV$ [42].

The parameters of the muon beams at 3 TeV are reported in table 3.1.

3.2.4 Interaction Region

In figure 3.4 is shown a model of the interaction region (IR) [44]. In light blue is enlightened the area outside the detector and the beam pipe, filled with air. In the interaction region the beam pipe is surrounded by tungsten (cyan), iron (brown and black) and concrete (grey and green). A layer of borated polyethylene (purple), BCH_2, envelops the last part of the beam pipe and the tungsten nozzles. These are visible inside the detector, in green. The last portion of the nozzles is made in beryllium.

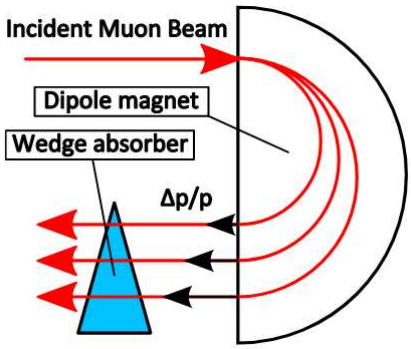

Figure 3.3: Schematic view of emittance exchange. Figure taken from [35]

Parameter	**Unit**	**Value**
$\mathcal{L}$	$10^{34} cm^{-2} s^{-1}$	4.4
f	Hz	12
β^*	cm	0.5
n	10^{12}	2
ϵ	μm	25

Table 3.1: Beam parameter for Muon Collider at $\sqrt{s} = 1.5\ TeV$ [43]

A detailed scheme of the nozzles is reported in figure 3.5. Their role in the BIB mitigation is discussed in section 5.2.

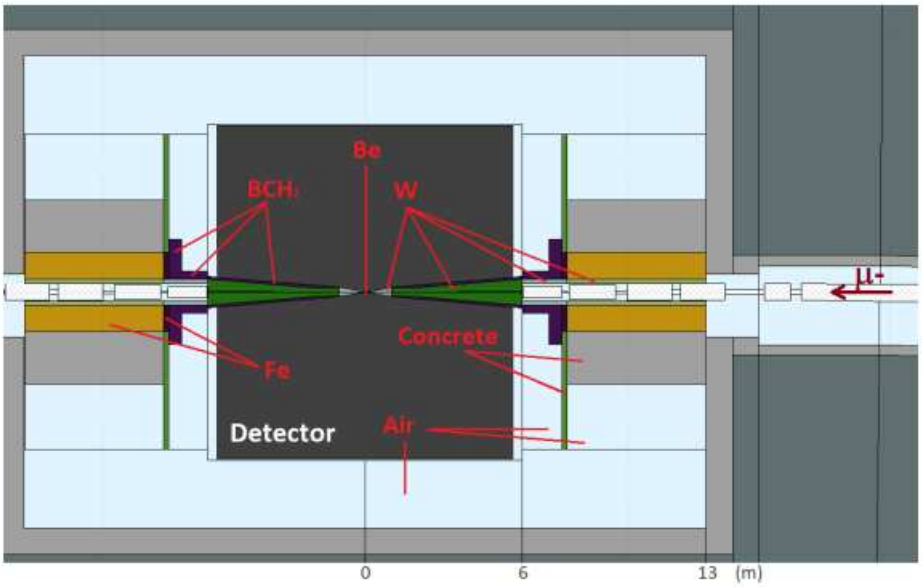

Figure 3.4: Scheme and materials of the Interaction Region. Figure from [44]

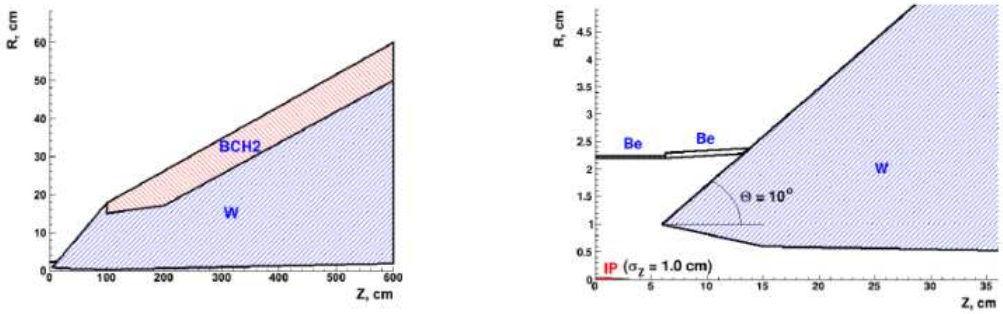

Figure 3.5: Geometry and materials of the nozzles. Figure form [44]

Chapter 4

Detector

4.1 Overview

In order to study the potential of the Muon Collider, a layout of the detector has been designed starting from the one proposed by the CLIC collaboration [45]. However, different colliders require different detectors, so the layout has been modified by MAP [17].

If not specified otherwise, the technical notions in this chapter are taken from [46] and the pictures from [47].

The current design consists in a cylindrical-shaped detector with a diameter of 12.8 m and a length of 11.4 m. It is composed by the following sub-systems:

- Tracking system;
- Electromagnetic calorimeter;
- Hadronic calorimeter;
- Superconducting solenoid;
- Muon detectors.

In figure 4.1 it is possible to see how these are located inside the whole detector. The coordinates quoted in the following sections refers to the frame in which (0,0,0) is the exact center of the detector, the z-axis is oriented along the beam pipe, the y-axis is parallel to the gravity acceleration and the x-axis is perpendicular to the other two.

4.2 Tracking system

The tracking system is composed by three detectors: the vertex detector, the inner tracker and the outer tracker. Together they allow to reconstruct the charged particles tracks and compute their momentum.

Each detector is composed by a set of co-axial barrels and endcaps. Barrels are cylindrical surfaces, whose axis coincides with the beam axis. Endcaps are disc centered as well on the beam axis and they located at both ends of the barrels. Figure 4.2 presents a schematic view of the geometry of the tracking system.

On barrels and endcaps are installed different silicon sensors. The details are given in the following section.

4.2.1 Vertex detector

The vertex detector is composed by four barrels and eight endcaps, four per side. Figure 4.3 helps to understand how the structures are disposed. On both barrels and endcaps are installed double-sensor layers. The cells are pixel of 25 $\mu m \times 25$ μm and 50 μm thick with a time resolution of 30 ps and a spacial resolution of 5×5 μm spatial resolution [50].

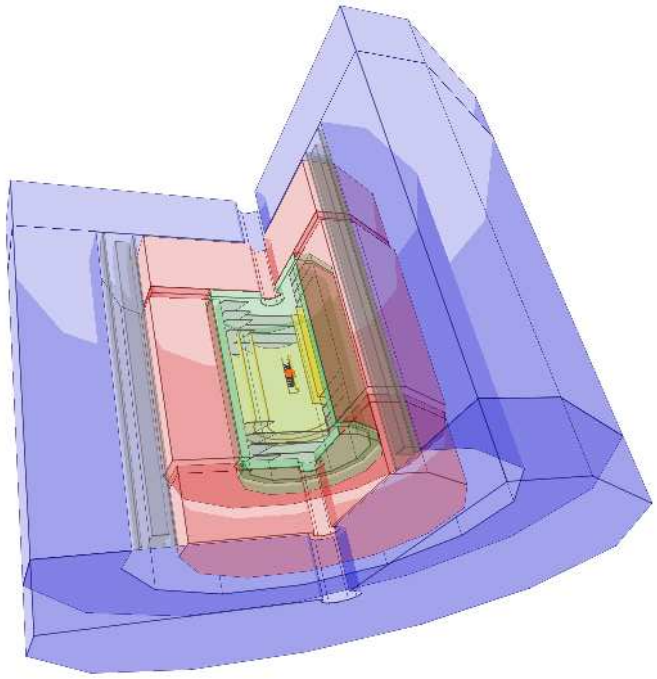

Figure 4.1: Muon collider detector. Figure from [48]

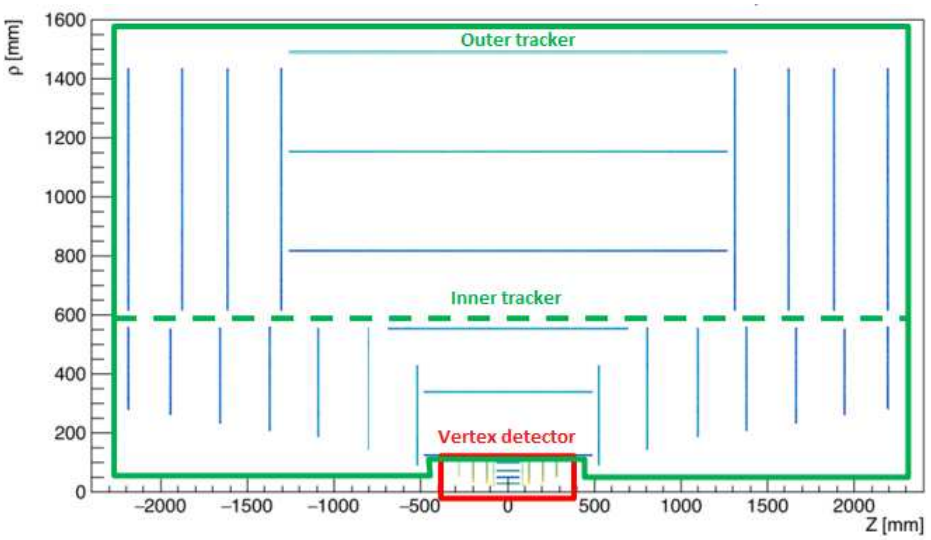

Figure 4.2: Overview of the tracking system. In red is boxed the vertex detector, while in green the trackers. The dotted line divides the inner tracker from the outer one. Figure taken from [49]

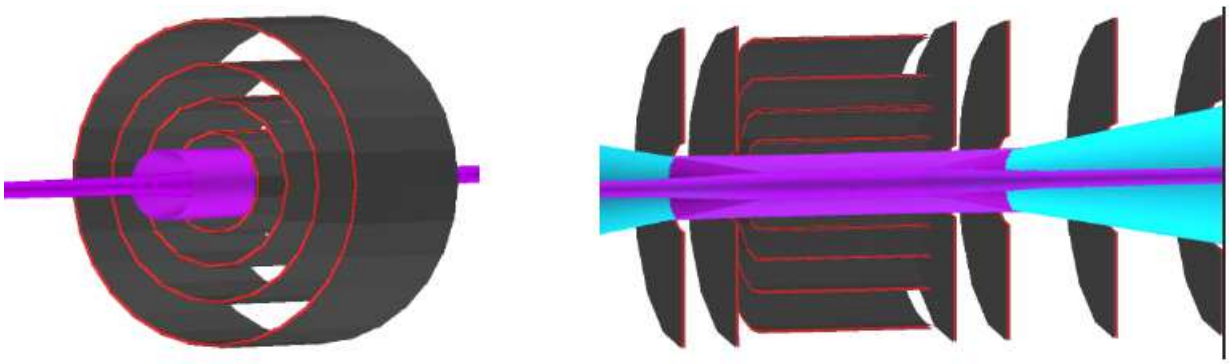

Figure 4.3: Longitudinal view of the barrels (left) and longitudinal section of both barrels and endcaps in the region $z \in [-17\ cm; 28\ cm]$

Barrel	Diameter [cm]
B_1	6.2
B_2	10.2
B_3	14.8
B_4	20.4

Table 4.1: Diameter of the four barrels

The vertex detector is the closest to the interaction point and it has the best resolution in order to identify secondary vertices due to hadrons decay.

In table 4.1 and 4.2 are summarized the geometrical parameters of the detectors.

4.2.2 Trackers

Inner and outer trackers surrounds the vertex detector as it can be seen in figure 4.2.

Their structure is the following [49]:

- Inner tracker: it has three barrels and fourteen endcaps, seven per side. The sensors are strips of 50 $\mu m \times 1\ mm$, 100 μm thick, with time resolution of 60 ps and spacial resolution of 7 $\mu m \times 90\ \mu m$. The geometrical parameter are reported in table 4.3 and 4.4;

- Outer tracker: it has three barrels and eight endcaps, four per side. The sensors are strips of 50 $\mu m \times 10\ mm$, 100 μm thick, with time resolution of 60 ps and spacial resolution of 7 $\mu m \times 90\ \mu m$. The geometrical parameter are reported in table 4.5 and 4.6.

In figure 4.4 and 4.5 are shown the section and the transverse view of the whole system.

The discussion about the tracking performance is presented in section 6.2.1 together with the track reconstruction algorithm.

Endcap	z [cm]	Internal Radius [cm]	External Radius [cm]
E_1	8.0	2.5	11.2
E_2	12.0	3.1	11.2
E_3	20.0	3.8	11.2
E_4	28.0	5.3	11.2

Table 4.2: z coordinate, internal and external radius of endcaps 1 to 4. Endcaps 5 to 8 have the same parameters of endcaps 1 to 4 but the sign of the spacial coordinate [51].

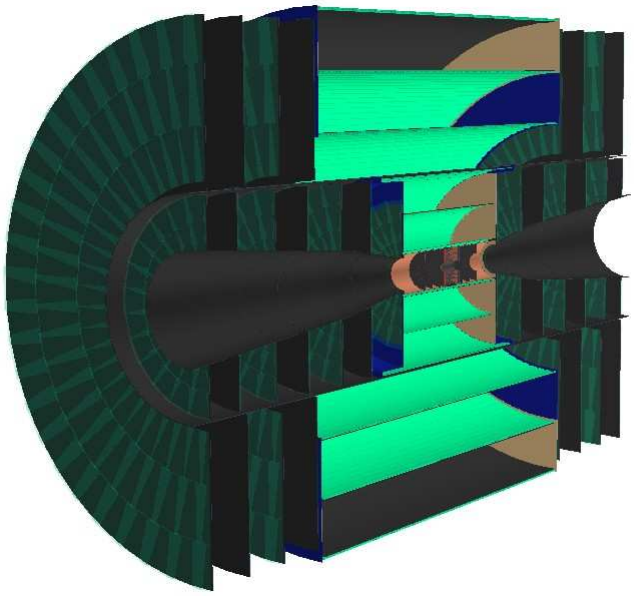

Figure 4.4: Section of the full tracking system

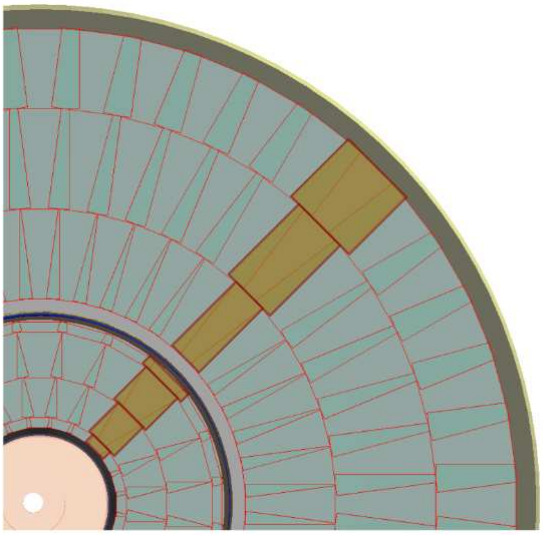

Figure 4.5: Transverse view of last endcap of outer tracker and sixth endcap of inner tracker. Picture from [45]

Barrel	Diameter [cm]
B_1	25.4
B_2	68.0
B_3	110.8

Table 4.3: Diameter of the three barrels of the inner tracker [51].

Endcap	z [cm]	Internal Radius [cm]	External Radius [cm]
E_1	52.4	9.5	42.7
E_2	80.8	14.7	55.8
E_3	109.3	19.0	55.6
E_4	137.7	21.2	56.1
E_5	166.1	23.7	55.7
E_6	194.6	26.4	55.4
E_7	219.0	28.4	55.8

Table 4.4: z coordinate, internal and external radius of endcaps 1 to 7 of the inner tracker. Endcaps 8 to 14 have the same parameters of endcaps 1 to 7 but the sign of the spacial coordinate [51].

Barrel	Diameter [cm]
B_1	163.8
B_2	230.6
B_3	297.2

Table 4.5: Diameter of the three barrels of the outer tracker [51].

Endcap	z [cm]	Internal Radius [cm]	External Radius [cm]
E_1	131.0	61.7	143
E_2	161.7	61.7	143
E_3	188.3	61.7	143
E_4	219.0	61.7	143

Table 4.6: z coordinate, internal and external radius of endcaps 1 to 4 of the outer tracker. Endcaps 5 to 8 have the same parameters of endcaps 1 to 4 but the sign of the spacial coordinate [51].

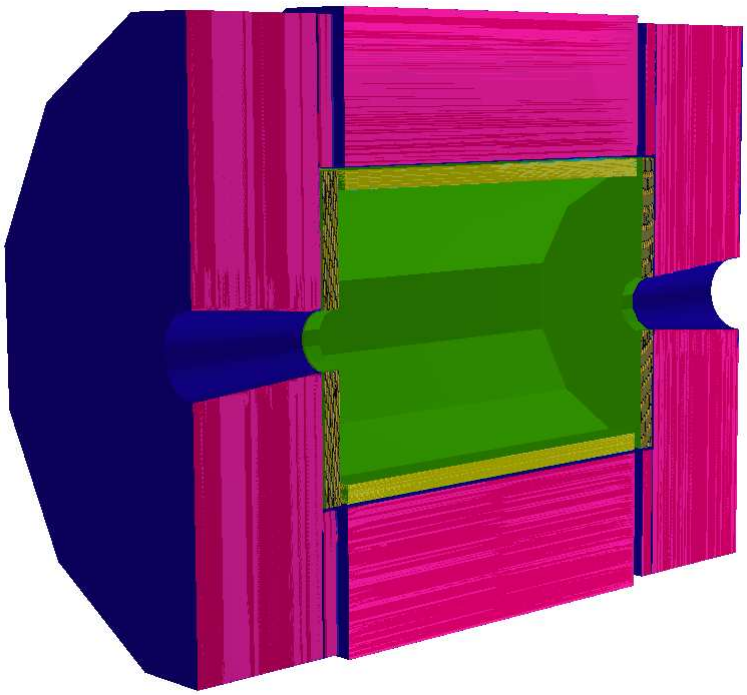

Figure 4.6: Section of the calorimetry system, composed by electromagnetic calorimeter (green) and hadronic calorimeter (purple)

4.3 Calorimeter

The calorimetry system, formed by an hadronic and an electromagnetic calorimeter, allows to measure the energy of the particles. In figure 4.6 a section of the system is visible. Its design is based on the detectors designed for CLIC. The design and the resolution for the Muon Collider are still under study.

The electromagnetic calorimeter (ECAL) structure is formed by a dodecagonal barrel and two endcaps, one per side. On it are installed 40 layers of silicon detectors in cell of $5 \times 5\ mm^2$ separated by a Tungsten absorber 1.99 mm thick. This configuration of silicon layers allows to optimize the spacial resolution, while the choice of Tungsten absorber is justified by the large ratio $interaction\ length/radiation\ length$, so the electromagnetic shower can start earlier in the detector and the fraction of hadronic shower in the ECAL is reduced.

The hadronic calorimeter (HCAL) has a structure very similar to the electromagnetic one. It has a dodecagonal barrel and two endcaps as well. However, in the HCAL there are 60 layers with plastic scintillating tiles characterized by $30 \times 30\ mm^2$ cells. The absorber layers are steel layers 19 mm thick.

As mentioned above, an estimation of the energy resolution for the Muon Collider has not been computed yet. However, studies on jet reconstruction performances have been done and they will be discussed in section 6.5.2

4.4 Solenoid and Muon detector

In figure 4.7 the last parts of the detector are shown. In cyan, right outside the calorimeter system, there is the superconducting solenoid. It produces the magnetic field $B_1 = 3.57\ T$ on the inside region needed to bend the trajectory of charged particles.

An iron return yoke, in red in figure 4.7, envelops the solenoid generating a magnetic field $B_2 = 1.4\ T$ in the opposite direction with respect to B_1. This configuration confines the particles that reach the yoke, except for muons and weak-interacting particles [52].

The dimensions of the system is reported in table 4.7.

On the return yoke is installed the Muon system. It is visible in figure 4.7, in green and blue. It has a structure similar to the calorimeters and the trackers, made by a barrels and endcaps. In

	Internal Radius [cm]	External Radius [cm]
Solenoid	364.9	399.3
Return yoke	446.1	645.0

Table 4.7: Internal and external radius of the superconducting solenoid and the return yoke [51].

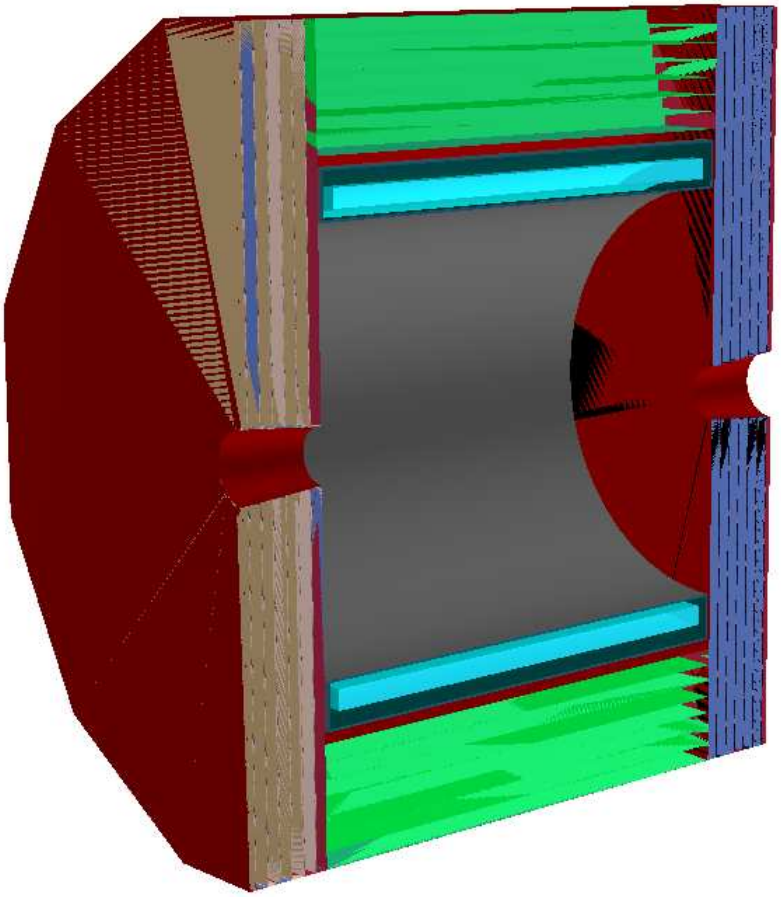

Figure 4.7: Section of solenoid and RCPs

particular, the muon system has seven layers of Resistive Plate Chamber with cells of 30 $mm \times 30$ mm in the barrel and six layers in the endcaps.

As for the other detectors, the performances are discussed in chapter 6.

Chapter 5

Beam Induced Background

5.1 BIB characteristics

One of main challenges of the Muon Collider is dealing with the so-called Beam Induced Background (BIB) mentioned in the previous sections. Muons have a lifetime $\tau = 2.2\ \mu s$ at rest, in the collider they are accelerated to relativistic energies, as consequence the lifetime in the laboratory frame is longer. For example, the decay length is $\lambda_D = 4.7 \times 10^s\ m$ for a 0.75 TeV beam. The amount of BIB it is very high: 1.28 primary decay$\times m^{-1} \times s^{-1}$ for a $\sqrt{s} = 1.5\ TeV$.

From secondary reactions following muon decays, a flux of 0.5-1 kW/m arises in the collider ring and the detector causing two different problems. The first one concerns the hardware, because this high amount of particles at high energies will damage the detector. The second one concerns the reconstruction of the events: particles will leave signals in the apparatus and this will affect the measurement. [23]

A detailed simulation of BIB in the interaction region requires a lot of computational resources. MAP studies found that the all the particles arriving in the detector come from muons decayed in the range of 25 m from the interaction point. The Bethe-Heitler muons behave differently. These arise from pair production after the interaction between photons in the electromagnetic shower and the detector matter. In this case, a range of $\pm 100\ m$ has to be considered.

The final simulation, performed using MARS15, only muons which decayed in the proper range were considered and a sample of Bethe-Heitler muons were added. A part the Bethe-Heitler muons already mentioned, the other particles of the BIB are electrons and positrons coming directly from the decay, which emit themselves photons by synchrotron radiation. When these particles interact with the detector, they produce electromagnetic showers, hadrons and muons.

In figure 5.1 the particle composition of the BIB is plotted as function of the muon decay distance from the interaction point.

The BIB particles momentum distributions are shown in figure 5.2 and in table 5.1 are reported the fractions of particle in the BIB and the average momenta. The dominant fraction of BIB is composed by low-energy photons, electron and positrons and neutrons[54]. The most energetic particles in the BIB are muons, which usually have a momenta of few GeV, but they can reach energies of $\sim 160\ GeV$.

Particle	**Fraction** [%]	$\langle p \rangle$ **[MeV]**
photon	~ 94	1.7
neutron	~ 4	477
electron	~ 1	6.4
Others[1]	< 1	481[2]

Table 5.1: Fraction and average momentum for the different particles which compose the BIB

[1] Others means charged hadrons and muons

[2] The average momentum is referred only to charged hadrons

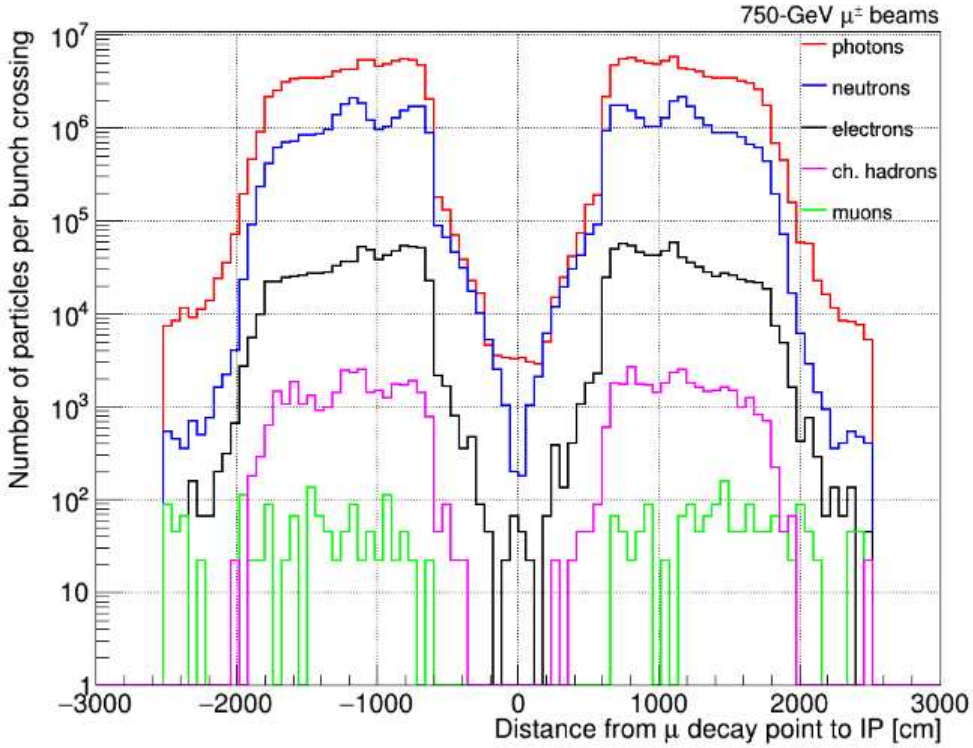

Figure 5.1: Particles per bunch crossing which arrive in the IP as function of decayed muon distance from IP itself. Figure from [53]

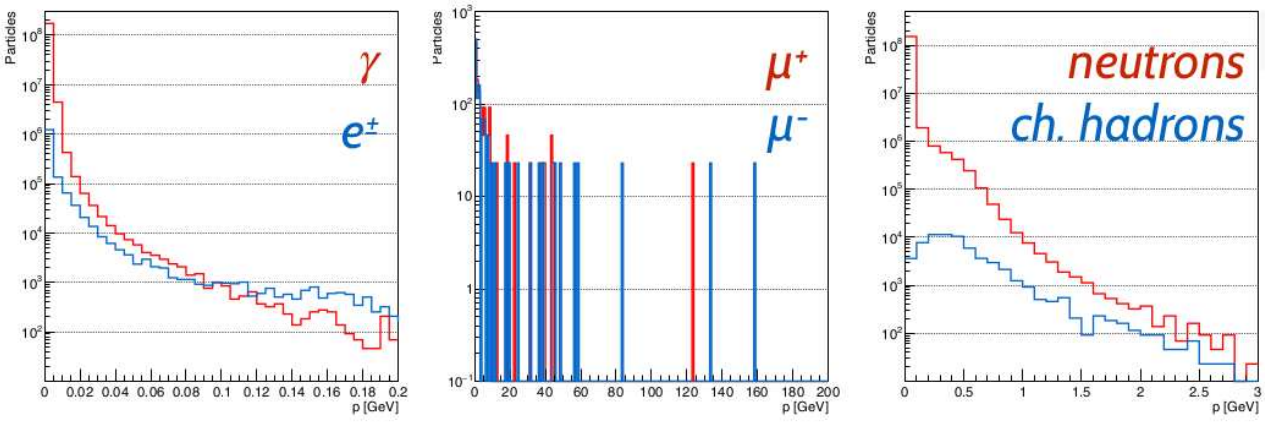

Figure 5.2: Momentum distributions for the different particles of the BIB. Figure from [55]

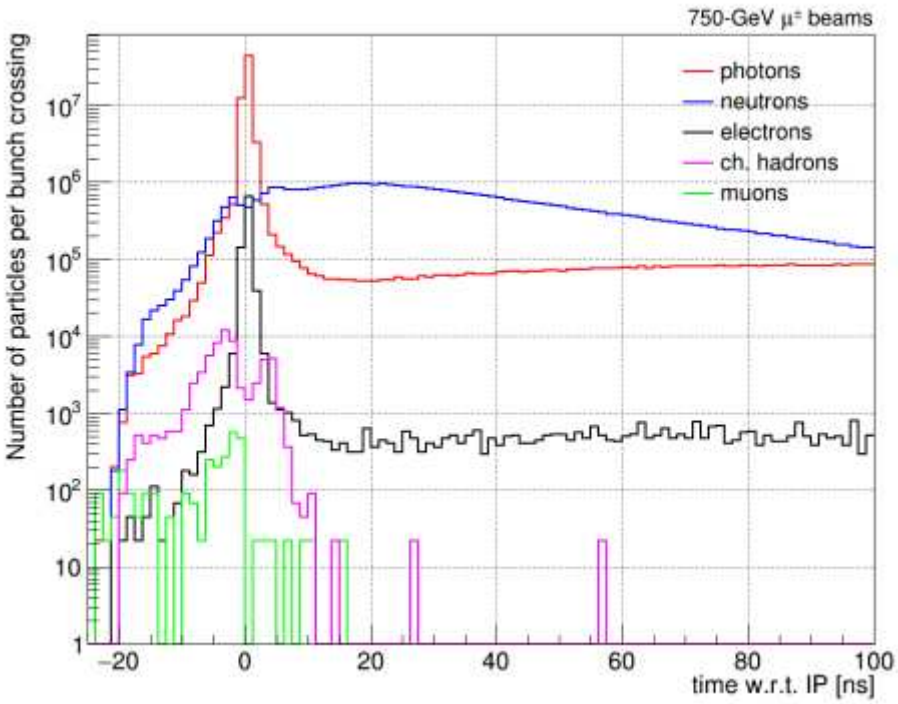

Figure 5.3: Particle per bunch crossing as function of the arrival time minus the bunch crossing time. Figure from [47]

At $\sqrt{s} = 3\ TeV$ the BIB has not been fully studied yet, however, there are hints that its amount is lower with respect to 1.5 TeV, so the results that will be shown are obtained with a conservative approach to the BIB. [23]

5.2 BIB mitigation

Mitigation strategies have been studied since the very begging of the Muon Collider proposal in the 90s [53]. The most updated simulations have shown that the high flux of particle can be reduced by two tungsten absorbers cone shaped nozzles, mentioned above and visible in figure 3.4. These two shields start 6 cm far form the interaction point (IP) and their length is of 6 m. They start with an angle of 10° close to the IP, then, at 1 m, the angle is reduced to 5°. Also at 1 m a capsule in borated polyethylene starts . While the tungsten is effective in minimize the electromagnetic components, this shell is able to reduce the flux of neutrons, which usually come at low-energies [56].

Despite the nozzles, a huge amount of particles reach the detector, therefore further strategies are needed to reduce the impact on the detector. One is to consider the arrival time of the particles with respect to the bunch crossing, shown in figure 5.3. A large spread in the time distribution suggests that a cut around the t_0 could remove a meaningful amount of background [47]. In fact, the bunch crossing is considered at 0 ns, where a peak is visible. The plot refers only to the BIB, so this peak cannot be due to signals. Instead, its origin can be addressed to muon decayed close to the IP and to particles re-emitted by the nozzles after interactions with other BIB particles.

The tracker and the calorimeter requirement are studied in detail. A sample of prompt muons produced at the interaction point at $t = 0\ s$ has been generated and compared to BIB sample. In the left plot of figure 5.4 the arrival time distributions on the first layer of vertex barrel detector of the two samples are compared. On the right, the same plot has been produced for the first layer of the outer tracker barrel. The arrival time is defined as:

$$T_{arrival} = T_{hit} - \frac{|\overrightarrow{r}_{hit}|}{c}$$

with T_{hit} the arrival time of particles at the layer and $\frac{|\overrightarrow{r}_{hit}|}{c} = \sqrt{x^2 + y^2 + z^2}$ the time of flight of a

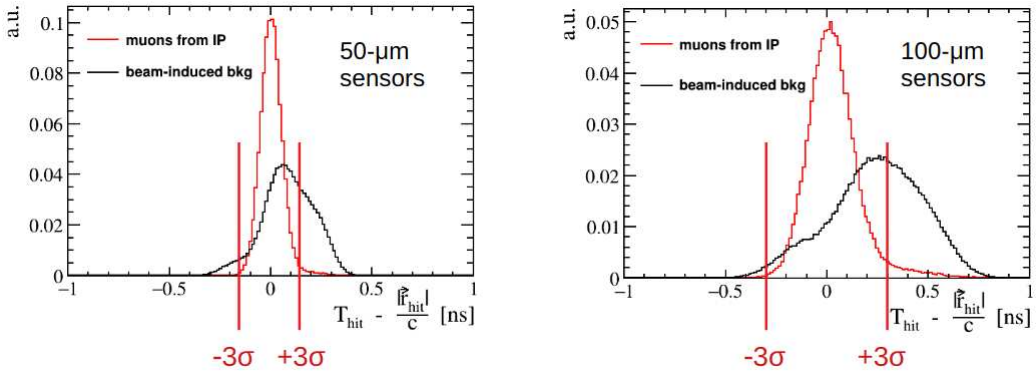

Figure 5.4: Timing of arrival (T_{hit}) - time of flight $|r_{hit}|/c$ distribution in the first layer of vertex barrel detector (left), and in the outer barrel (right). Figure from [47]

photon. In both cases, the signal presents a well-defined gaussian, that be can fitted, therefore the standard deviation of the curve, σ_T, can be extracted. The σ_T depends on the detector considered, however, figure 5.4 suggest that a timing cut at ± 3 σ_T will suppress a large portion of background in each layer. More recent studies suggest that a better window is $[-3\sigma_T,\ 5\sigma_T]$ [52]. Figure 5.5 shows the effects on the tracker system of the proper requirements. There, the average density of BIB particle hits, namely the average number of hits per event per unit of surface, has been plotted for every layer of the tracking system before (blue) and after (yellow) the application of the timing cut. The hit density is reduced significantly. In particular, in the first layer of the vertex detector, where the BIB hits density is higher, the reduction is about 65%.

Similarly, the arrival time in the calorimeter has been plotted in figure 5.6. The distribution for prompt muons is peaked close to zero, while the BIB one presents tails in both directions of the axis, therefore, a proper time window can be applied to reduce the BIB.

Requiring a time window is not the only strategy adopted to mitigate the BIB effects in the calorimeter. Figure 5.7 shows the energy deposited on the calorimeters by the BIB particles. These distribution can be subtracted before the reconstruction of the event.

In figure 5.8 the energy released by BIB particles in the ECAL has been compared to the one released by the signal $\mu^+\mu^- \to \nu\overline{\nu} \to b\overline{b}$, $\sqrt{s} = 1.5\ TeV$. The plot shows that BIB particles (the red distribution) release energy in the first layers of the calorimeter, while the peak of the signal (blue) is shifted of about 5 cm with respect to the BIB one. Therefore, inserting a pre-shower absorber before the ECAL could reduce the BIB energy released in the detector.

For the purpose of this thesis is important to discuss also the effect of the BIB on the muon system. Figure 5.9 shows the spacial distribution of BIB particles in the muon system. A sizeable contribution is present only in the very forward region, namely $\theta < 10°$ and, symmetrically, $\theta > 170°$.

However, the BIB contribution in the very forward region can be suppressed by requiring the presence of a cluster, which is a group of hits built with the algorithm PandoraPFA (more details in the next chapter), $\theta > 10°$ and the transversal momentum greater than 5 GeV. The results are reported in figure 5.10.

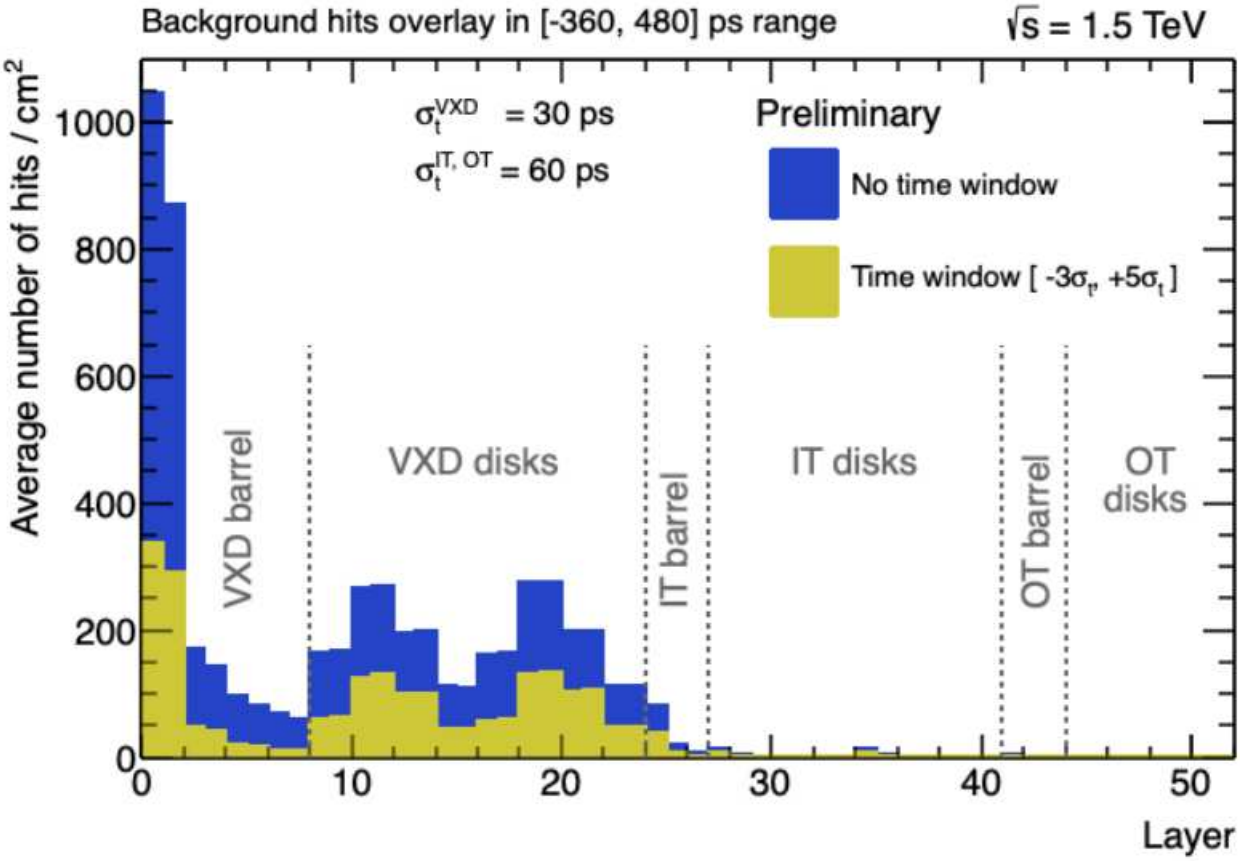

Figure 5.5: Effects of timing cuts on occupancy in tracker layers. Figure from [52]

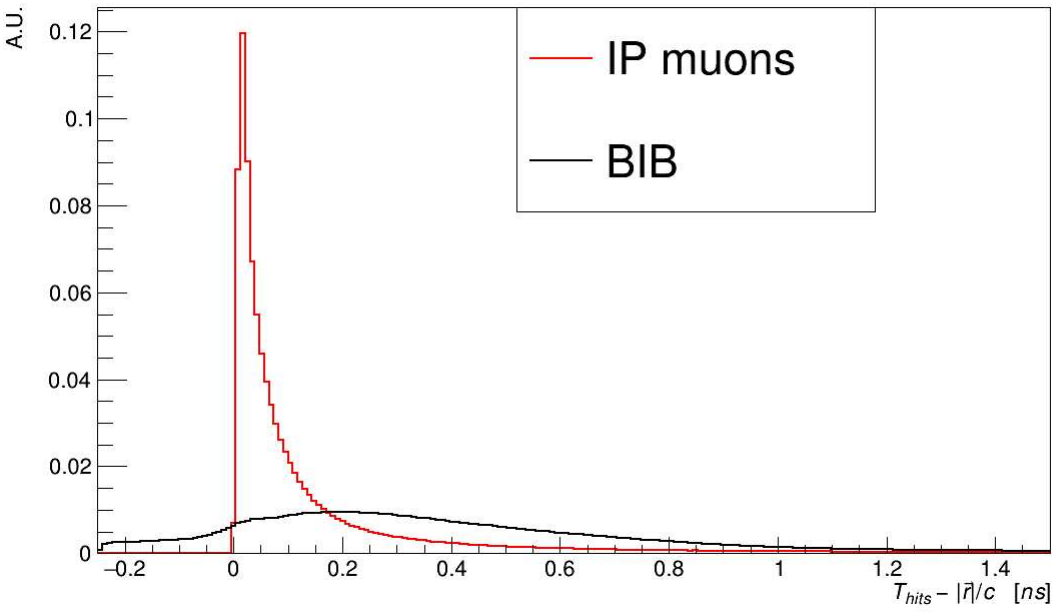

Figure 5.6: Timing of arrival (T_{hit}) - time of flight $|r_{hit}|/c$ distribution in the calorimeter. Figure from [47]

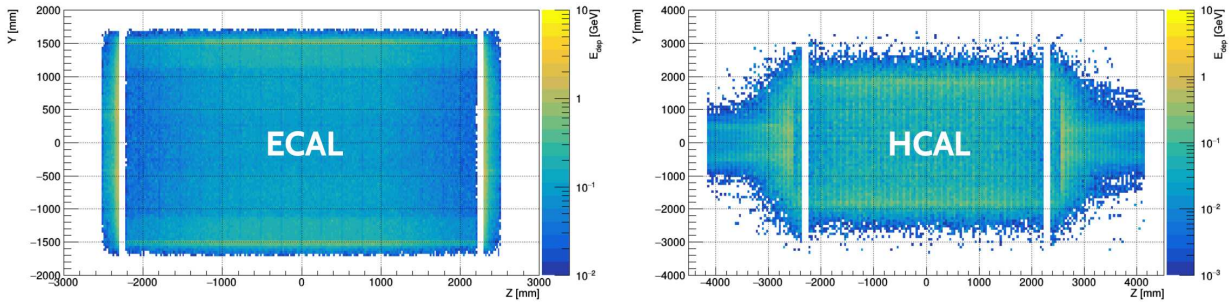

Figure 5.7: Energy deposited by the BIB in the electromagnetic calorimeter (left) and in the hadronic calorimeter (right). Figure from [57]

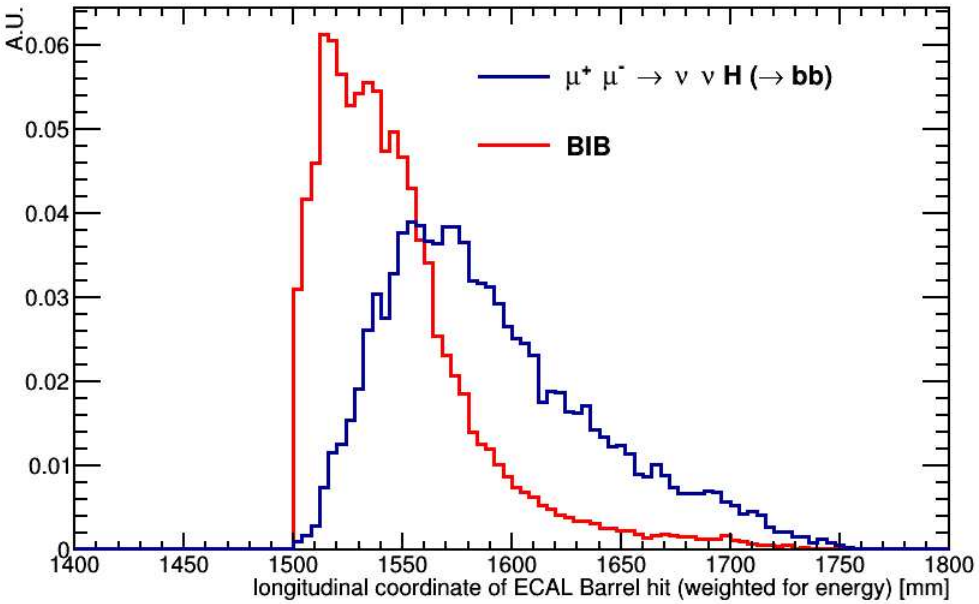

Figure 5.8: Energy released distribution of BIB (red) and $\mu^+\mu^- \rightarrow \nu\overline{\nu} \rightarrow b\bar{b}$, $\sqrt{s} = 1.5\ TeV$ signal in the ECAL. Figure from [47]

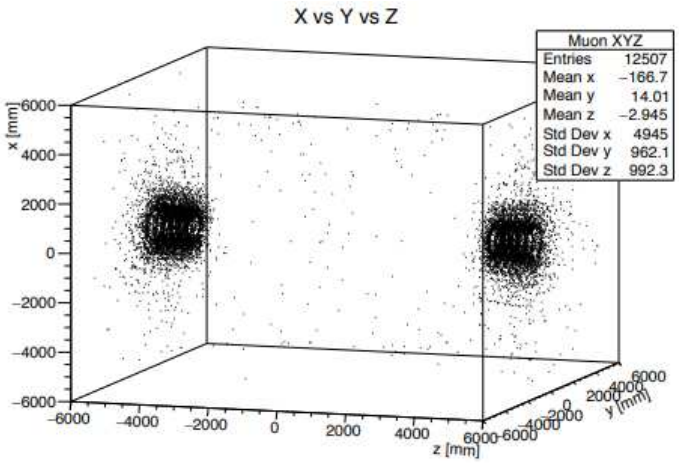

Figure 5.9: 3-dimensional distribution of BIB particles in the muon system. Figure from [58]

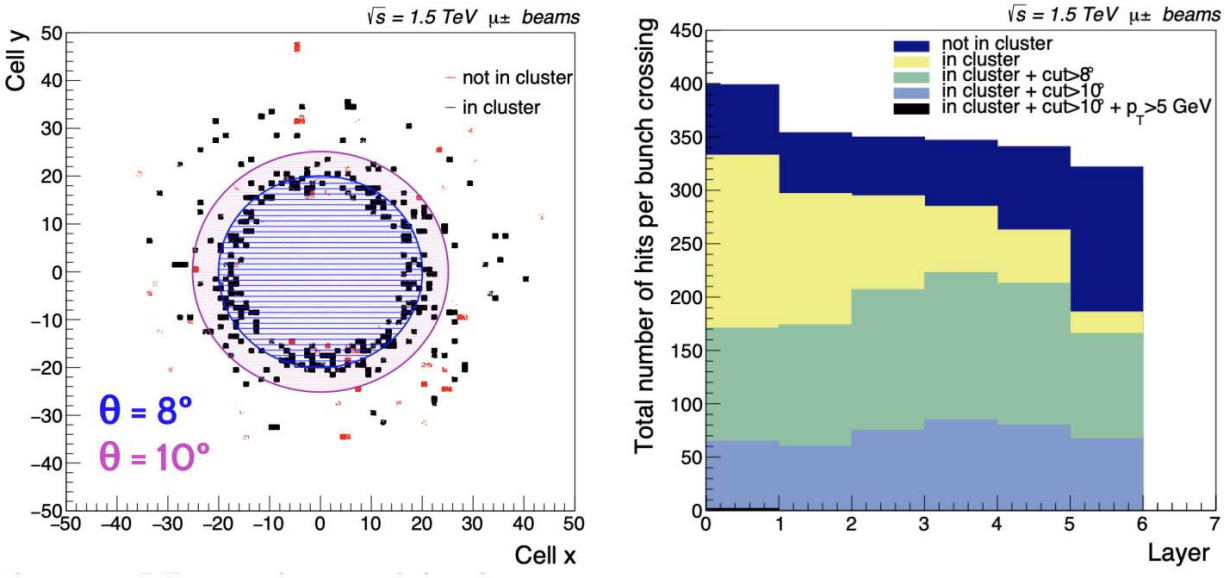

Figure 5.10: BIB hits distribution in the endcap region of muon system on the left. On the right BIB hits per bunch crossing per endcap layer after the application of several cuts configuration. Figure from [54].

Chapter 6

Simulation tools

In this chapter a overview of the tools used for the whole simulation process is presented. First, the generation and simulation of the events will be discussed, then there will be a focus on the reconstruction part.

6.1 Event generation and simulation

The generation process is developed in three steps:

- **Generation of the main process**: using a dedicated software, the event is produced. For this thesis two different programs were used. The one adopted in the first analysis was PYTHIA [59] which generates event at the Leading Order (LO). In a second moment, for a correct study of the signals and backgrounds, it has been used WHIZARD [60], which, instead, generates events at higher orders;

- **Passage through the detector**: using GEANT4 [61], the particles, generated at the origin of the system, are propagated through the detector, whose geometry is simulated with DD4HEP [62]. During this step there is the so-called BIB overlay. The BIB, in fact, is not present in the file produced by PYTHIA or WHIZARD. To reproduce the BIB behaviour, the BIB particles are generated in a specific point in the detector, not in the origin. GEANT4 propagates also the BIB particles. This last process is extremely slow, therefore a pool of reusable events has been produced [63]. The output of GEANT4 contains the signals recorded by the sensors, the so-called simulated hits, which includes physics hits plus BIB;

- **Hits digitization**: to simulate the effects of detectors, the simulated hits are digitized. A digitization of the tracking detector is not available yet, so the hits are treated differently from the calorimeter and muon system ones. To reproduce the detector effects, the hits coordinates x and y in the tracking are smeared with a gaussian distribution peaked in the simulated position with a σ equal to the single point resolution of the sensor. The same process is applied to the timing response, with the gaussian distribution with σ equal to the time resolution of the sensor [63].

  The digitization of the calorimeters and muon system hits, instead, works by summing for each cell all the hits arrived in the cell in the readout time window[63].

6.2 Track reconstruction

The track reconstruction is performed in two step:

- Track finding: using the conformal tracking algorithm, the hits belonging to the same particle are identified and the track candidates are built;

- Track fitting: using the Kalmar filter the parameters of the particles trajectory are estimated.

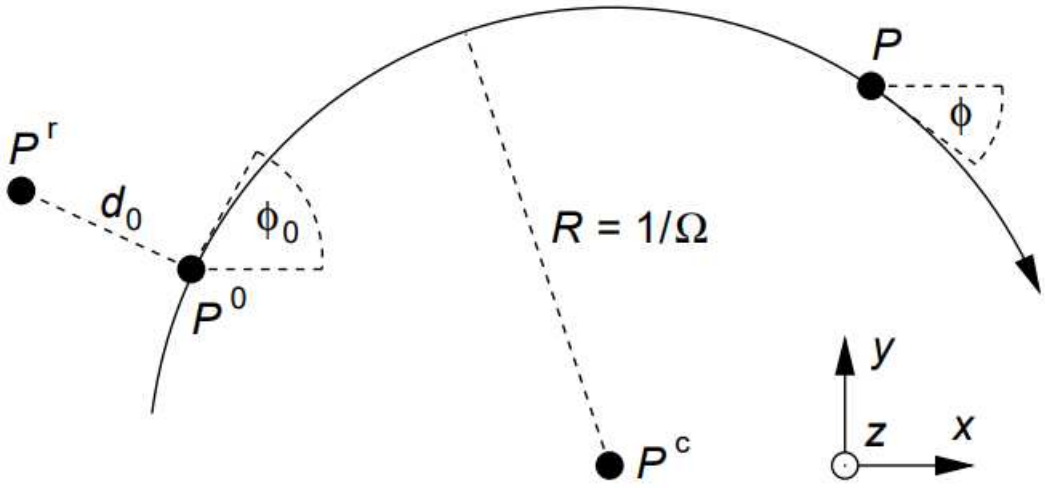

Figure 6.1: Projection of a trajectory segment in the x-y plane. The projection is an arc centered in P^c. Figure from [64]

6.2.1 Tracks parametrization

Before entering in the details of the track reconstruction processes, it is important to define tracks parametrization.

With a magnetic field parallel to the z-axis, as in the case of Muon Collider, the trajectory of a charged particle, under the assumption of negligible energy losses and multiple scattering, is an helix. The projection on the x-y plane is an arc of circumference, while the z displacement can be expressed as a linear function of the arc length, s, in the x-y plane.

The parametrization is defined by an arbitrary reference point $P^r = (P^r_x, P^r_y, P^r_z)$,in this case the origin of reference frame has been chosen, and five track-parameters: Ω, ϕ_0, D_0 Z_0 and $\tan\lambda$. These parameters refer to a specific point P^0 in the helix, in this case chosen as the closest point to P^r in the x-y plane. Figure 6.1 shows the projection of a trajectory segment in the x-y plane. The arc is described by three of the five parameters:

- Ω: it is the curvature parameter of the track and it is related to the curvature radius R, in particular $|\Omega| = 1/R$. $\Omega \in]-\infty, \infty[$ and its sign is defined by the particle momentum. $\Omega > 0$ implies that the trajectory is traveled clockwise and, because of the magnetic field is parallel to the z-axis and oriented in the positive direction, the particle has positive electric charge. For the same considerations $\Omega < 0$ means a negative charged particle;
- ϕ_0: it is the azimuthal angle of the particle at P^0;
- D_0: it is the impact parameter, defined as the signed distance in the x-y plane between P^r and P^0, where the sign is positive if the particle travels left to right, looking from P^r to P^0. With this definition the sign of D_0 and Ω are correlated, in particular they have the same sign if P^r is inside the arc, otherwise opposite sign. The impact parameter is computed as follow

$$D_0 = -(P^r_x - P^0_x)sin\phi_0 + (P^r_y - P^0_y)cos\phi_0 \tag{6.1}$$

Figure 6.2 shows the trajectory in the s-z plane, which is a straight line parametrized by the last parameters of the track:

- Z_0: it is the longitudinal impact parameter, i.e. the z position of the track at P^0 with respect to the reference point P^r, namely:

$$Z_0 = P^0_z - P^r_z \tag{6.2}$$

- $tan\lambda$: it is the slope of the trajectory in the s-z plane and it is related to the momentum of the particle and the polar angle θ:

$$tan\lambda = \frac{p_z}{\sqrt{p^2_x + p^2_y}} = cot\theta \tag{6.3}$$

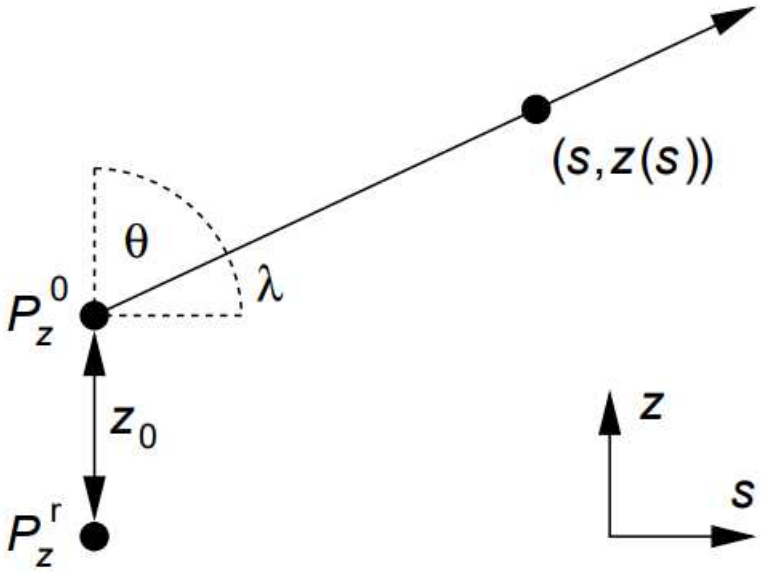

Figure 6.2: Projection of a trajectory segment in the x-y plane. The projection is a straight line. $s(P)$ is defined as the arc length in the x-y plane between P and P^0. Figure from [64]

From the parameters of the tracks the charge Q and the momentum of the particles can be computed:

$$Q = sgn\left(\frac{B}{\Omega}\right) \tag{6.4}$$

$$p_T = \frac{cBQ}{\Omega} \tag{6.5}$$

$$p = p_T\sqrt{1 + (tan\lambda)^2} \tag{6.6}$$

where $p_T = \sqrt{p_x^2 + p_y^2}$ is the transversal momentum, B is the z component of magnetic field, which coincides with the total magnetic field in the Muon Collider detector, c is the speed of light and p is the module of the momentum $\overrightarrow{p}$. The components of $\overrightarrow{p}$ are computed as follow:

$$p_x = p_T cos\phi_0 \tag{6.7}$$

$$p_y = p_T sin\phi_0 \tag{6.8}$$

$$p_z = p_T tan\lambda \tag{6.9}$$

6.2.2 Track finding

As mentioned above, the track finding step is needed to identify hits belonging to the same track and to build the track candidates that will be fitted in the last step of the track reconstruction process. For these purposes, the conformal tracking is adopted [65]. This is a pattern recognition algorithm that combines two different methods, namely the conformal mapping and the cellular automaton-based track finding.

The first method consists in mapping each hit in the conformal space: $(x,\ y) \rightarrow\ (u,\ v)$ using the following transformation [66]:

$$u = \frac{x}{x}^2 + y^2 \tag{6.10}$$

$$v = \frac{y}{x}^2 + y^2 \tag{6.11}$$

The reason behind this transformation is that charged particles trajectories that are circles passing through the origin in the $(x,\ y)$ space became straight lines in the conformal space coordinates $(u,\ v)$.

It is important to underline the fact that not every trajectory is mapped in a straight line in the conformal space for two possible reasons. The first one is that the particle may not be generated in the origin of the (x, y) space. These particles are defined as "displaced". The second reason is that particle generated in the origin may undergo multiple scattering, therefore the trajectory in the (x, y) space deviates from a circle.

In order to consider these deviations, the pattern recognition is performed with a cellular automaton algorithm (CA)[67] which builds the so-called "cellular track" candidates in two steps:

- **Building**: the algorithm takes a subset of hits (e.g. the hits in the vertex detector), called "seeding collection". Each hit in the seeding collection is called "seed". For each seed, one or more "seed cells" are created by connecting the seed with its closest "neighbor hits". The neighbor hits are hits which respect the following conditions: they must lay on a different detector with respect to the seed, and have a polar angle $\Theta = arctan(u/v) + \pi$ belonging to $[\Theta_{seed} - \Delta\Theta,\ \Theta_{seed} + \Delta\Theta]$, with $\Delta\Theta$ a fixed parameter. If a seed sell length is greater than a fixed parameter l_{max}, the cell is discarded.

  All the seed cells created from a seed are extrapolated for a fixed distance in the cell direction and a new search for neighbor hits is performed. At this point a new extrapolation is performed.

  To each cell is given a "weight" equal to the number of cells further connected to the cells, therefore the higher the weight the higher the potential of the cell to make a track.

  The cellular track candidates are created as chains of cells which lay in a certain angular window. Candidates which do not have a minimum number of hits are discarded. For each candidate a linear regression fit is preformed in both (x, y) and (s, z) planes. If both reduced χ^2 obtained are below a fixed parameter, χ^2_{max}, the candidates are kept, otherwise they are discarded. For further details see [67].

- **Extension**: the extension of cellular track candidates is performed in two different ways. If the transversal momentum computed from the parameters fitted in the previous step is greater than a fixed threshold p_T^{th}, the candidate is extend using as seed the endpoint of the track and searching the nearest neighbor hits in the the adjacent detector layer. More than one extension can be created in this way, but only the one with the minimum reduced χ^2 is selected. The procedure is iterated till the final layer of the tacking system is reached.

  The tracks with transversal momentum below the threshold are extend after the others, using all the remaining hits. No neighbors search is performed and all the hits which lay in the same side of the detector considering the z-coordinate with respect to the seed. For further details see [52] and [67].

6.2.3 Track fitting

The estimation of the trajectory parameters is not straightforward, in fact, due to possible energy losses or multiple scattering, the trajectory can deviate from the expected helix.

To properly deal with these phenomena the fitting procedure is performed with the Kalman filter algorithm[68]. First, a χ^2 fit is performed to the first, the middle and the last hit of a cellular candidate.

Using the output parameters and their uncertainties from the χ^2 fit as input, the Kalman filter is applied. The algorithm works progressively from one hit to the other, updating the parameters of the track at each iteration. It works in two steps:

- **Prediction step**: calling q_k the vector of the parameters at the detector layer of the hit k, the algorithm compute:

  $$q_{k+1,\ predicted} = f_{k+1,\ k}(q_k)$$

  where $f_{k+1,\ k}$ is the propagator function from the layer k to the layer $k+1$. In the same step, the uncertainties on the parameters (covariance matrix) are propagated using the Jacobian matrix of the propagator;

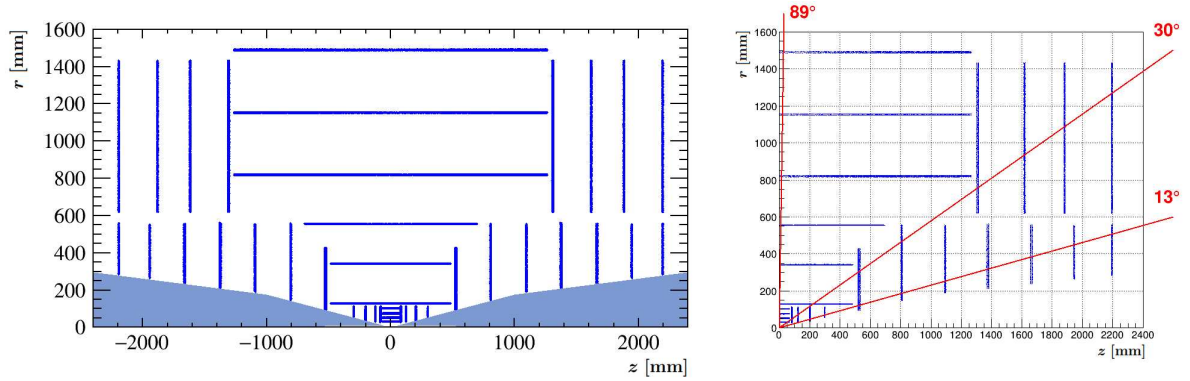

Figure 6.3: On the left the structure of the tracking system in the region $z \in [-240,\ 240]$ cm and $r = \sqrt{x^2 + y^2} \in [0, 160]$ cm. In cyan is indicated the region occupied by the nozzles. On the right, the structure of the tracking system is reported considering $z \in [0,\ 240]$ cm. The red lines form a the polar angle $\theta = 13,\ 30,\ 89°$. Figure from [52].

- **Update step**: the vector of the parameters is updated using a weighted average in the following way:

$$q_{k+1} = q_{k+1,\ predicted} + K_{k+1}[m_k - h_{k+1}(q_{k+1,predicted})]$$

where h_{k+1} is a function that relates the measured parameters m_k to the estimated parameters q_{k+1} (see [68] for further details). K_{k+1} is the gain matrix built with the covariance matrix of the parameters.

6.3 Tracks reconstruction performance with no BIB overlaid

In this section the performance of the track reconstruction algorithm is discussed. Efficiency and resolution of the transversal momentum will be defined and plotted as function of the polar angle θ and the transversal momentum of the particles.

For this study six Monte Carlo samples of 100000 prompt muons were generated with the following characteristics [52]:

- three samples with fixed muon momentum, respectively at 1, 10 and 100 GeV, and θ uniformly distributed in the range [10°, 170°], that is the acceptance region in the current detector configuration;
- three samples with fixed polar angle, respectively at 13°, 30° and 89°, and p_T uniformly distributed in the range [0.1, 100] GeV.

Figure 6.3 reports the layout of the tracking detector (left) and highlights the three different polar angle at which prompt muons were generated [52].

Tracking efficiency

The tracking reconstruction efficiency ϵ_{trk} is defined as:

$$\epsilon_{trk} = \frac{N_{reco}}{N_{tot}} \tag{6.12}$$

where N_{reco} is the number of reconstructed tracks, while N_{tot} is the number of reconstructable MC particles, i.e. particles with a polar angle within the acceptance region and a transversal momentum greater than 0.1 GeV.

In figure 6.4 the efficiency is plotted as function of θ for the three samples with fixed momentum. Due to the symmetry of the detector the events in the range $\theta \in [90,\ 170]°$ were folded into the range $\theta \in [10,\ 90]°$.

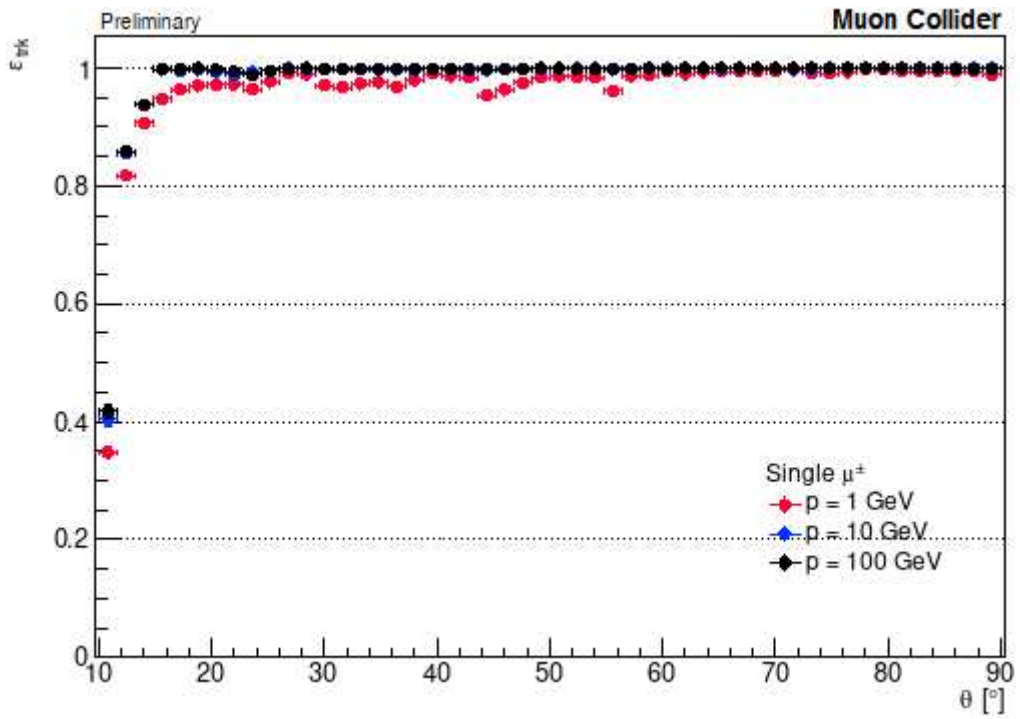

Figure 6.4: Tracking efficiency as function of the polar angle, for prompt muons with momentum fixed at 1, 10, 100 GeV. Figure from [52]

The three samples behave similarly. At low angles the efficiency is $\sim$ 42 % for $p = 10,\ 100\ GeV$ samples and $\sim$ 35% for the last one. This is due to the presence of the shielding nozzles which cover a region of $\theta = 10°$. Efficiency increases rapidly and reaches the plateau at $\theta \simeq 18°$. For the $p = 1\ GeV$ sample the efficiency is $\sim$ 98% while for the other two is close to 1. The $p = 1\ GeV$ sample suffers also of efficiency decreases in the transition zones between barrels and endcaps. Due to the low momentum, the muons of this sample are more subject to deviations, therefore they are more sensitive to the detector structure. This is the reason why the other samples do not present the same behaviour.

In figure 6.5 the efficiency is plotted as function of the muon transversal momentum for the three samples with θ fixed. The samples with $\theta = 30°$ and $89°$ the efficiency has a minimum at very low momenta, while for $p_T \geq 1\ GeV$ it reaches the plateau of $\sim$ 1. Instead, for $\theta = 13°$ the efficiency remains around 87%, lower than the other samples, as one can expect from figure 6.4.

Transversal momentum resolution

The transversal momentum resolution is defined as:

$$\frac{\Delta p_T}{p_T^2} = \frac{p_{T,reco} - p_{T,true}}{p_{T,true}^2} \tag{6.13}$$

with $p_{T,true}$ is the Monte Carlo truth, i.e. the transversal momentum of the Monte Carlo particles, $p_{T,reco}$ is the transversal momentum of the reconstructed track.

In figure 6.6 the resolution is plotted as function of the polar angle for the three samples at fixed momentum.

In each sample the resolution follows the same trend, reaching the best values in the region $\theta \in [50, 90]°$, while it gets worse in the forward region. The plot shows that the resolution improves for muons with higher momentum, in fact, the best results are obtained with the $p = 100\ GeV$ sample in the right portion of the plot, where the resolution is $\sim 0.004\%$. Instead, the worst value is $\sim 5\%$, obtained for the $p = 1\ GeV$ sample in the forward region. In figure 6.7 the same behaviour is highlighted. In this plot the resolution for the samples at fixed θ has been plotted as function of the p_T. The maximum value of $\sim 0.004\%$ is now obtained for muons with a transversal momentum greater

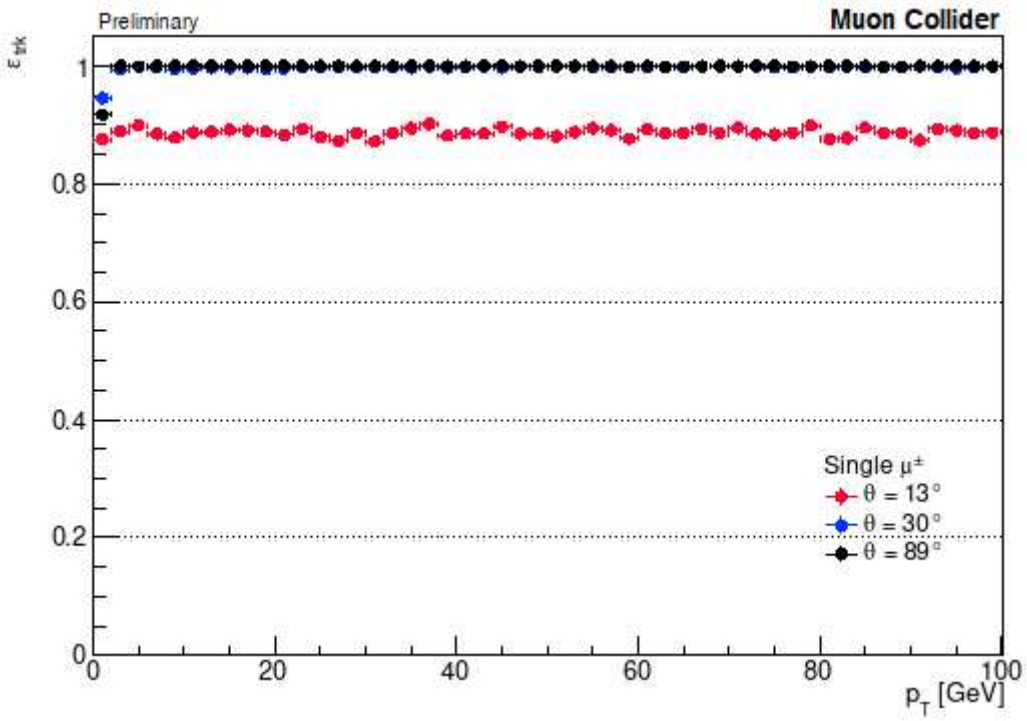

Figure 6.5: Tracking efficiency as function of the transversal momentum, for prompt muons with θ fixed at 13°, 30°, 89°. Figure from [52]

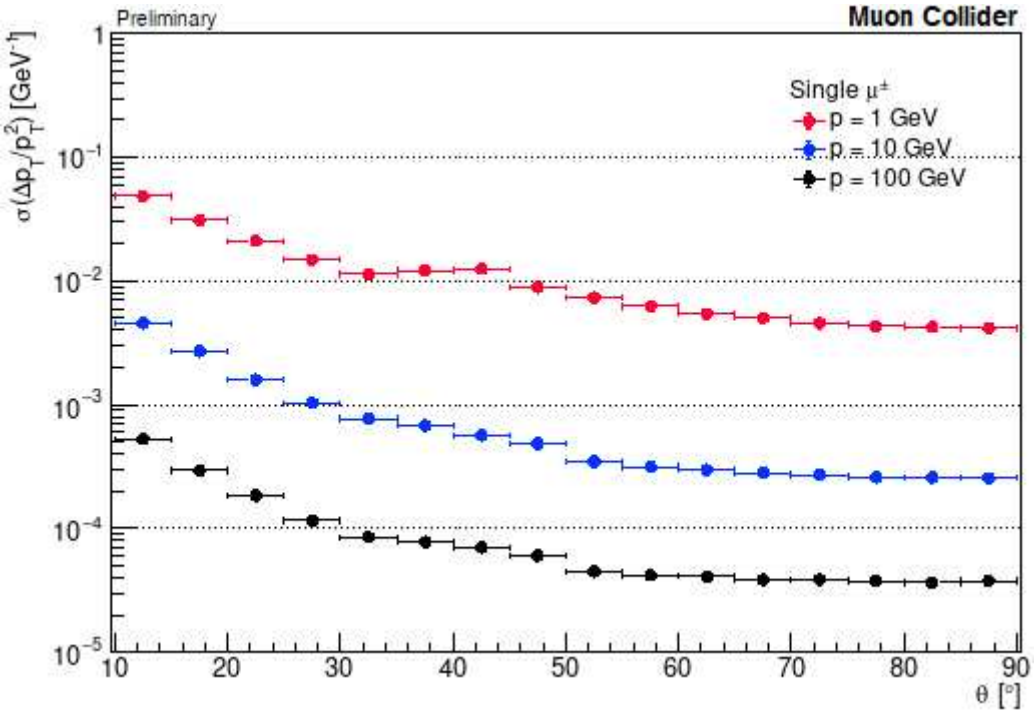

Figure 6.6: Transversal momentum resolution as function of the polar angle, for prompt muons with momentum fixed at 1, 10, 100 GeV. Figure from [52]

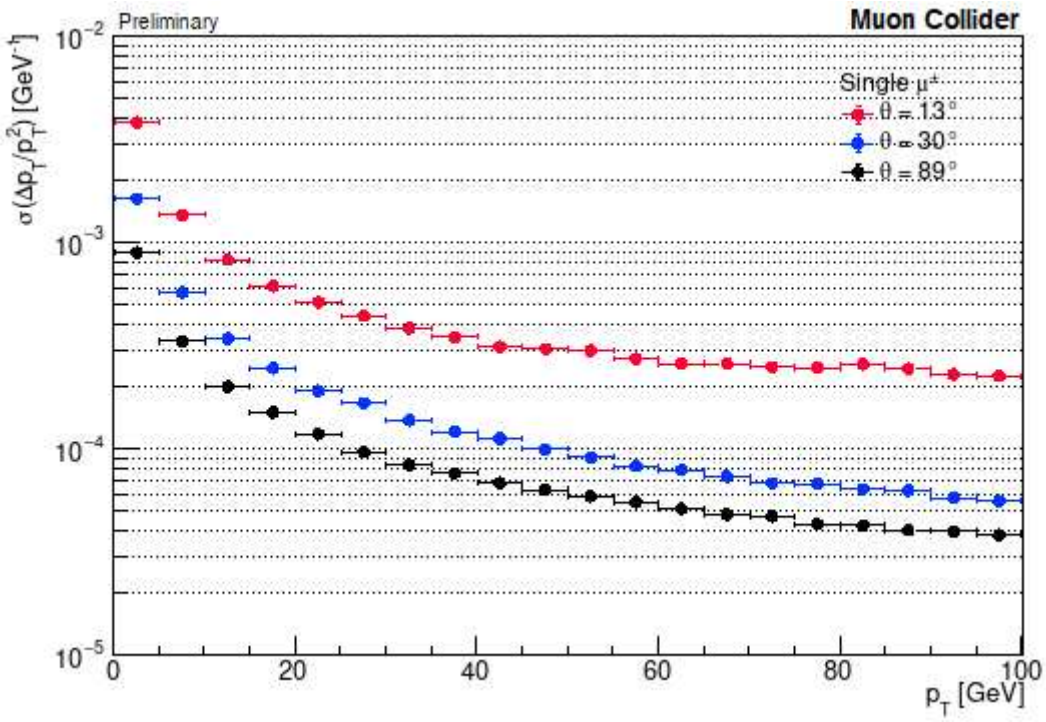

Figure 6.7: Transversal momentum resolution as function of the polar, for prompt muons with θ fixed at 13°, 30°, 89°. Figure from [52]

than 80 GeV in the sample with θ fixed at 89°, while the minimum of $\sim 0.4\%$ occurs in the sample with $\theta = 13°$ in the region of $p_T \in [0,\ 5]\ GeV$.

6.4 BIB effects on tracking performance

As discussed in chapter 5, the BIB consists in a high flux of particles leaving signals in the detector and increasing the combinatorics and this reduces the reconstruction performances. The tracking system is the most affected by this fact because is the closest to the interaction region.

In section 5.2 it has been shown the result that an hit rejection method based on the arrival time can achieve. However, this strategy is not enough to prevent the worsening of the tracking performance and other methods are under studies. For further details see [69] and [70].

In the following paragraphs the tracking efficiency and the transversal momentum resolution are studied using the same samples as in the section above, but with a BIB simulation overlaid.

Efficiency

In figure 6.8 the tracking efficiency is plotted as function of θ. As it can be seen, the BIB mostly affects the region $\theta \lesssim 45°$. In particular for $10° < \theta < 15°$ there is an efficiency drop around 20% for each sample. In the interval $[15,\ 40]°$, the sample with $p = 1\ GeV$ suffers more the BIB effects, in fact, the efficiency drops by about 15-20%, while the worsening of the other two samples is about 5-10%. Instead, for $\theta \gtrsim 45°$ the efficiency reaches a plateau at $\sim 100\%$ for every sample.

The results obtained for higher polar angles is confirmed by figure 6.9. It can be noticed that the sample with $\theta = 89°$ is unaffected by the BIB and the efficiency remains at $\sim 100\%$. Instead, a drop of about 20% occurs for the $\theta = 13°$ sample and about 2% for the last one.

Transversal momentum resolution

In figure 6.10, the resolution on the transversal momentum is plotted as function of the polar angle. Similarly to the tracking efficiency, the BIB effect can be seen in the region $\theta \lesssim 45°$ for the three samples but it differs from the no-BIB case only by less than an order of magnitude. For higher

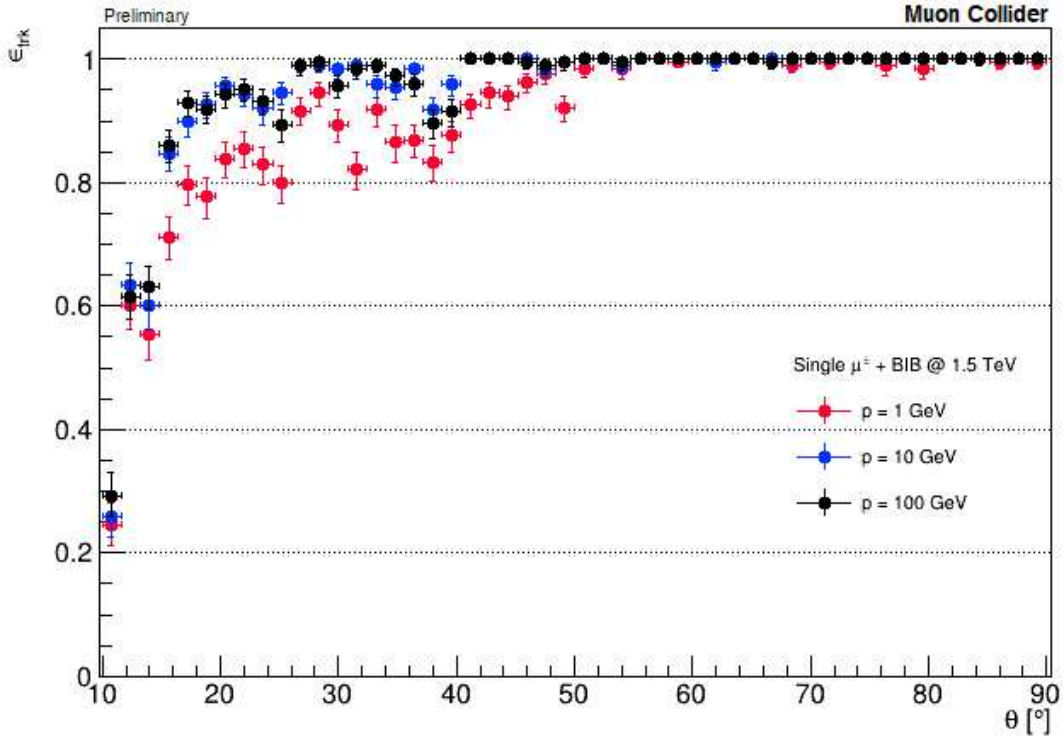

Figure 6.8: Tracking efficiency as function of the polar angle, for prompt muons with momentum fixed at 1, 10, 100 GeV with BIB overlaid. Figure from [52]

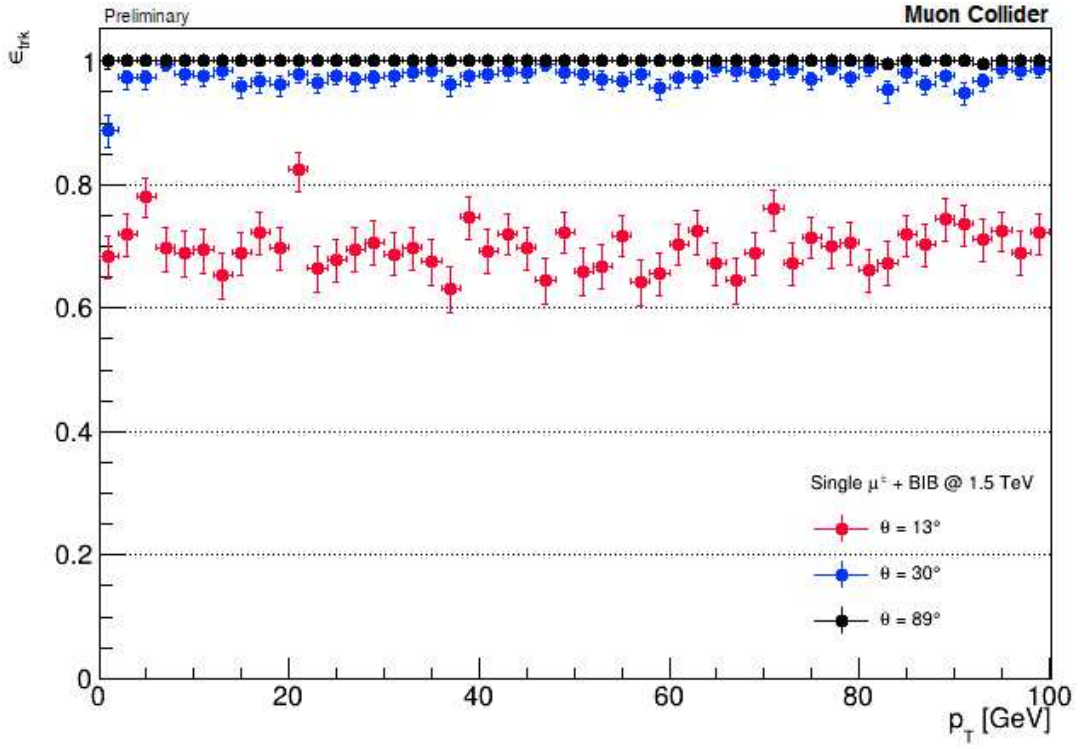

Figure 6.9: Tracking efficiency as function of the transversal momentum, for prompt muons with θ fixed at 13°, 30°, 89° with BIB overlaid. Figure from [52]

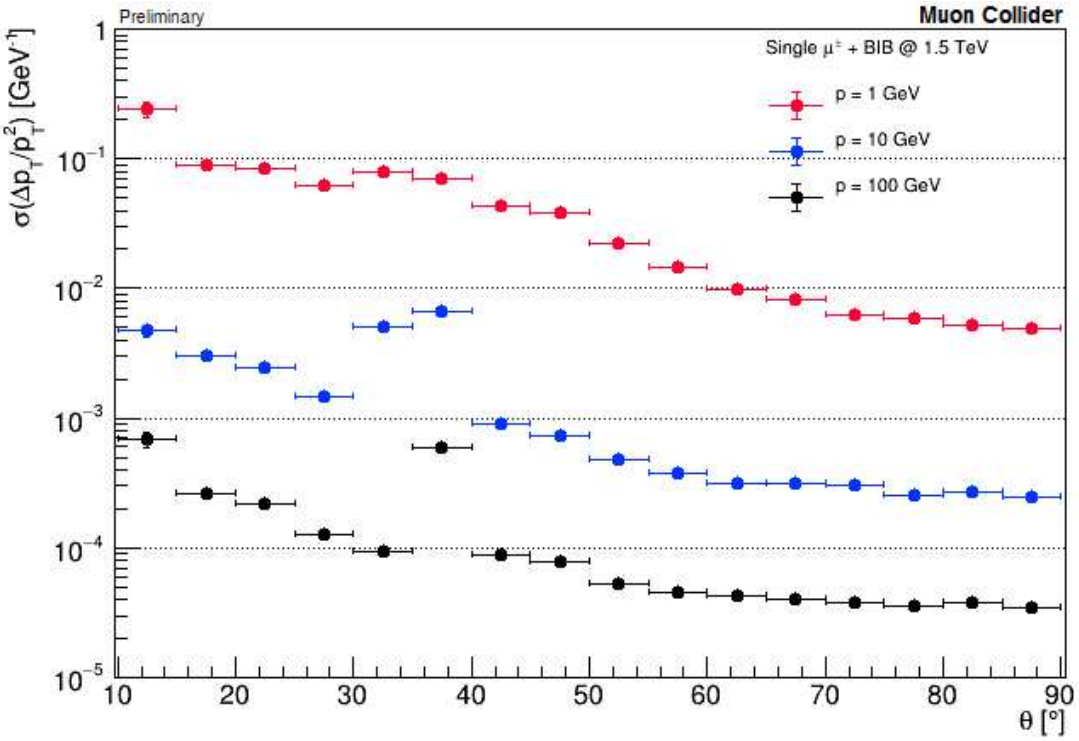

Figure 6.10: Transversal momentum resolution as function of the polar angle, for prompt muons with momentum fixed at 1, 10, 100 GeV with BIB overlaid. Figure from [52]

θ the BIB effects become negligible for the $p = 10\ GeV$ and $p = 100\ GeV$ samples, while it affects the last sample till $\theta \sim 80°$.

Figure 6.11 highlights the fact that the higher is the momentum of the muons, the less the BIB affects the resolution.

It can be noticed that for the $p = 10\ GeV$ and $p = 100\ GeV$ samples at $34 \leq \theta \leq 40°$ the resolution is higher. This behaviour is due to the fact that for these angles the muons do not hit all the layer of the endcap, as it can be seen in figure 6.3. Therefore, in these cases, the track is reconstructed with less information, and the resolution worsens.

The results obtained on resolution and efficiency are good despite the BIB presence and allow to perform physical measurements. However, new reconstruction algorithms which may improve the results presented in this section are under studies.

6.5 Particles and jet reconstruction

Jet reconstruction and particle identification at Muon Collider is performed with the Particle Flow Calorimetry approach, implemented with the PandoraPFA algorithm [71, 72]. The PFA approach consists in the reconstruction of the four-momenta of every visible particle in the event, extracting energy and momentum from the subdetector with the best accuracy. In this way, the momentum of charged particles is obtained from the tracking system and the energy of the neutral ones by the calorimeters, therefore a significant improvement in energy resolution can be achieved. Figure 6.12 gives a schematic view of the particle flow concept[71].

In the next sections the reconstruction with PandoraPFA and the particle identification will be discussed.

6.5.1 PandoraPFA

The PandoraPFA is the algorithm used in the Muon Collider for the particle reconstruction exploiting the particle flow approach. It takes as input the reconstructed tracks and the digitized hits from the calorimeters and it reconstructs the particles in eight steps [72]:

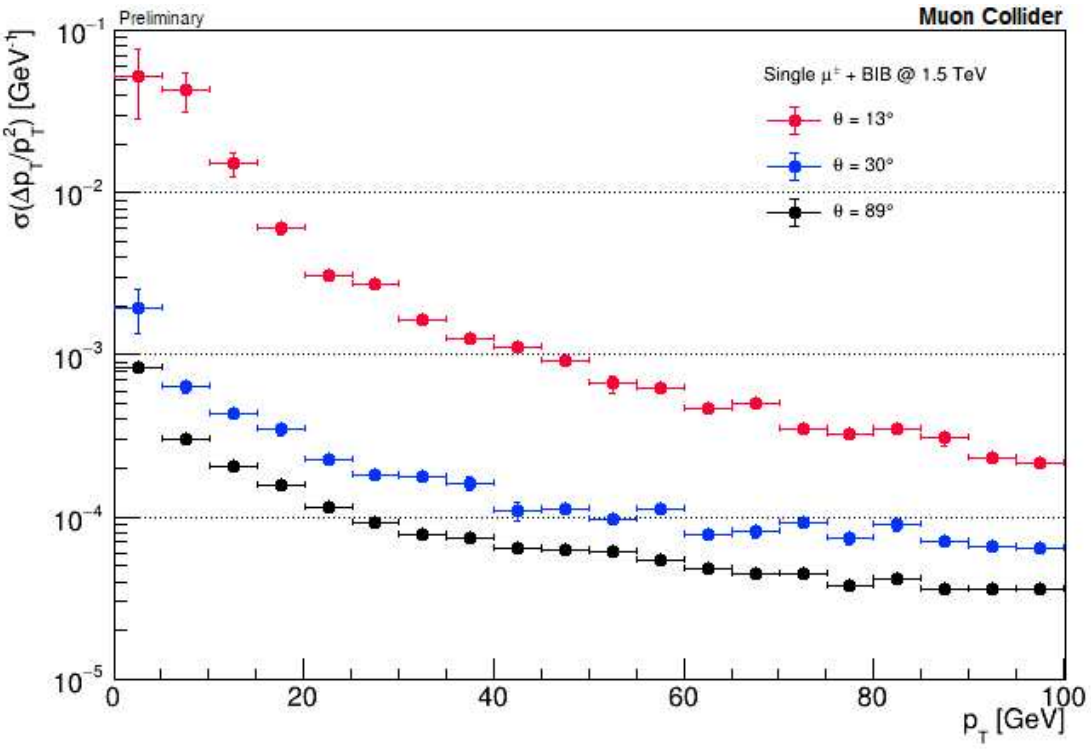

Figure 6.11: Transversal momentum resolution as function of the polar, for prompt muons with θ fixed at 13°, 30°, 89° with BIB overlaid. Figure from [52]

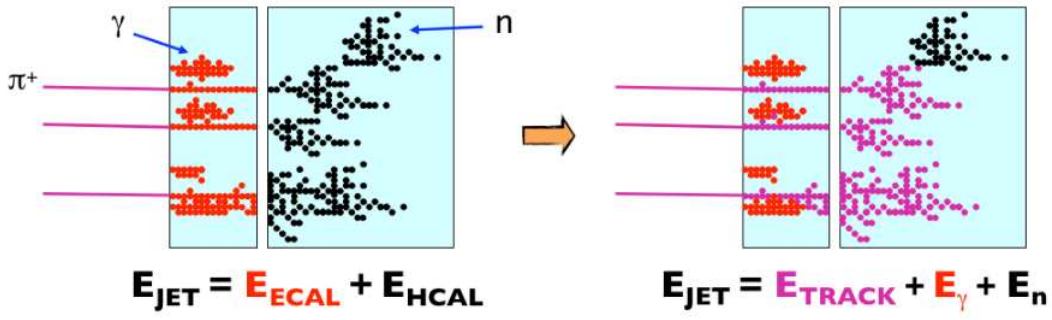

Figure 6.12: Schematic view of the standard calorimetric (left) and particle flow (right) methods. In the first approach the jet energy is measured using only the calorimeters. In the Particle Flow Calorimetry approach the charged particles are measured in the tracking system, which has a greater resolution with respect to the calorimeters, the photon are measured in the ECAL and only the neutral hadrons in the HCAL, which is the detector with the worst resolution. Figure from [71]

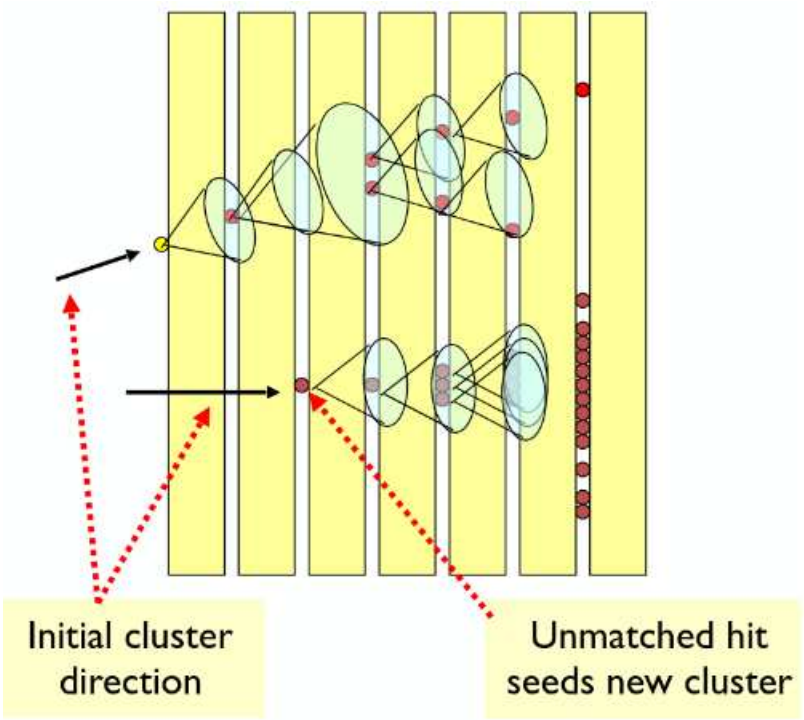

Figure 6.13: Schematic view of cone clustering in PandoraPFA algorithm. Figure taken from [72]

- **Track selection/topology**: tracks are projected into the front face of the electromagnetic calorimeter. Tracks topologies such as kinks (charged particle decaying into a single charged particles plus neutral particles) or decays of neutral particles into a pair of charged particles are identified;
- **Calorimeter Hits Selection and Ordering**: isolated hits, defined by proximity to others, are removed and the remaing hits within each layer of the calorimeter are ordered by their energy;
- **Cone clustering**: hits in the calorimeter are grouped into clusters by a cone based algorithm. Figure 6.13 may give an idea of the working principle. The first hit, the seed, is obtained by projecting a reconstructed track on the ECAL;
- **Topological association**: clusters with specific characteristic are associated together, an example is given in figure 6.14;
- **Reclustering**: clusters are compared with associated tracks. If there are significant discrepancies, the clusters are splitted or merged;
- **Photon identification and recovery**: more sophisticated photon identification algorithm are applied to identify clusters of calorimeter hits which are consistent with photons and to recover photons merged with clusters associated to a hadronic shower;
- **Fragmental removal**: clusters that do not have a track associated, but are not identified as neutral particles, are then considered as fragment of other clusters and treated properly;
- **PFO construction**: the last step produces the outputs, so particles whose energy is calculated from tracks if they are charged or taken from the calorimeters if they are neutral.

6.5.2 Jet identification with BIB overlaid

The particles reconstructed by PandraPFA are used as input for the jet identification, which is performed with the "k_T algorithm", provided by the FastJet package [73]. The algorithm works in three steps:

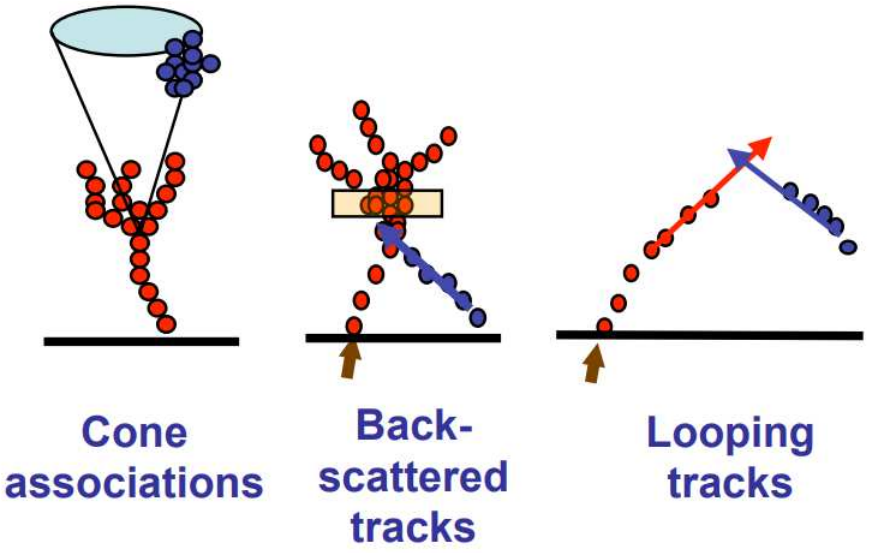

Figure 6.14: Example of clustering association in PandoraPFA algorithm. Clusters are combined on the basis of clear topological signatures, e.g. showers associated with a hadronic interaction, back-scattered tracks and looping minimum ionising calorimeter tracks. Figure taken from [72]

- **Computing the k_T-distance**: for each pair of reconstructed particles the following observable is computed:

$$d_{ij} = min(p_{ti}^2, p_{tj}^2)\frac{\Delta R_{ij}^2}{R^2}$$

where

$$\Delta R_{ij}^2 = (y_i - y_j)^2 + (\phi_i - \phi_j)^2$$

with p_t transversal momentum, y rapidity, ϕ azimuthal angle and R a parameter of the algorithm. In the first and last step of the jet reconstruction is equal to 0.5, while in the second is equal to 0.7;

- the distance from the z-axis is considered as $d_{iB} = p_{ti}^2$;

- the minimum among all the d_{ij} and the d_{iB} is computed. If the minimum is a d_{ij} the particles i and j are merged together and considered as a single particle with 4-momentum equal to the sum of the particles 4-momentum. The algorithm is reiterated till the minimum is d_{iB}. The last particle, obtained by merging the input ones, is the jet and its energy and momentum are the sum of all the particles merged.

Efficiency and resolution are obtained by comparing the Monte Carlo truth and the reconstructed data of a sample of simulated data and they are computed as follow:

$$\epsilon = \frac{N_{MC,matched}}{N_{MC,matched} + N_{MC,unmatched}}$$

where $N_{MC,matched}/N_{MC,matched}$ is the number of true jets matched/unmatched with reconstructed ones;

$$\frac{\Delta p_T}{p_{T,MC}} = \frac{p_{T,MC} - p_{T,reco}}{p_{T,MC}}$$

In figure 6.15 are reported the results obtained. As for the track reconstruction, the performance is not optimized for low momenta jets. However, as for the track reconstruction, efficiency and resolution are good enough to perform physical measurements.

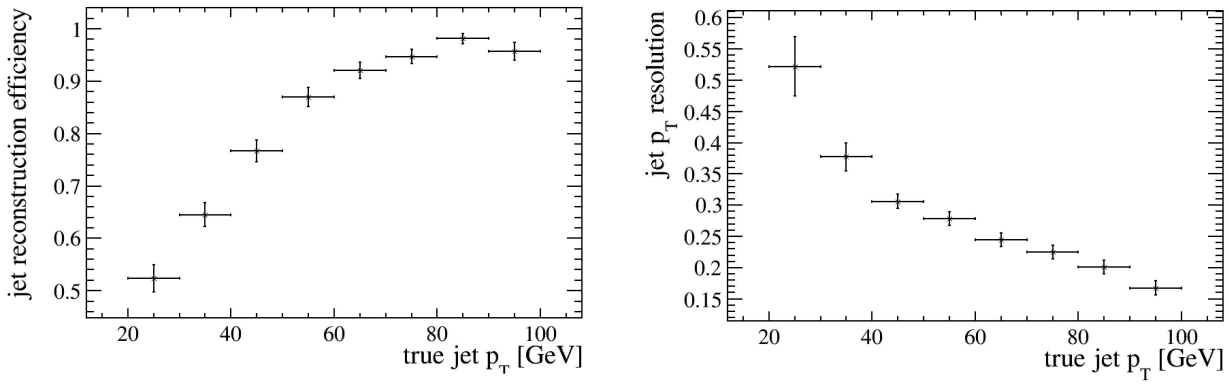

Figure 6.15: Jet reconstruction efficiency (left) and resolution (right) as function of the Monte Carlo transversal momentum of jets. Figure taken from [57]

6.5.3 Muon reconstruction

For the muon reconstruction the performance of PandoraPFA algorithm are not good for muons inside jets, due to the large number of hits inside the calorimeter [74]. In fact, muons leave a small number of hits with respect the other particles of a jet. Therefore a better approach, called "inward projective reconstruction" has been adopted, and it is implemented in the PandoraPFANew framework. In this method first a track made from the hits deposited in the muon system is identified and matched to a track in the tracking system, and then the direction of the track in the tracking system is extrapolated to the track in the muon system [74]. The muon reconstruction is achieved through three steps [74]:

- **Identification of yoke track candidates**: the same clustering algorithm used in the third step of PandoraPFA is applied to the muon system, but it is optimized to deal with the smaller number of layers with respect to the calorimeter (for further details see [74]). If a reconstructed cluster occupy at least 5 layers, it has less than 30 hits and its depth, defined as the difference between the first and the last layer number, is less than 5, then the cluster is considered as a track in the muon yoke;

- **Extrapolation of inner tracks to the muon system**: the tracks are taken and for each of them an helix trajectory is computed using the reconstructed momentum of the track and the magnetic field in the detector. During this process, the change of the magnetic field along the detector is taken into account, in order create a external helix, which is the propagation of the trajectory outside the solenoid;

- **Track matching**: in this step to each yoke track is associated one valid inner track. Valid inner tracks are inner tracks which respect the following requirements:

  - the track momentum is $> 7\ GeV$;
  - the angle between the direction of the external helix at its entry point to the muon system and the direction of the yoke track is $< 0.2\ rad$;
  - the distance of closest approach between the helix and the cluster (i.e. the shortest distance of the external helix to the mean position of the hits in the innermost layer of the yoke track) is < 200 mm.

  The valid track with the minimum distance of closest approach with a yoke track is matched with that yoke track.

The performance in terms of efficiency and transversal momentum resolution are reported respectively in figure 6.16 and 6.17. The efficiency is defined as:

$$\epsilon = \frac{N_{MC,matched}}{N_{MC,matched} + N_{MC,unmatched}}$$

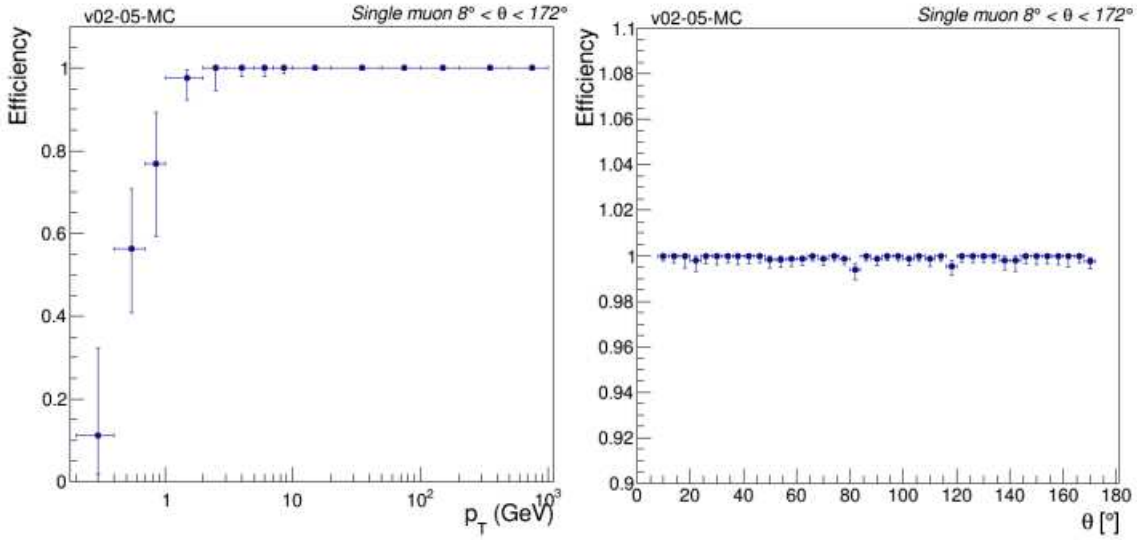

Figure 6.16: Muon reconstruction efficiency as function of transversal momentum (left) and polar angle (right). The sample has no BIB overlaid and the muons are generated with a polar angle in the range [8°, 172°]. Outside this range it is not possible to reconstruct muons due to the presence of the nozzles. Plot taken from [75]

where $N_{MC,matched}/N_{MC,matched}$ is the number of montecarlo muons matched/unmatched with reconstructed ones. The resolution is defined as:

$$\frac{\Delta p_T}{p_{T,MC}} = \frac{p_{T,MC} - p_{T,reco}}{p_{T,MC}}$$

The plots shows that the efficiency is $\sim$ 100% for muons with $p_T > 0.1\ GeV$ and for each θ considered. The efficiency drops for low momentum muons.

The resolution is of the order of 10^{-3} for low momentum muons and it improves to $\sim 10^{-4}$ for higher transversal momentum.

The plot presented in this section are obtained from a sample without BIB overlaid, however, as discussed in section 5.2, the BIB effects in the muon system are negligible, therefore no serious issues are expected for muon reconstruction.

The muon identification during the analysis is performed just by requiring that a particle has a track matched with a track in the muon system. This is not optimal because other particles can leave signal in the muon system. These particles are called "fake muons". New identification algorithm are under studies.

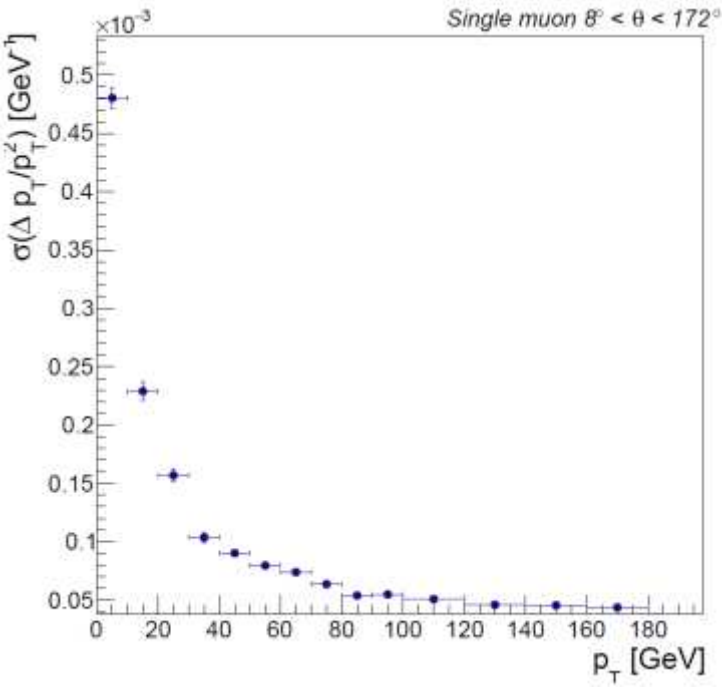

Figure 6.17: Muon reconstruction resolution as function of the transversal momentum of the muon. The sample has no BIB overlaid and the muons are generated with a polar angle in the range [8°, 172°]. Outside this range it is not possible to reconstruct muons due to the presence of the nozzles. Plot taken from [75]

Chapter 7

Reconstruction and identification of the $H \to WW^*$ process

In this chapter the analysis performed to estimate the precision with which it is possible to perform the measurement of the cross section of the process $\mu^+\mu^- \to H + X \to WW^* \to \mu\nu qq'$ is reported. Here "X" can be $\nu\overline{\nu}$, as result of WW-fusion, or $\mu^+\mu^-$ as result of ZZ-fusion. The analysis has been performed following four steps that will be discussed in a dedicate section:

- **Samples generation**: signal and relevant physical backgrounds production;
- **Pre-selection requirements**: requests on the events have been studied in order to discard physical background events;
- **Topology study of events**: the topology of signal and background events have been compared in order to understand which observable are suited for signal to background discrimination;
- **Multivariate analysis description**: by exploiting the Toolkit for Multivariate Data Analysis (TMVA) package, a machine learning (ML) algorithm has been used to separate signal from background.

7.1 Samples preparation

For the studies of this thesis, several samples were generated using two different Monte Carlo, namely, PYTHIA and WHIZARD, as mentioned in section 6.1. In the latter case, the hadronization process is performed with PYTHIA. In a first moment, only the signal and the main physical background, $\mu^+\mu^- \to WW^* \to \mu\nu qq$ have been generated, in order to compare the generation tools. Therefore, the four samples generated were:

- **Signal with PYTHIA Monte Carlo**: a sample of 10000 events $\mu^+\mu^- \to H\nu\overline{\nu} \to WW^*\nu\overline{\nu} \to \mu\nu + X + \nu\overline{\nu}$ at $\sqrt{s} = 3\ TeV$ has been produced using PYTHIA [59]. The muon in the final state has been required to have a transversal momentum $p_T > 10\ GeV$. X means everything, i.e. one of the two W boson was bind to decay into a muon and a neutrino, while the other one was let free. Therefore, not the entire sample was relevant for the studies of this thesis, because the desired final state requires one W boson to decay into a muon and in a neutrino and the other W boson to decay into a couple of quarks. The branching ration of $W \to qq'$ is 67.41% [76], therefore about 6700 events out the total sample were interesting for this study;

  It is important to remind the fact PYTHIA considers only diagrams at the Leading Order;

- **Main physical background with PYTHIA Monte Carlo**: a sample of 10000 events of the main physical background events. In this case the selected process was $\mu^+\mu^- \to WW^*\nu\overline{\nu} \to \mu\nu + X + \nu\overline{\nu}$ at $\sqrt{s} = 3\ TeV$. As for the signal, only the decay of one out two W bosons has been forced to a muon. The only background processes relevant for the study of this thesis are the ones with the same final state as the signal, therefore only the 67.41% generated event were interesting for this study;

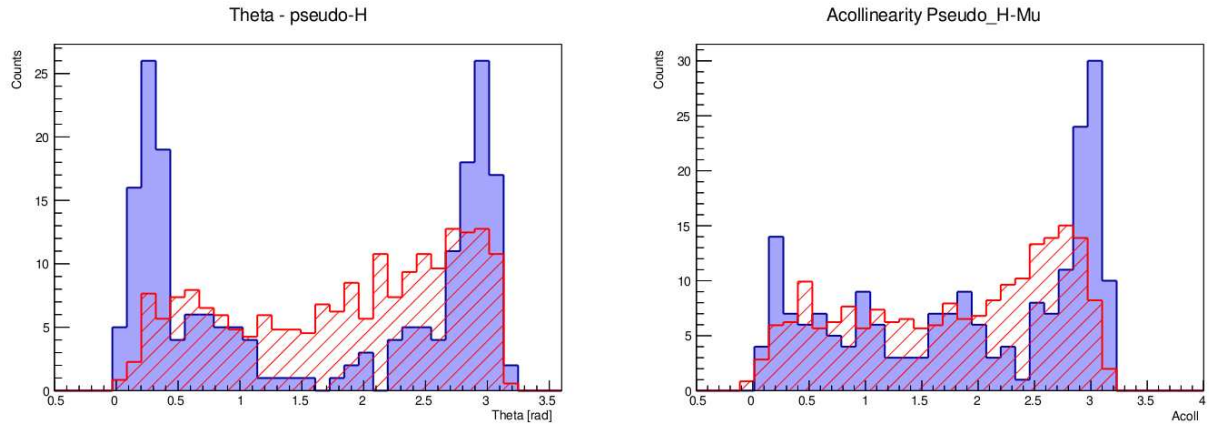

Figure 7.1: Comparison between the reconstructed sample of main background generated with WHIZARD (blue) and PYTHIA (red). On the left is presented the polar angle of the *pseudo-H*, on the right there is the acollinearity between *pseudo-H* and μ. In each plot the histograms are normalized to the same area, i.e. the area of the WHIZARD sample

- **Signal with WHIZARD Monte Carlo**: a sample of 2000 events $\mu^+\mu^- \to H\nu\overline{\nu} \to WW^*\nu\overline{\nu} \to \mu\nu qq\nu\overline{\nu}$ at $\sqrt{s} = 3\ TeV$ has been generated with WHIZARD. "q" indicates a generic quark with different flavors. The main difference with PYTHIA is that WHIZARD includes higher order diagrams.

- **Background with WHIZARD Monte Carlo**: a sample of 10000 events $\mu^+\mu^- \to \mu\nu qq$ at $\sqrt{s} = 3\ TeV$ has been generated with WHIZARD requiring the muon in the final state to have a transversal momentum greater than 10 GeV. This requirement has been imposed to remove events that will not enter in the analysis sample.

The signal samples show the same behavior within statistical fluctuation, but significant differences appear for the background, in particular for the angular related observables. Figure 7.1 shows the comparison of the WHIZARD background sample (blue) and PYTHIA background sample (red) for two observables. These observables are taken as example and their definition will be given in the next section, for the moment it is enough to see the different behaviour in the two samples.

PYTHIA does not include all the processes present in WHIZARD. The plots in figure 7.1 enlighten the fact that something relevant is missing. The analysis is performed by using WHIZARD samples, while PYTHIA samples are used only for some controls when specified. The background processes considered relevant are reported below. For each, a sample of 10000 events has been generated.

- $\mu^+\mu^- \to H\nu\overline{\nu} \to WW^*\nu\overline{\nu} \to qqqq\nu\overline{\nu}$;
- $\mu^+\mu^- \to H\nu\overline{\nu} \to b\bar{b}\nu\overline{\nu}$;
- $\mu^+\mu^- \to H\nu\overline{\nu} \to \tau^+\tau^-\nu\overline{\nu}$;
- $\mu^+\mu^- \to qqll$;
- $\mu^+\mu^- \to qq\nu\nu$.

From now on, the set of background events which do not have the Higgs boson production is called "no-Higgs sample", while the "Higgs sample" refers to the set of background events that have the Higgs boson.

The Higgs boson production mechanism considered in the samples above is the WW-fusion, which is the main process, as shown in figure 2.5, and it occurs $\sim 90\%$ of the times. However, at $\sqrt{s} = 3\ TeV$, also the $\sim 10\%$ due to the ZZ-fusion is relevant and it has to be taken into account.

Producing the all the samples with the ZZ-fusion would have been challenging in terms of time and computational resources. Therefore a different approach has been adopted. Only the signal process $\mu^+\mu^- \to ZZ\mu^+\mu^- \to H\mu^+\mu^- \to WW^* + \mu^+\mu^- \to qq\mu\nu + \mu^+\mu^-$ has been generated. The two signal

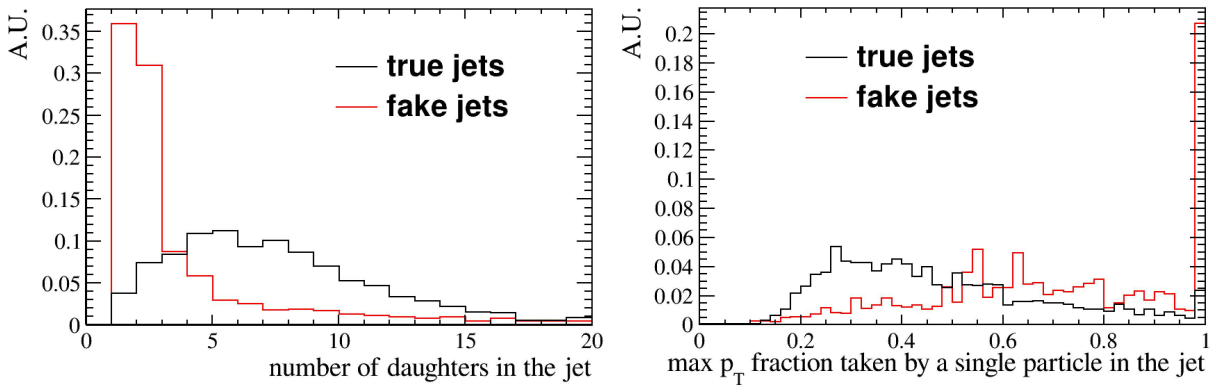

Figure 7.2: On the left the number of daughters particle per jet (black) and fake jet(red). On the right the jet maximum transversal momentum fraction carried by a single daughter.

samples with the different Higgs boson production mechanism have been compared. The topology of the events were compatible within statistical fluctuation, as it is expected from the fact that the characteristic momentum of neutrinos (in case of WW-fusion) and muons (in case of ZZ-fusion) is much larger than their masses. Therefore it has been assumed that the event selection does not depend on the Higgs boson production mechanism and the results concerning the expected number of events at the Muon Collider were computed using the total Higgs production cross section. The comparison of the observables can be found in appendix A.

7.2 Pre-selection requirement

In order to keep the signal and discard the physical background, each event has to satisfy several requirements.

The first cuts presented are the so-called "jet quality cuts", namely:

- $N_{daughters} > 2$
- $p_{ratio} < 0.8$

where $N_{daughters}$ is the number of particles which lay inside the associated jet, while p_{ratio} is the maximum fraction of the jet momentum carried by a single daughter.

These cuts aim to remove the fake jets, namely hits due to combinatorics reconstructed as jets by the algorithm, caused by the presence of the BIB. In figure 7.2 the two variables have been plotted comparing jets and fake jets. Actually in the right figure $p_{T,\ ratio}$ is defined using the transversal momentum instead of the total momentum as in this thesis.

It can be seen that most of the fake jets have one or two daughters, therefore the requirement is able to discard the majority of fake jets. When there is only one daughter, it carries the whole momentum of the jet, therefore $p_{ratio} = 1$. This explain the peak at $p_{ratio} = 1$ in figure 7.2. Also in the region $p_{ratio} > 0.8$ the amount of fake jets is relevant, doubled with respect to the true ones, therefore this cut has been adopted.

The third cut presented in this section concerns the number of muons in the final state, namely:

- $N_{muons} \geq 1$

because in the desired final state there must be at least one muon, the product of the W boson decay. However, other muon may arise from the BIB events or from jets, therefore, only a lower bound has been fixed.

The muons produced by the W boson decay usually have a transversal momentum of few tens of GeV, while muons coming from other sources, i.e. BIB or jets, mostly have low transversal momentum, as it can be seen in figure 7.4. Therefore a cut on the transversal momentum of the muon has been implemented, namely:

- $p_{T,\ Muons} > 10\ GeV$

The nozzles in the very forward region absorb particles produced at low polar angles, therefore a cut concerning the muon polar angle has been implemented:

- $\theta_\mu > 10°$ and $\theta_\mu < 170°$

It is particularly interesting to see how the muon cuts affect the samples. In figure 7.3 the signal (in blue) has been compared to the backgrounds (in red). On the left is presented the comparison with the no-Higgs sample, on the right the comparison with the Higgs sample. As it can be seen, in both background sample there is a significant amount of events in which there is not a muon that fulfill the requirements, therefore those events are discarded.

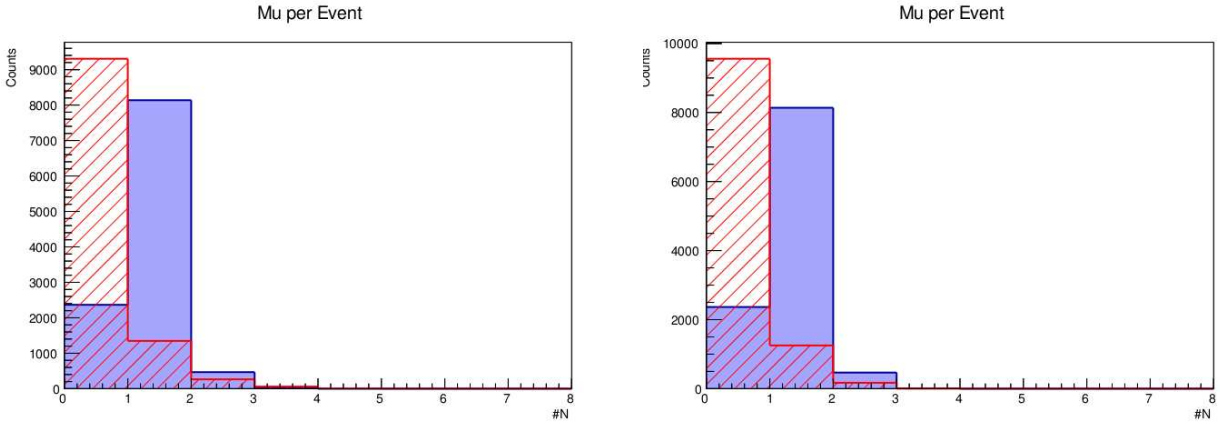

Figure 7.3: Number of muons with $p_T > 10\ GeV$ per events. On the left the signal (in blue) has been compared to the no-Higgs sample, on the right to the Higgs sample. Both plot are normalized to the area of the signal sample.

As shown in figure 7.3, there great majority of events in signal and backgrounds have one or zero muons, but, in case more than one is detected, the algorithm have to choose the one coming from the W boson. The criterion adopted in this thesis is the isolation. For each muon, the ΔR (defined in equation 7.1) of the muon with each jet is computed. Then the jet with the minimum ΔR is considered. If $\Delta R < 0.5$, the muon isolation is defined as $\frac{pt_\mu}{pt_{jet}}$. Otherwise, if the $\Delta R > 0.5$, the muon lays outside the jet cone and is considered isolated, therefore the isolation is fixed to 1. The muon with the maximum isolation is chosen as the muon coming from the W boson decay and kept in the analysis.

$$\Delta R_{i,j} = \sqrt{(\eta_{jet} - \eta_\mu)^2 + (\phi_{jet} - \phi_\mu)^2} \tag{7.1}$$

with ϕ the azimuthal angle and η the pseudo-rapidity:

$$\eta = -ln\left[tan\left(\frac{\theta}{2}\right)\right] \tag{7.2}$$

Another interesting aspects of cut on the transversal momentum of the muon is that it is able to discard a significant fraction of fake muons and particles from BIB that leave signal in the muon detector. This fact can be understood by looking at the plot in figure 7.4. The muon coming from the W boson decay (on the left) is separated from every other particle tagged as a muon by the algorithm (on right). These particles can be muons coming from hadrons decay in jets which leave signal in the muon system or fake muons.

The separation has been done using the Monte Carlo truth, which allows to know from which particle the selected one comes from.

In the plots the transversal momentum has been plotted for signal (blue) and main physical background (red) using the PYTHIA samples.

It is clear that a significant fraction of particles tagged as muons that are not from W boson decay are cut out by the muon p_T requirement.

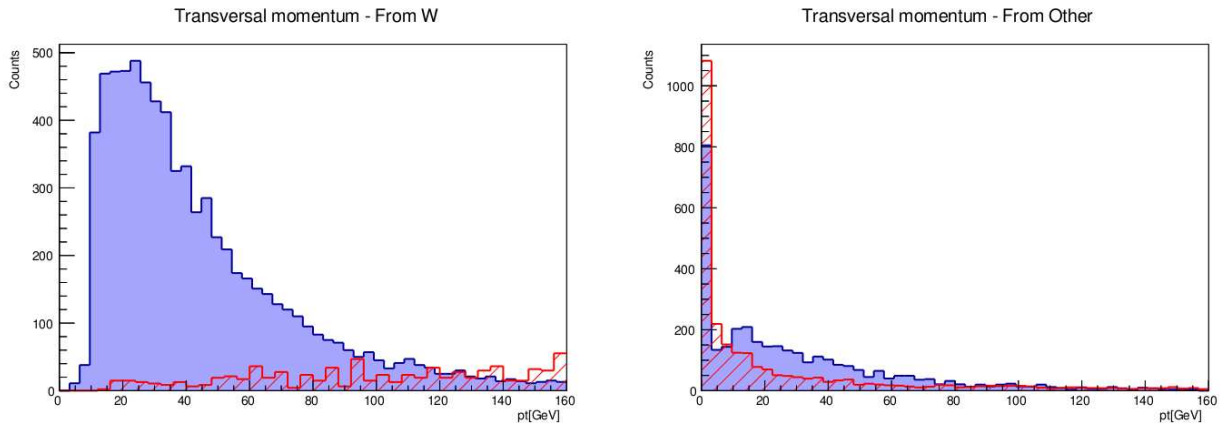

Figure 7.4: Monte Carlo transversal momentum of muons produced by W boson decay (left) and from jets (right). In blue it is shown the signal, in red the physical background, normalized to the same area. The distributions are zoomed at low momenta. Each plot is normalized to the area of the signal.

Once the quality cuts are applied, the algorithm proceeds analysing only the survived jets and it asks:

- $N_{jets} \geq 2$

This requirement fix a lower bound in the jets number because additional jets may be produced as consequence of gluons emission.

In order to discard jets close to the nozzles a cut on the jets pseudorapity has been implemented:

- $|\eta_{Jets}| < 2.5$

For each pair of jets, the algorithm computes the W boson invariant mass and selects the pair of jets which minimizes the deviation from the nominal one.

In table 7.1 signal pre-selection efficiency of the cuts are reported. The first row shows the effect

Cuts	Efficiency [%]
Quality, N_μ, N_{jet}	38.7
Quality, N_μ, N_{jet}, pt_μ	29.0
All cuts	29.0

Table 7.1: Pre-selection efficiency on the signal sample depending on cuts. Only the quality cuts, the requirements on the number of particles and the cut on the muon transversal momentum affects the efficiency. The other cuts, as it can be seen in the third row of the table, are irrelevant on the signal sample.

of the application of quality cuts and the requirements on number of muons and jets in the final state. These cuts are crucial because the quality cuts remove fake jets that cannot be included in the analysis, while the others establish the minimum number of particles needed in the final state. These requirements lead to an efficiency of 38.7%.

The only other relevant cut, concerning the signal, it the one on the muon transversal momentum which reduces the efficiency down to 29.0%. The other cuts do no affect the signal efficiency.

To better understand these results, the signal sample without the BIB has been studied. In this case, the quality cuts are not needed, because there cannot be fake jets caused by BIB.

The results are reported in table 7.2. The final efficiencies on the two samples are similar. It can be notice that the cut on the transversal momentum of jets is particularly effective on the sample without the BIB overlaid. This behaviour enlightens the fact that the quality cuts which act on the BIB sample remove the jets with low momentum.

At this point, an estimation of the expected number of events at the Muon Collider can be calculated by the formula:

Cuts	Efficiency [%]
N_μ, N_{jet}	71.0
N_μ, N_{jet}, pt_μ	60.9
N_μ, N_{jet}, pt_μ, pt_{jet}	30.4

Table 7.2: Pre-selection efficiency on the signal sample without BIB depending on cuts

Process	ϵ_{pre}[%]	σ $[fb]$	Expected Events
$\mu^+\mu^- \to H\nu\overline{\nu} \to WW^*\nu\overline{\nu} \to qq\mu\nu\nu\overline{\nu}$	29 ± 1	17.3	5020 ± 190
$\mu^+\mu^- \to\to qq\mu\nu$	6.5 ± 0.3	$5.02 \cdot 10^3$	$(326 \pm 12) \cdot 10^3$
$\mu^+\mu^- \to\to qqll$	2.3 ± 0.2	$1.04 \cdot 10^3$	$(24.3 \pm 1.5) \cdot 10^3$
$\mu^+\mu^- \to\to qq\nu\nu$	4.6 ± 0.3	$1.56 \cdot 10^3$	$(72 \pm 4) \cdot 10^3$
$\mu^+\mu^- \to H \to WW^* \to qqqq$	3.9 ± 0.2	108	4250 ± 210
$\mu^+\mu^- \to H \to bb$	1.1 ± 0.2	313	3600 ± 800
$\mu^+\mu^- \to H \to \tau\tau$	0.3 ± 0.1	34.3	93 ± 21

Table 7.3: Pre-selection efficiency, cross section and expected events for signal and background events.

$$N_{events} = \mathcal{L} \cdot \sigma \cdot \epsilon \tag{7.3}$$

were $\mathcal{L}$ is the integrated luminosity, σ is the cross section of the process considered and ϵ the selection efficiency.

Assuming $\mathcal{L} = 1\ ab^{-1}$, achievable in about two years, and the pre-selection efficiency, namely:

$$\epsilon_{pre} = \frac{N_{after\ cuts}}{N_{total}} \tag{7.4}$$

the expected number of events for each process has been reported in table 7.3.

The error on the expected number of counts is obtaining by:

$$\sigma_{N_{events}} = \mathcal{L} \cdot \sigma \cdot \sigma_\epsilon \tag{7.5}$$

where σ_ϵ is the error on efficiency calculating using a Bayesian approach [77].

The probability $P(\epsilon;\ k, n)$ that ϵ is the true efficiency, given the number of selected events k and the total number of event n is:

$$P(\epsilon;\ k, n) = \frac{P(k; \epsilon, n) \cdot P(\epsilon; n)}{C} \tag{7.6}$$

where:

- $P(k; \epsilon, n)$ is the probability of having k selected events giving a certain efficiency ϵ and total number of event n. It follows the binomial distribution, therefore

$$P(k; \epsilon, n) = \frac{n!}{k!(n-k)!}\epsilon^k(1-\epsilon)^{n-k} \tag{7.7}$$

  ;

- $P(\epsilon; n)$ is the so-call Prior probability, namely the probability of having ϵ giving the total number of event n. $P(\epsilon; n)$ is assumed uniform in [0, 1];

- C is the normalization constant and it can be proven that $C = \frac{1}{n+1}$

Therefore,

$$P(\epsilon;\ k, n) = \frac{(n+1)!}{k!(n-k)!}\epsilon^k(1-\epsilon)^{n-k} \tag{7.8}$$

From the formula above it is possible to compute the variance $V(\epsilon) = \sigma_\epsilon^2$:

$$V(\epsilon) = \sigma_\epsilon^2 = \frac{(k+1)(k+2)}{(n+2)(n+3)} - \frac{(k+1)^2}{(n+2)^2} \tag{7.9}$$

The entire derivation can be found in [78].

7.3 Topology of the events

In this section all the observables studied are presented. The goal here is to understand the differences between signal and physical background. This work allows to choose which observables has to be given as input to the machine learning algorithm to perform the discrimination.

The observables are separated in two categories: momentum-related and angular related and for each observable two plots will be presented. The one on the left compares the signal with the no-Higgs background, the one on the right, instead, has the signal compared to the Higgs background. In both plots the signal will be in blue and the background in red. Each plot will be normalized to the area of the signal histogram.

Before proceeding , it is import to specify the notations adopted in this thesis. In each event there are two W bosons, but only the one which decays hadronically can be reconstructed. In the final state there are three neutrinos, two coming from the Higgs boson production through WW-fusion, $\mu^+\mu^- \to H\nu\overline{\nu}$, one coming from the W boson leptonic decay, $W \to \mu\nu$. The neutrino in the experiments are reconstructed from the missing momentum. In this case it is not possible because the missing momentum is the sum of three particles and information about a single one of them cannot be retrieve and the W boson which decay leptonic cannot be reconstructed. Therefore, for the rest of the thesis, the W boson which decays hadronically is simply indicated as W.

As consequence, the Higgs boson cannot be reconstructed either. However, observables related to the Higgs are crucial to separate signal from background. In the following paragraphs, with *pseudo-H* it is intended the Higgs boson without the contribution of the neutrino or, in other words, the sum of the 4-momentum of the W and the μ.

7.3.1 Momentum-related observables

The first observable studied was the invariant mass of the W. It is computed with the following formula:

$$m_W = \sqrt{(E_{jet1} + E_{jet2})^2 - (\overrightarrow{p}_{jet1} + \overrightarrow{p}_{jet2})^2} \tag{7.10}$$

In figure 7.5 the m_W distributions for signal and background are superimposed. On the top there are the full spectrum for no-Higgs and Higgs background, while on the bottom the region around the nominal mass of the W boson is zoomed.

The W boson invariant mass histogram of the signal sample shows two different distributions. The first one at low invariant mass, the other one around the nominal mass of the W boson. This behaviour is expected due to the Higgs boson decay in one W boson on shell and one W boson off-shell. In the plots in figure 7.5 only the W boson which decay hadronically. Half of the times it will be the W boson, the other half the W^* boson, causing the distribution showed.

The Higgs background does not manifest the same behaviour, instead there is single peak at $\sim 80\ GeV$. The most relevant component in this background is due to $\mu^+\mu^- \to H\nu\overline{\nu} \to WW^* \to qqqq$. In this case both W boson decay hadronically and could be reconstructed by the algorithm, however, the selection criterion adopted searches for the particle that minimize the distance from the nominal mass of the W boson, therefore it will always select the W boson produced on-shell.

A peak is visible also in the no-Higgs sample, where the main component of this sample is given by the process $\mu^+\mu^- \to WW\nu\overline{\nu} \to\ \mu\nu qq\nu\overline{\nu}$, where both W boson are produced on-shell, however, the

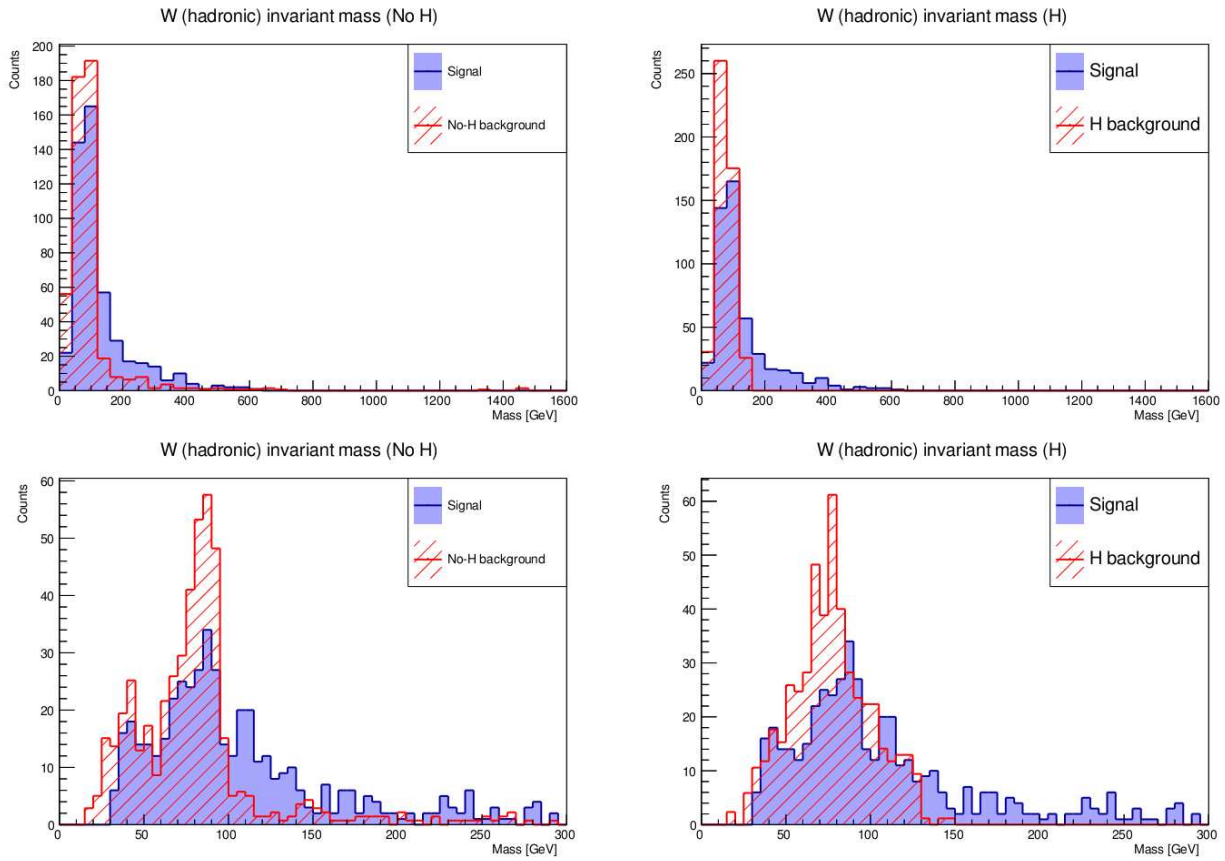

Figure 7.5: Invariant mass of W for signal (blue) and background (red). On top the full distribution for no-Higgs background (left) and Higgs background (right). On bottom the same distributions are zoomed around the region of W boson nominal mass The histograms are normalized to the same area.

other contributions affect this peak inducing a large number of counts in the region below the nominal mass of the W boson, and a lower number in the region above.

The second observable studied was the invariant mass of the *pseudo-Higgs* that is, remembering the definition given above, the four-momentum sum of the W and the μ, therefore the invariant mass is defined as:

$$m_{pseudo\ H} = \sqrt{(E_W + E_\mu)^2 - (\overrightarrow{p}_W + \overrightarrow{p}_\mu)^2} \tag{7.11}$$

and its spectrum is reported in figure 7.6, the full view on top left and the zoom on the first 500 GeV on the bottom.

The plots on the left have predictable shape. The signal shows a resonance peaked around the mass of the Higgs boson. The constrains on the momentum of jets and muon forbid these plots to have a tail on the left, at very low energies.

The no-Higgs background shows a peak caused by the W boson, in fact it is centered at lower energies with respect to the signal.

In the Higgs background events the muon selected arise from the jets, therefore most of the times it will have a low four-momentum with respect to the di-jet and its contribution to the mass of the *pseudo H* will be negligible. Therefore, the invariant mass is computed using only the information on one W boson. In fact the plot present a peak on $\sim 80\ GeV$.

The next set of observables presented are the transversal momenta of W, *pseudo H* and μ. Figure 7.7, 7.8 and 7.9 show the three distributions. A common behavior may be notice. Each particle has a lower p_T in the signal with respect to the physical background. The only plot which does not respect this behaviour is the transversal momentum of the muon in the Higgs background. In this case, the muon is produced by hadron decay in a jet, therefore it is expected to have a lower momentum.

Another momentum-related observable studied is the missing transversal momentum, due to the

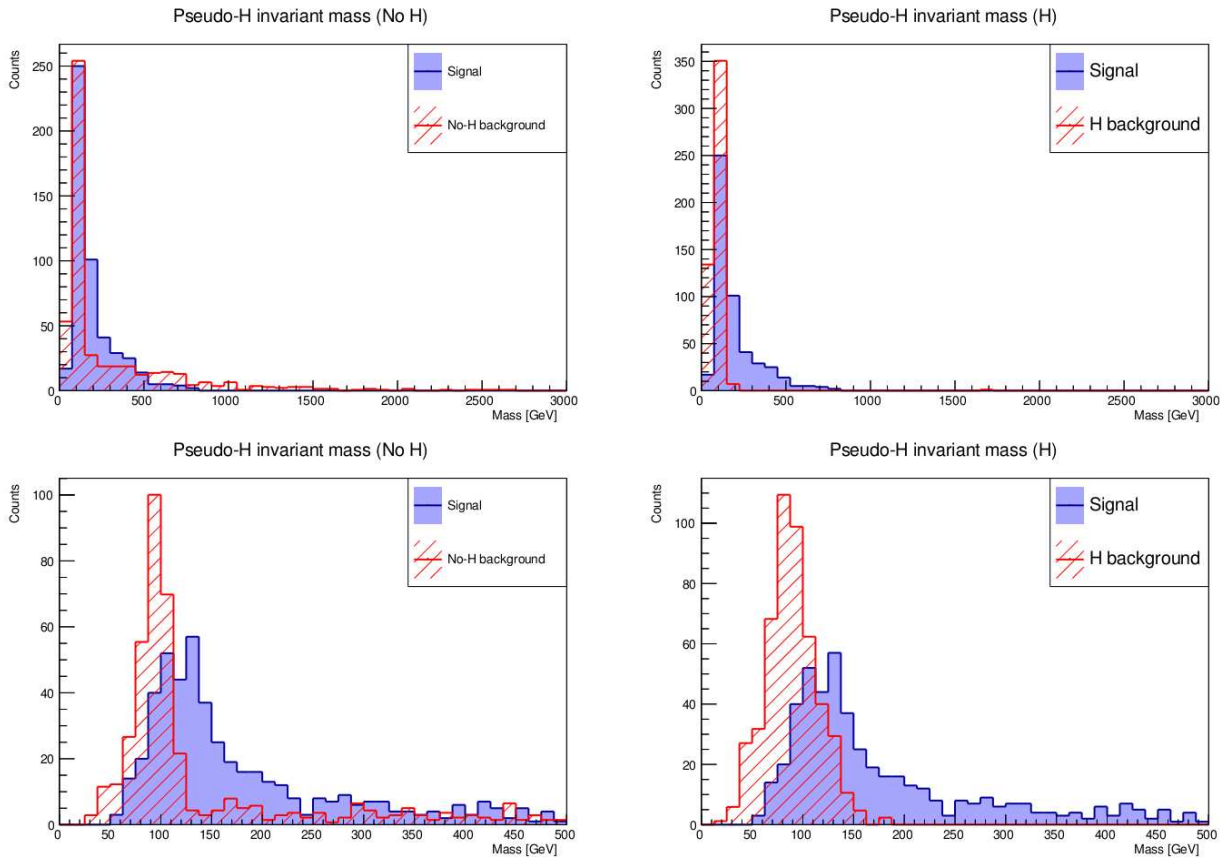

Figure 7.6: Invariant mass of *pseudo H* for signal (blue) and background (red). On top the full distribution for no-Higgs background (left) and Higgs background (right). On bottom the same distributions are zoomed around the region of W boson nominal mass The histograms are normalized to the same area.

three neutrinos produced in the event. It is defined as:

$$p_{t,\ miss} = -\sqrt{(p_x^2 + p_y^2)} \tag{7.12}$$

where

$$p_{x,y} = p_{x,y,mu} + \sum_{jets} p_{x,y,jet}$$

The distribution is reported in figure 7.10. The signal show a peak at very low momenta, while the background goes even close to 3 TeV, which is the center of mass energy of the collision. The next observable presented is the number of isolated muons in the event. A muon is tagged as "isolated" when the $\Delta R > 0.5$ for each jet which survives the quality cuts. The distributions are reported in figure 7.11. The last observable studied is sum of the number of daughters in the two jets selected for the W boson reconstruction. The plots are reported in figure 7.12. The last two variables presented are remarkably different between signal and Higgs background.

7.3.2 Angular-related observables

The second category of observables is the so-called angular related. The fact that the Higgs boson is a spin-0 particle, suggests that the angular related observable could be particularly useful in the no-Higgs background discrimination, where the Higgs boson is not produced.

The first observables are the polar angles of the W, the *pseudo H* and the μ with respect to the beam axis. The plots are reported in figure 7.13, 7.14 and 7.15. In the plot 7.13 it is difficult to notice significant differences in the no-Higgs case, while in the other an abundance with respect to the signal is present at low angles. A similar behaviour can be seen in both plots of figure 7.14. In this case, for the no-Higgs background, there is an evident difference also in the central region of the spectrum,

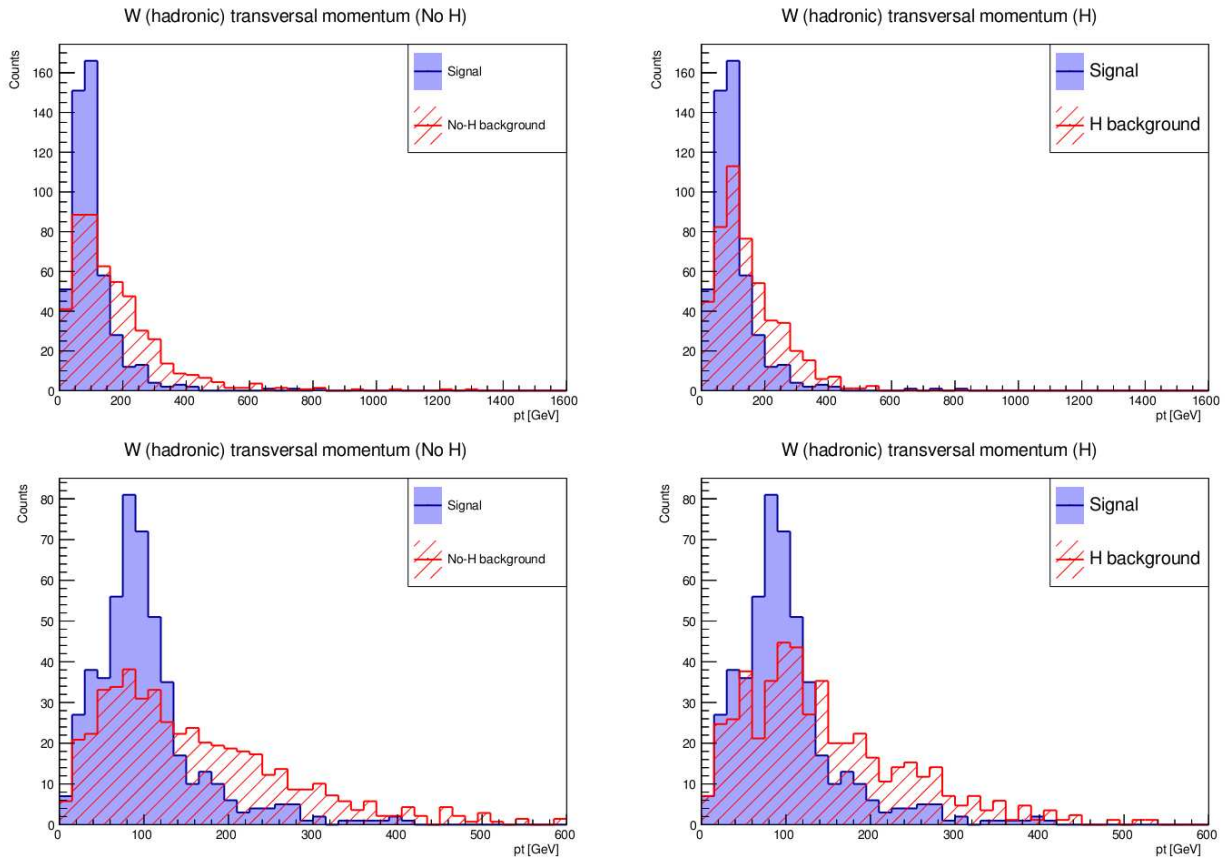

Figure 7.7: Transversal momentum of W for signal (blue) and background (red). On top the full distribution for no-Higgs background (left) and Higgs background (right). On bottom the same distributions are zoomed around the region of W boson nominal mass The histograms are normalized to the same area.

namely $0.7 \leq \theta \leq 2.2$ *rad* where the signal is greater than the background. The muon presents a completely different behaviour among signal and background. The signal distribution is almost uniform with a slightly abundance close to 10° and 170°. In both backgrounds, instead, presents very few counts in the central region. Especially the no-Higgs distribution, where the muon comes directly from the process and not from a jet, two peak are visible at 10° and 170°, while in the central region the counts drop.

Another set of observables studied was given by the acollinearity between two particles:

$$A_{1,2} = \pi - cos^{-1} \frac{(\overrightarrow{p}_1 \cdot \overrightarrow{p}_2)}{|\overrightarrow{p}_1| \cdot |\overrightarrow{p}_2|} \tag{7.13}$$

In particular it has been computed for three pair of particles: μ-W, μ-*pseudo* H and *pseudo* H-W, reported respectively in figure 7.17, 7.16 and 7.18. These observables are very important for the discrimination. The right plot of figure 7.16 shows a completely different distribution between signal and Higgs background and so does figure 7.17 as one can expect from the considerations done above on the muon in this background. Figure 7.17 is particularly significant also for the no-Higgs background, where almost half on the events lays on the very last region of the plot.

The last observable considered is the minimum separation between the muon and a jet. It is obtained by computing ΔR between the muon and each jet of the event that survives the quality cuts and the minimum among the ΔRs is stored. The distributions are reported in figure 7.19.

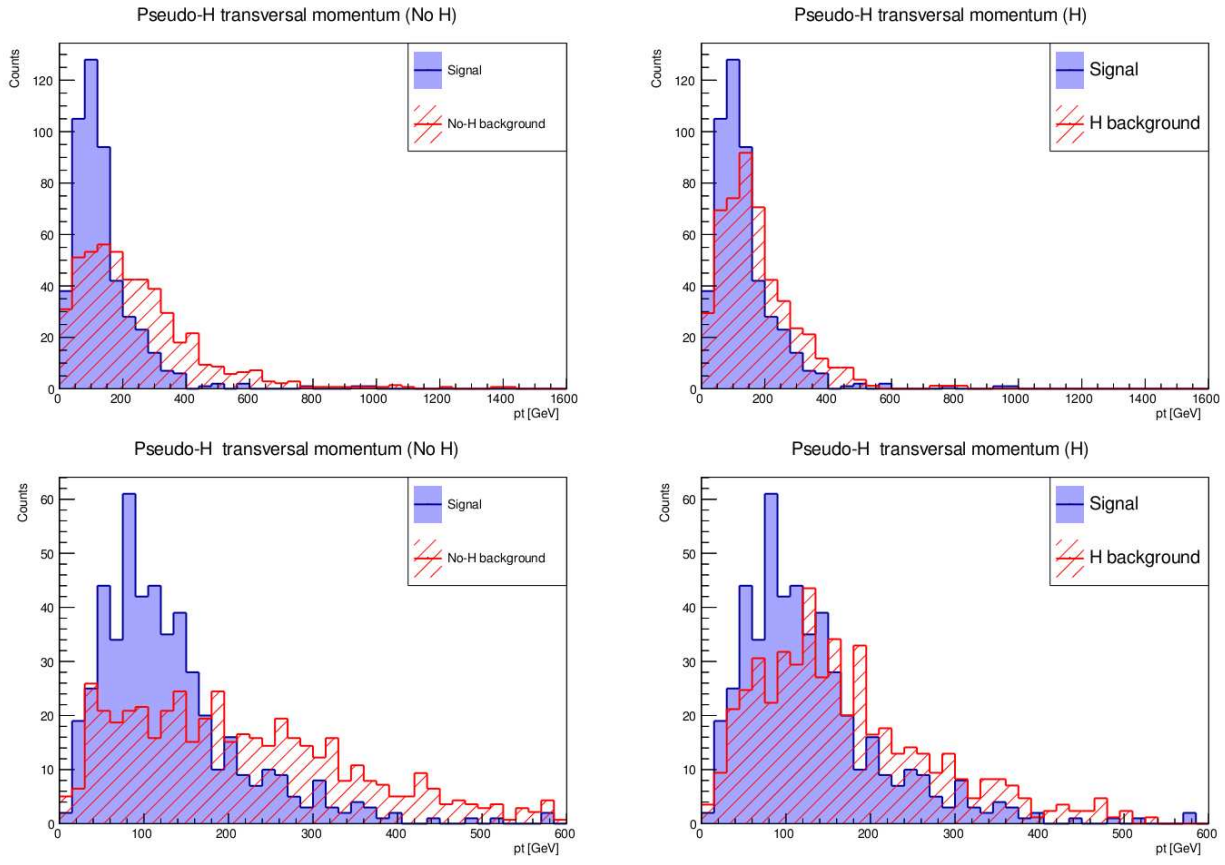

Figure 7.8: Transversal momentum of *pseudo H* for signal (blue) and background (red). On bottom the same distributions are zoomed around the region of W boson nominal mass The histograms are normalized to the same area

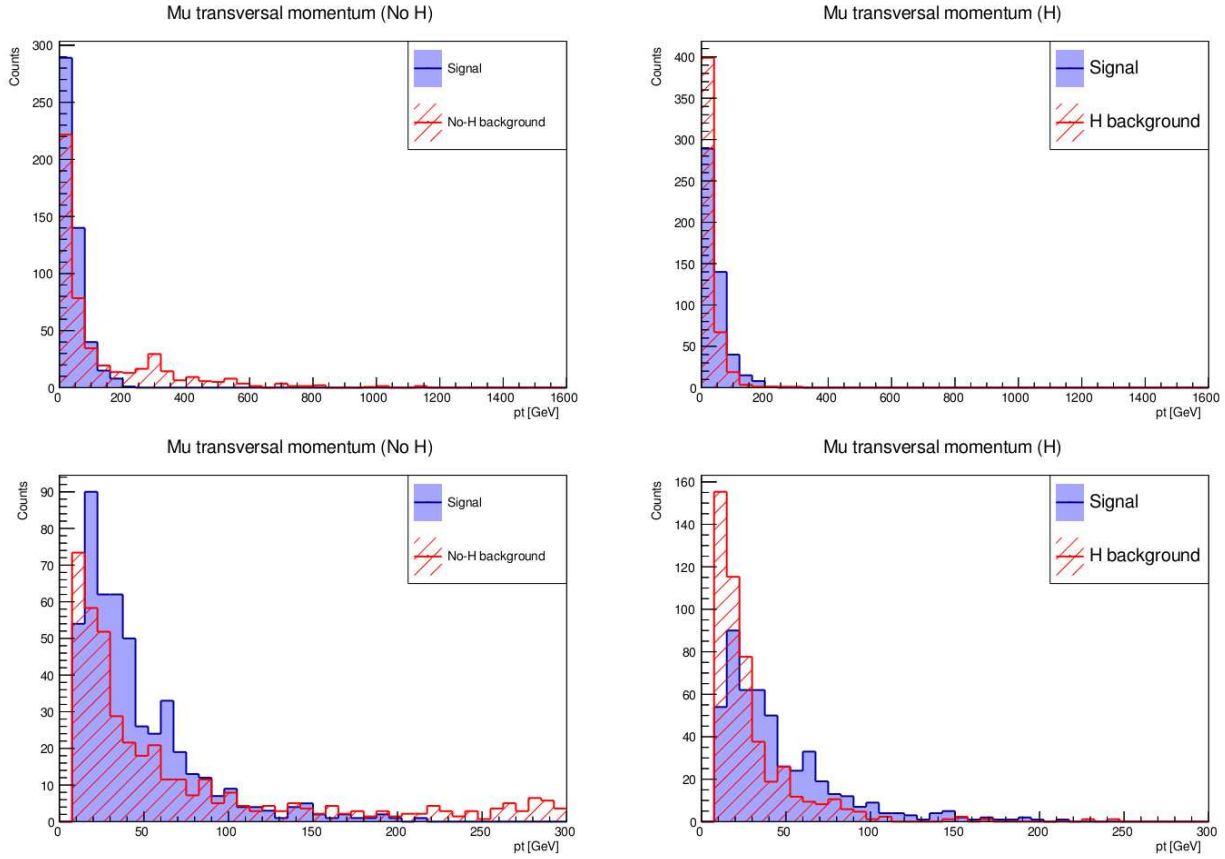

Figure 7.9: Transversal momentum of μ for signal (blue) and background (red). On bottom the same distributions are zoomed around the region of W boson nominal mass The histograms are normalized to the same area

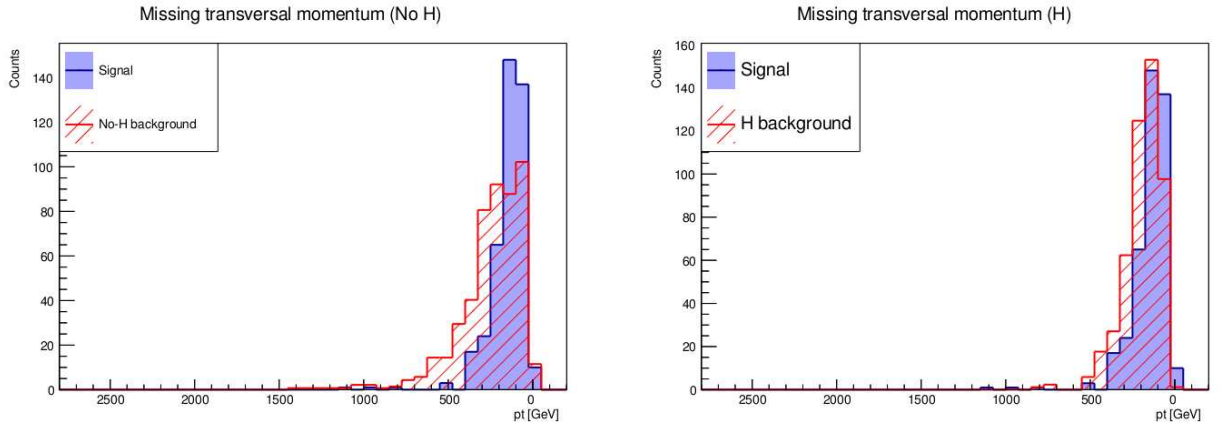

Figure 7.10: Missing transversal momentum of the events for signal (blue) and background (red). The histograms are normalized to the same area.

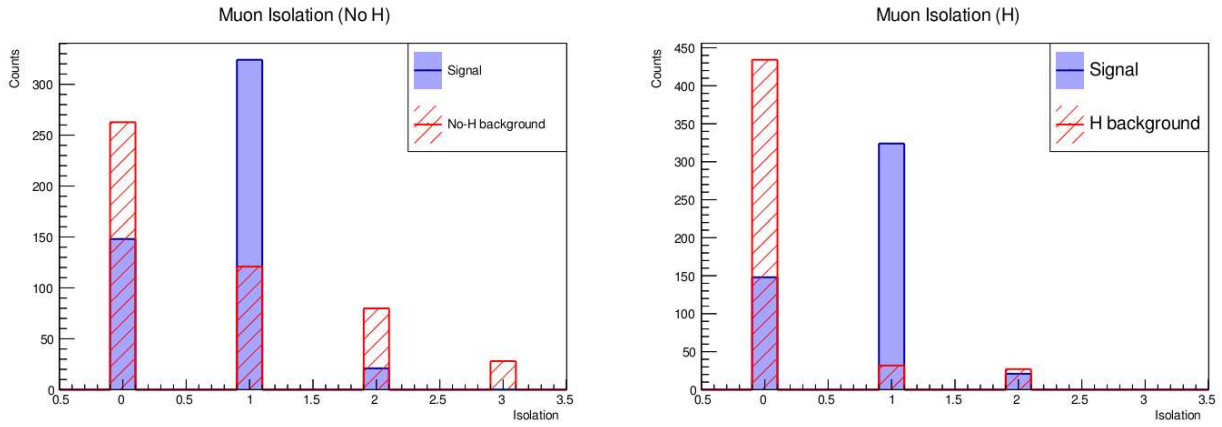

Figure 7.11: Number of isolated muons in the events for signal (blue) and background (red). The histograms are normalized to the same area.

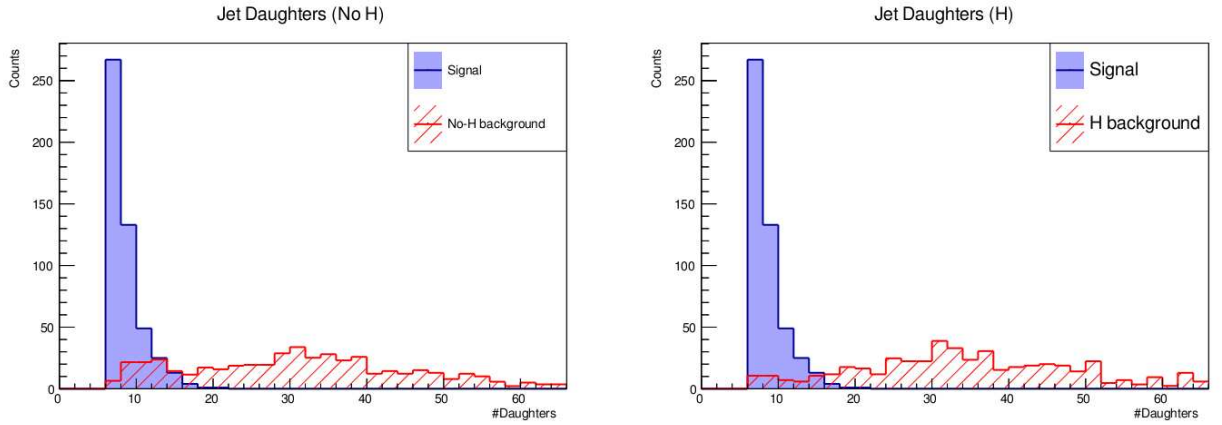

Figure 7.12: Total number of daughter particles in the jets selected for the W boson reconstruction for signal (blue) and background (red). The histograms are normalized to the same area

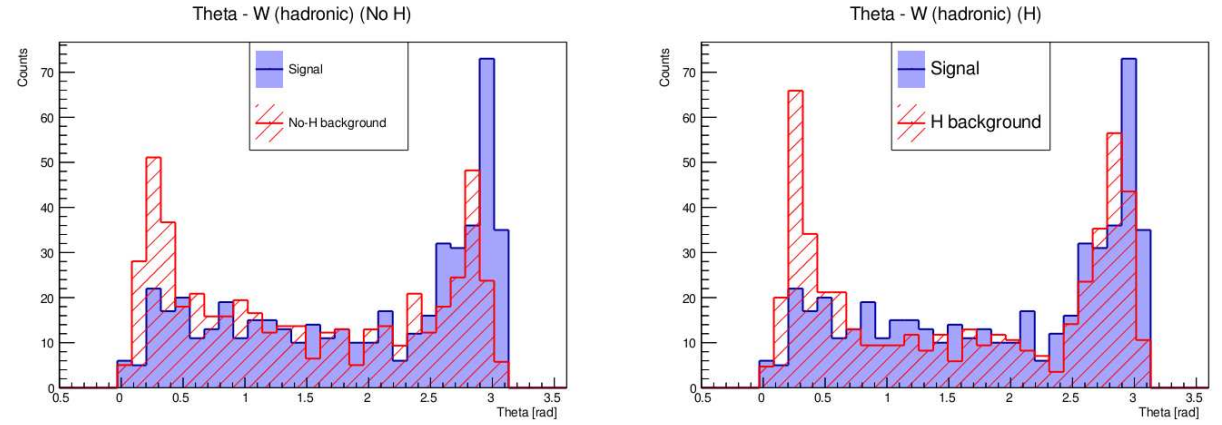

Figure 7.13: Polar angle with respect to the beam axis of W boson for signal (blue) and background (red). The histograms are normalized to the same area.

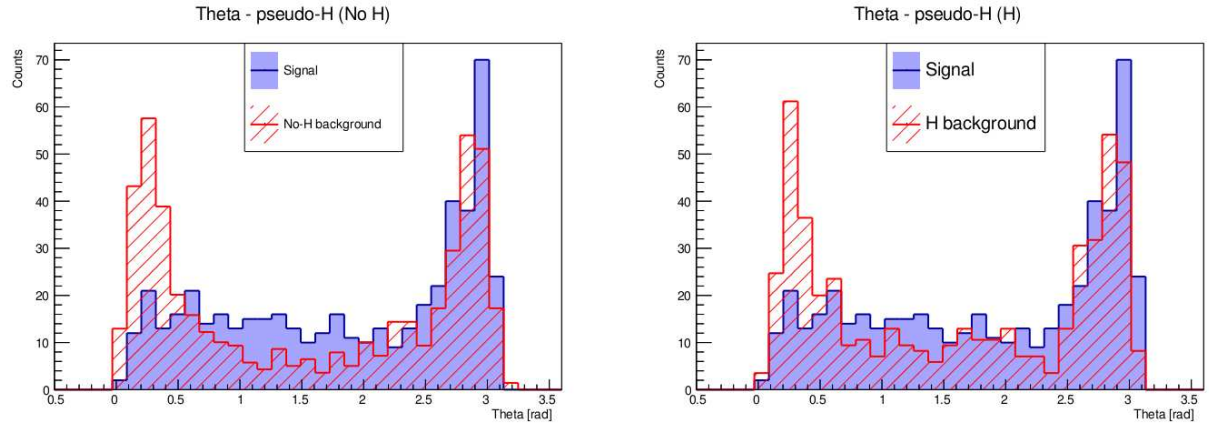

Figure 7.14: Polar angle with respect to the beam axis of *pseudo H* for signal (blue) and background (red). The histograms are normalized to the same area.

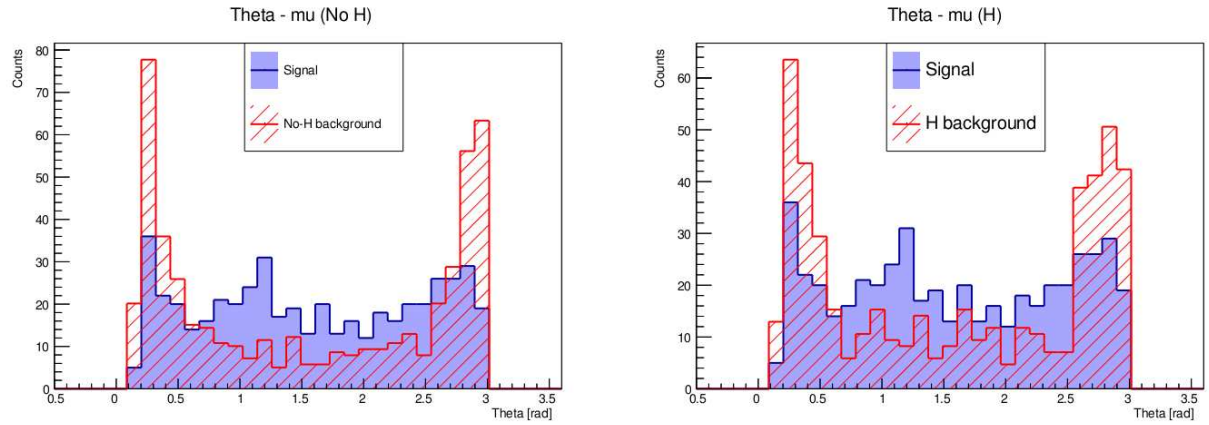

Figure 7.15: Polar angle with respect to the beam axis of μ for signal (blue) and background (red). The histograms are normalized to the same area.

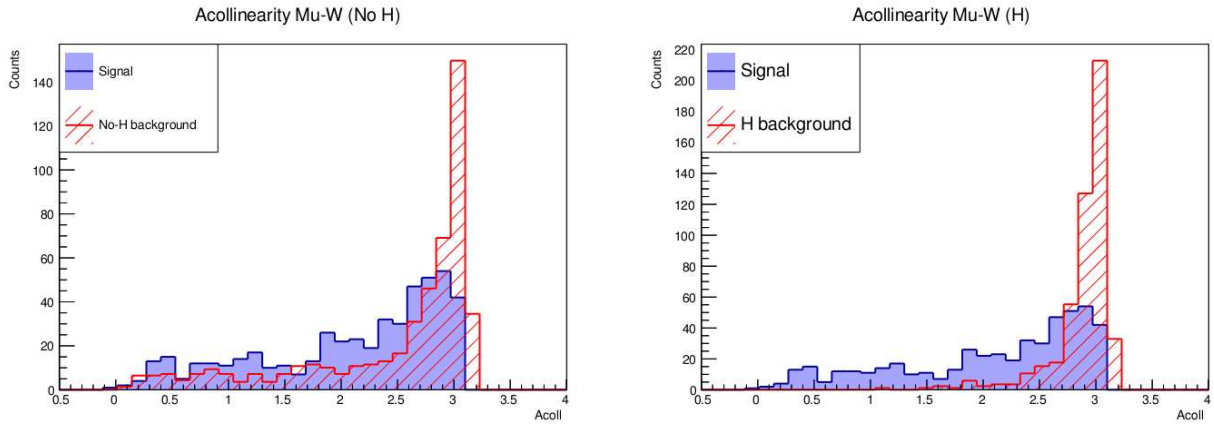

Figure 7.16: Acollinearity between μ and W for signal (blue) and background (red). The histograms are normalized to the same area.

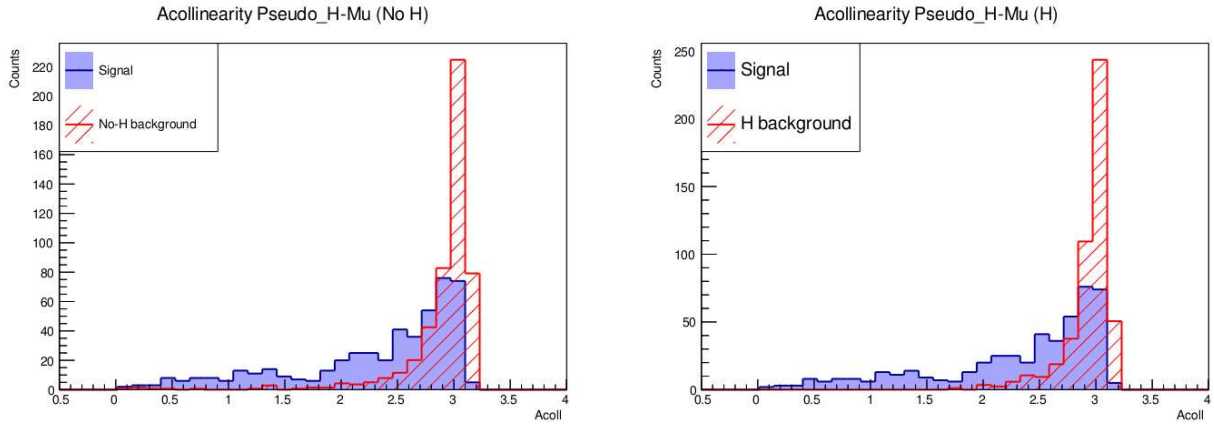

Figure 7.17: Acollinearity between μ and *pseudo H* for signal (blue) and background (red). The histograms are normalized to the same area.

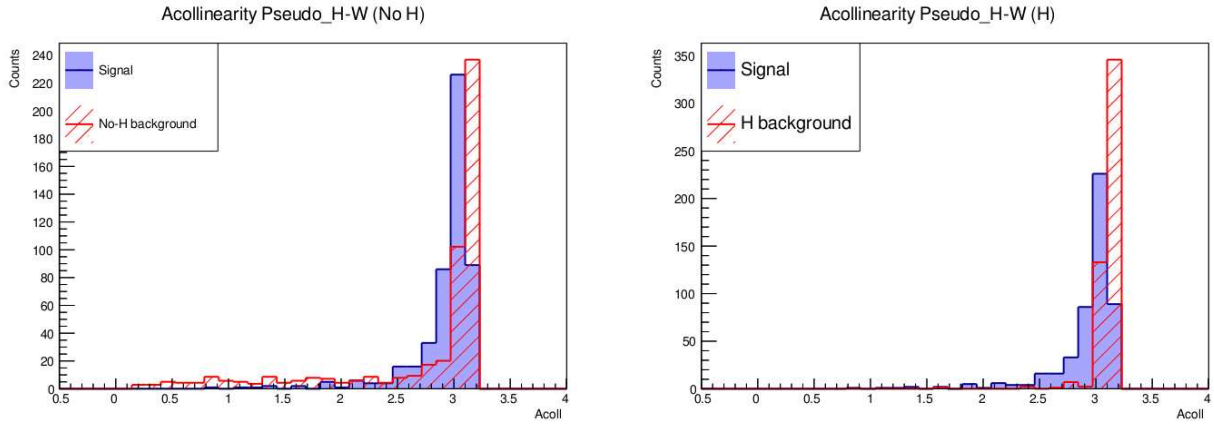

Figure 7.18: Acollinearity between W and *pseudo H* for signal (blue) and background (red). The histograms are normalized to the same area.

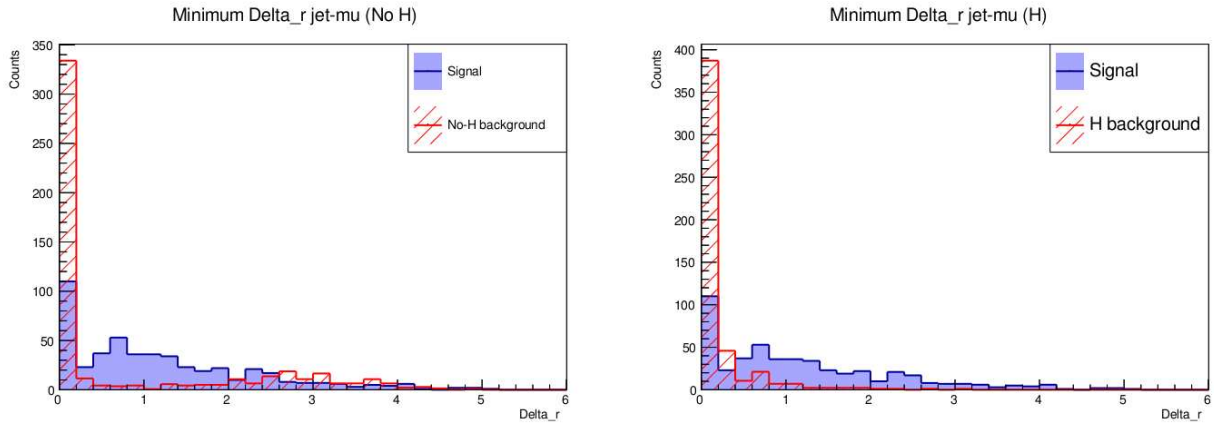

Figure 7.19: Minimum ΔR between the muon and jets for signal (blue) and background (red). The histograms are normalized to the same area.

Chapter 8

Multivariate analysis and $H \to WW$ cross section

In chapter 7 the observables useful to discriminate signal from background were presented. The actual classification is performed with a MultiVariate Analysis (MVA) approach, discussed in this chapter. For this purpose, the TMVA toolkit [79] integrated in the ROOT framework has been used.

TMVA provides several machine-learning algorithms with which perform a multivariate analysis, for example Boosted Decision Tree (BDT), MultiLayer Percepton (MLP), Multidimensional Likelihood estimator (PDERS), Functional Discriminant Analysis (FDA), Likelihood classifier.

The signal and background classification is achieved in two steps: train and test. The training of a machine-learning algorithm is obtained by giving to the algorithm a set of variables to consider and a set of events whose nature of signal or background is known. From the input variables the algorithm computes an output, which definition depends on the algorithm itself. Because of the fact that the algorithm knows the nature of the events, it can calculate the so-called "loss function" which measures how far an estimated value is from its true value. During the training process the algorithm tunes its parameters by minimizing the loss function in order to distinguish signal from background.

Once the algorithm has been trained, a test is performed by analyzing a different sample in order to assert the performance of the algorithm.

As mentioned above, TMVA offers several machine-learning algorithms and the first step of this analysis is to choose the one that maximize the background rejection (i.e. the fraction of background events excluded from the whole sample) and the signal efficiency (i.e. the fraction of signal events kept in the sample) simultaneously. In literature, one of the most used algorithm is the Boosted Decision Tree (BDT).

The plots in figure 8.1 reports the so-called Receiver Operating Characteristic (ROC) curve for a series of multivariate analysis methods. There, the background rejection is plotted as function of the signal efficiency. The plot on the left is obtained by training and testing the algorithms with the signal sample and the no-Higgs background, the one on the right with the signal and Higgs background samples. The plot shows clearly that the BDT is the algorithm with the best performances. A detailed discussion on the Boosted Decision Tree, focusing on its physics application can be found in [80].

8.1 Correlation and overtraining study

For the best discrimination, two different BDTs were trained, one with signal and no-Higgs sample, one with signal and Higgs background. At this point, the events considered are only the ones which survives at the pre-selection cuts and their number are reported in table 8.1. Half of the samples are used to train the BDTs, the other half to test it.

All the observables presented in the previous chapter are given as input to the algorithm and the linear-correlation among those has been studied, where the linear correlation between two observables i and j is defined as:

$$\rho_{i,j} = \frac{cov(i,j)}{\sigma_i \sigma_j} \tag{8.1}$$

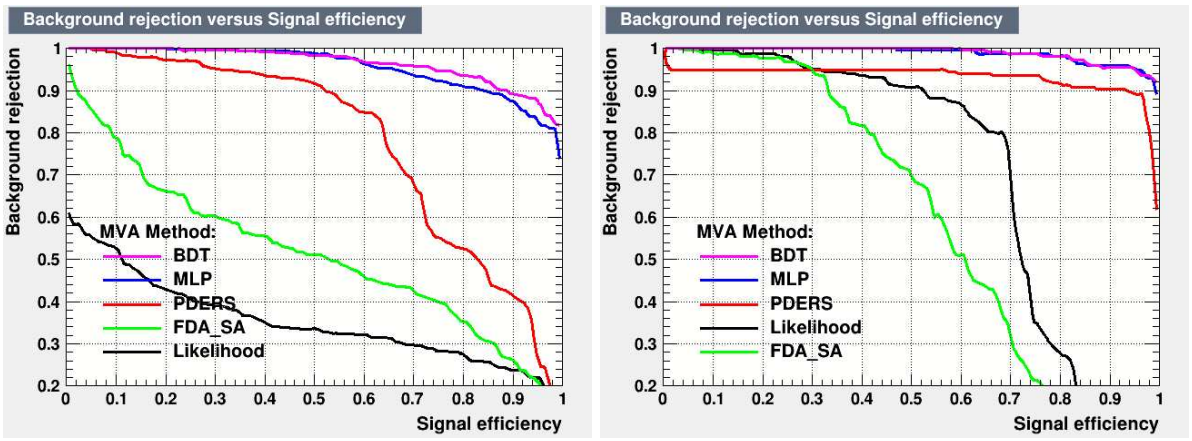

Figure 8.1: ROC curve for a set of MVA algorithms trained and tested on the signal and no-Higgs background samples (left) and on signal and Higgs background (right).

Sample	Events
Signal	493
no-H background	1176
H background	436

Table 8.1: Events used to train and test the BDTs.

with $cov(i, j)$ the covariance of the observables i and j and σ the standard deviation. Figure 8.2 and 8.3 shows respectively the correlation matrix of signal and both backgrounds. The parameter ρ lays in the range $[-100\%; +100\%]$, were -100% means that two variables are completely anti-correlated, while $+100\%$ indicates the complete correlation and 0% means the variables are totally uncorrelated. Looking at figure 8.2 the greatest correlations are between the transversal momentum and the invariant

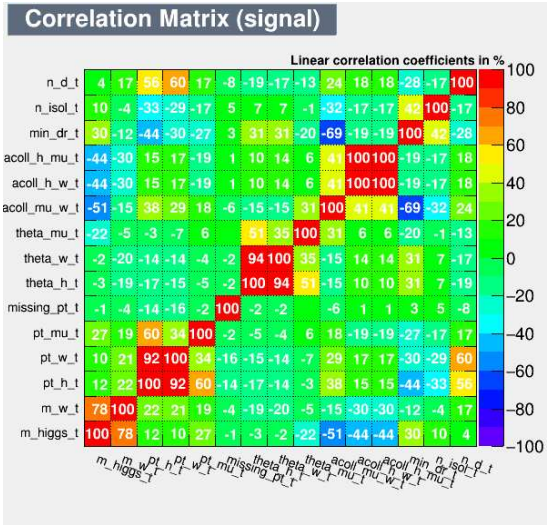

Figure 8.2: Linear correlation matrix of the signal sample

mass of the *pseudo H* and the W boson. This result is not surprising because the *pseudo H* is defined by the W boson and the muon, and the W boson is expected to be more energetic than the muon, therefore its contribution to the *pseudo H* will be more relevant. The correlation between the minimum ΔR and the acollinearity between the W boson and muon is predictable as well. The minimum ΔR is computed using the polar angle between the muon and one of the jets of the W boson while the acollinearity is computed using the polar angle between the muon and the W boson. It is interesting, instead, to notice the anti-correlation between the acollinearities and the mass of the *pseudo H*.

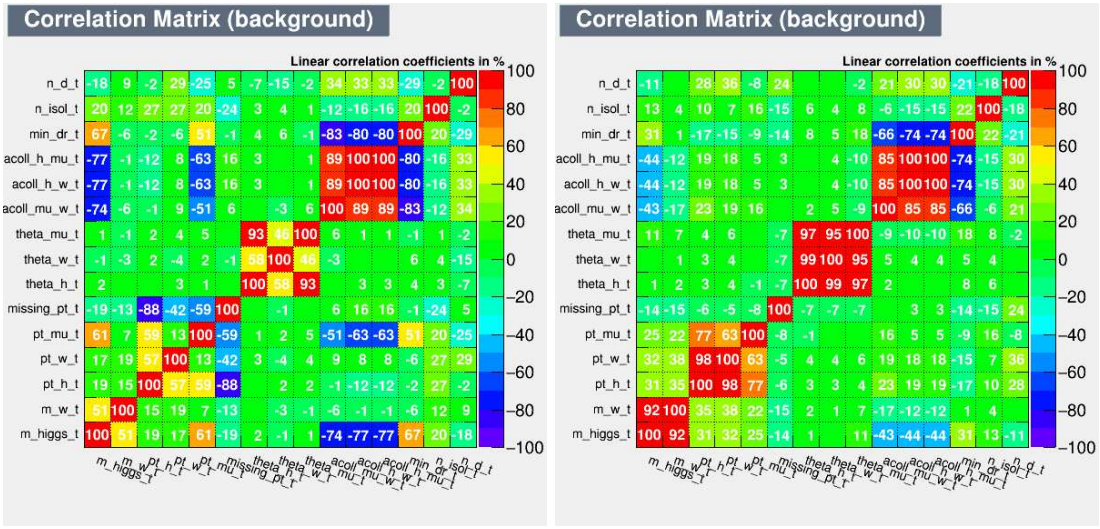

Figure 8.3: Linear correlation matrix of the no-Higgs background (left) and Higgs background (right) samples

Figure 8.3 shows the behaviour of the background samples. The major correlations, looking at the no-Higgs background, are for the kinematic variables of *pseudo H* and the W boson, meaning that the W boson contribution to the *pseudo H* is more relevant in the background with respect to the signal. Another difference is that the minimum ΔR is anti-correlated not only with the acollinearity W boson-muon, but also with the other acollinearities computed. Last, the polar angle of the muon appears very correlated to the polar angle of the *pseudo H*.

Looking at the right matrix, therefore at Higgs background, it can be seen immediately that the *pseudo H* and the W boson are extremely correlated, meaning that the muon contribution to the *pseudo H* is minimum with respect to the W boson. In this case, also all three polar angles considered appear highly correlated as well as the muon momentum and the missing one. An interesting fact is that the acollinearity between *pseudo H*-muon and *pseudo H*-W boson, are 100 % correlated, because both the muon and the W boson are produced from the same resonance, therefore their direction are correlated.

The second study performed on the BDTs concerned the overtraining. Overtraining may occur during the training of a machine-learning algorithm when the are too many input variables and too few training events. In this case, the algorithm may fit statistical fluctuations in the training sample [79], worsening the performance of the algorithm with an independent sample.

To understand if overtraining occurred, it is necessary to compare the BDT output distributions for training and test, if the distributions are compatible within the statistical uncertainties, no overtraining occurred. Figure 8.4 reports the comparisons for both no-Higgs (on the left) and Higgs (on the right) backgrounds.

The left plot shows slightly different distributions between training and test for the signal, caused by the low statistics used in the training process. The BDTs trained on the Higgs background, instead, does not present evidences of overtraining, despite the statistics is even lower than the no-Higgs case. The reason of this behaviour is that signal and Higgs background are topologically more different than signal and no-Higgs background, therefore the training of the BDT is easier in the Higgs background case and requires lower statistics.

8.2 Precision on the measurement of the cross section

Once the BDTs are trained, the actual discrimination can be performed. Given the fact that signal and backgrounds are well separated, as it can be seen in figure 8.4, the chosen approach is to select events by cutting on the BDT output. This means that for each event the response function of each BDT is evaluated. If both responses are above the correspondent threshold the event is kept, otherwise it is discarded.

After the analysis with the BDTs it is possible to evaluate the expected number of events and,

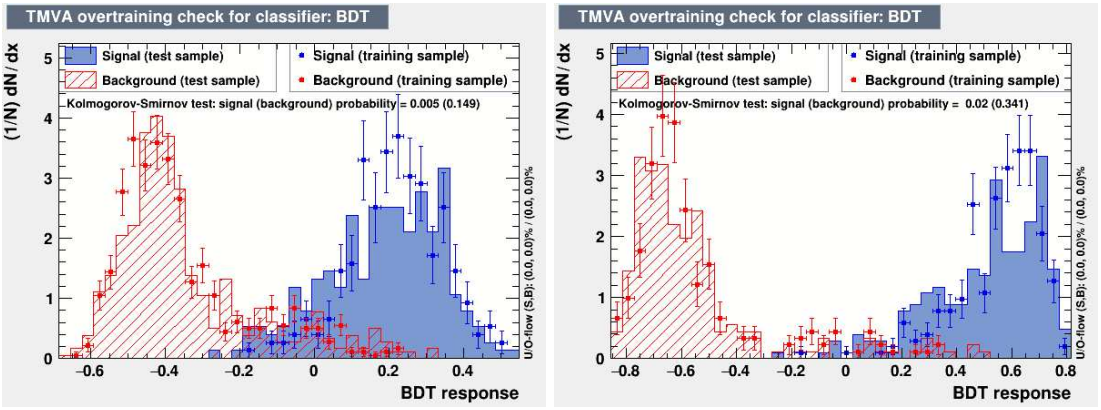

Figure 8.4: Overtraining check for the BDTs trained on signal and no-Higgs background (left) and Higgs background (right). The output distributions for test samples (filled histograms) have been superimposed the the output training distributions (dot).

therefore, to compute the precision on the measurement of the cross section, according to:

$$\frac{\Delta\sigma}{\sigma} = \frac{\sqrt{S+B}}{S} \tag{8.2}$$

where S is the number of expected count of the signal and B is the sum of the expected counts of the background.

The final result depends on the selected cuts on the BDTs. About 9000 combinations of the two thresholds have been tested and the one which gaves the best $\frac{\Delta\sigma}{\sigma}$ value has been adopted. The cuts are reported below:

- $BDT_{no\ Higgs}\ response\ > 0.22$;
- $BDT_{Higgs}\ response\ > 0.36$;

where the subscript refers to the sample used to train the BDT. The selection efficiency, the cross section and the expected number of events obtained in this configuration are reported in table 8.2.

The table enlightens the discrimination power of the combined BDTs. They are able to entirely remove every background but $\mu^+\mu^- \to WW\nu\overline{\nu} \to qq\mu\nu\nu\overline{\nu}$, whose efficiency drops to 0.06%.

Event	$\epsilon[\%]$	$\sigma\ [fb]$	Expected Events
$\mu^+\mu^- \to H\nu\overline{\nu} \to WW^*\nu\overline{\nu} \to qq\mu\nu\nu\overline{\nu}$	14.1 ± 0.8	17.3	2430 ± 150
$\mu^+\mu^- \to\to qq\mu\nu$	0.05 ± 0.03	$5.02 \cdot 10^3$	2600 ± 1300
$\mu^+\mu^- \to\to qqll$	< 0.01 $C.L. = 68\%$	$1.04 \cdot 10^3$	< 100 $C.L. = 68\%$
$\mu^+\mu^- \to\to qq\nu\nu$	< 0.01 $C.L. = 68\%$	$1.56 \cdot 10^3$	< 100 $C.L. = 68\%$
$\mu^+\mu^- \to H \to WW^* \to qqqq$	< 0.01 $C.L. = 68\%$	108	< 10 $C.L. = 68\%$
$\mu^+\mu^- \to H \to bb$	< 0.05 $C.L. = 68\%$	313	< 150 $C.L. = 68\%$
$\mu^+\mu^- \to H \to \tau\tau$	< 0.01 $C.L. = 68\%$	34.3	< 4 $C.L. = 68\%$

Table 8.2: Selection efficiency, cross section and expected events for signal and background events. The statistical error on the expected number of event has been obtained with a Bayesian approach as described in [77]

The statistical precision on the measurement of the cross section $\sigma(\mu^+\mu^- \to H\nu\overline{\nu} \to WW^*\nu\overline{\nu} \to qq\mu\nu\nu\overline{\nu})$ is:

$$\frac{\Delta\sigma}{\sigma} = 2.9\%$$

This result is obtained considering the expected number of event reported in table 8.2 for the signal and the $\mu^+\mu^- \to qq\mu\nu$ background. The other backgrounds are considered negligible since 0 events in the samples survived to the BDTs cuts.

With a conservative approach, considering the upper limit on the expected number of events for the other backgrounds, the result becomes:

$$\frac{\Delta\sigma}{\sigma} = 3.0\%$$

Chapter 9

Conclusions

The work presented in this thesis provides an evaluation of the precision on the measurement of the cross section of $\mu^+\mu^- \to H + X \to WW^* \to qq\mu\nu + X$ at the Muon Collider with a $\sqrt{s} = 3\ TeV$, assuming an integrated luminosity of $\mathcal{L} = 1\ ab^{-1}$.

A multivariate analysis approach has been implemented in order to discriminate signal from physics background. Pre-selection requirements were imposed to obtain a first discrimination and to mitigate the Beam-Induced Background effects on the reconstruction capabilities. Using the selected events as input, multivariate classifiers based on a boosted decision tree have been trained and applied to further improve the signal/background separation.

The result is:

$$\frac{\Delta\sigma(H \to WW^* \to \mu\nu qq)}{\sigma(H \to WW^* \to \mu\nu qq)} = 2.9\%$$

The precision obtained in this thesis can be compared with the one published by 3-TeV CLIC, the only e^+e^- collider that can reach the same energy in the center of mass. .

In order to do so, this result has been re-normalized to the same integrated luminosity expected by CLIC, namely, $\mathcal{L} = 2\ ab^{-1}$, obtaining:

$$\frac{\Delta\sigma(\mu^+\mu^- \to H + X \to WW^* \to qq\mu\nu)}{\sigma(\mu^+\mu^- \to H + X \to WW^* \to qq\mu\nu)} = 2.1\%$$

The result quoted by CLIC in [81] is:

$$\frac{\Delta\sigma(H \to WW^*)}{\sigma(H \to WW^*)} = 1.5\%$$

It has to be noticed that CLIC considered all the W decays, differently from this thesis. However, CLIC considered only the WW-fusion Higgs boson production mechanism, because they can separate the events coming from ZZ-fusion [82]. At the moment this is not possible at the muon collider, due to the presence of the nozzles that reduces the acceptance by excluding the region at low angles with respect to the beams.

The Muon Collider results are very similar to CLIC. This is encouraging, considering the fact that the Beam Induced Background is particularly intense in the Muon Collider.

Moreover, $s = 3\ TeV$ is the maximum c.o.m. energy at which CLIC would operated, while the Muon Collider is supposed to reach energy of tens of TeV at which a large increment of the sensitivity is expected, together with a minor impact of the BIB on the detector performances.

Another important fact to consider is that several developments on the algorithms are under study and they could improve the results obtained in this thesis. One example is the muon identification. So far, as mentioned in section 6.5.3, the muon identification is performed by asking that a track has hits in the muon system. This approach is very simple and is not optimized, and a particle coming from hadron decay in jets or particles from the BIB can be mis-identified as muon. A dedicated muon identification algorithm is currently under study.

Similar considerations can be done for the jet reconstruction which is not optimized. New reconstruction algorithms are currently under development and the goal is to improve the jet reconstruction efficiency at low momentum.

In addition, a better treatment of the fake jets caused by the BIB can be implemented using a multivariate analysis to separate them from jets generated by physics processes.

Finally, developments on the detector and the reconstruction algorithms are currently under study. In particular, studies on Machine-Detector Interface and detector technologies are in progress to reduce the BIB impact and the nozzles angle, that will allow to increment the detector acceptance.

This work is the first step of an analysis whose ultimate purpose is to evaluate the precision on the measurement on the coupling constant g_{HWW} at the Muon Collider. The cross section and the coupling constant are related by:

$$\sigma(H \to WW^*) \propto \frac{g^2_{HWW} \cdot g^2_{HWW} + g^2_{HZZ} \cdot g^2_{HWW}}{\Gamma_H} \tag{9.1}$$

The first g^2_{HWW} and g^2_{HZZ} are the coupling constants on the production mechanisms of the Higgs Boson, namely WW-fusion and ZZ-fusion, while other g^2_{HWW} contributions are due to the decay $H \to WW^*$.

To determine the precision on the measurement on g_{HWW} the result obtained in this thesis has to be combined with the precision on the measurement of the Higgs boson width Γ_H and on the coupling constant g^2_{HZZ}, which are under study.

Appendix A

WW and ZZ fusion comparison

In this chapter the observables presented in chapter 7 are plotted for the signal sample where the Higgs boson is produced via WW-fusion (blue) and for the signal sample where the Higgs boson is produced via ZZ-fusion (red). The histograms are normalized to the area of the WW-fusion sample.

Each observable shows compatible distributions for the two samples.

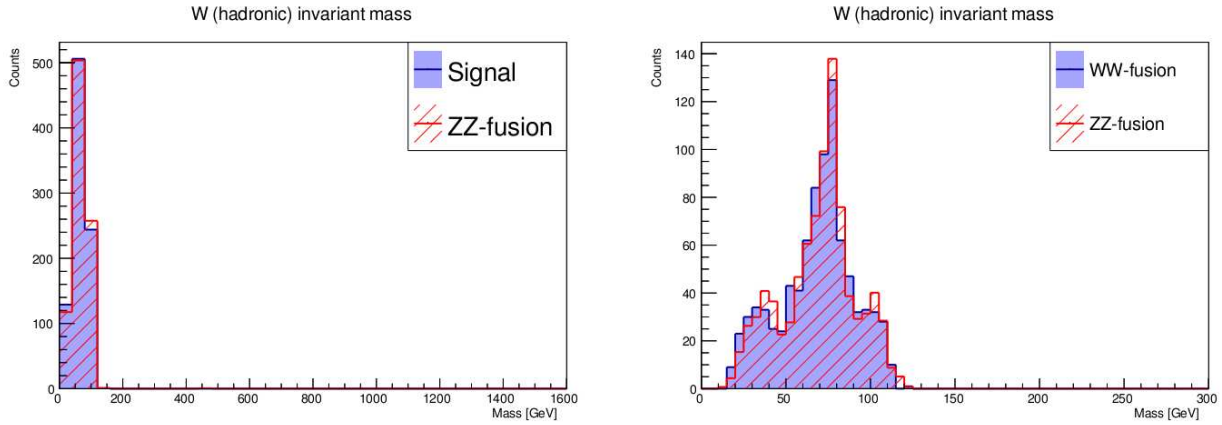

Figure A.1: Invariant mass of W for WW-fusion sample (blue) and ZZ-fusion sample (red). On left the full distribution, on the right the zoom around the region of W boson nominal mass. The histograms are normalized to the same area.

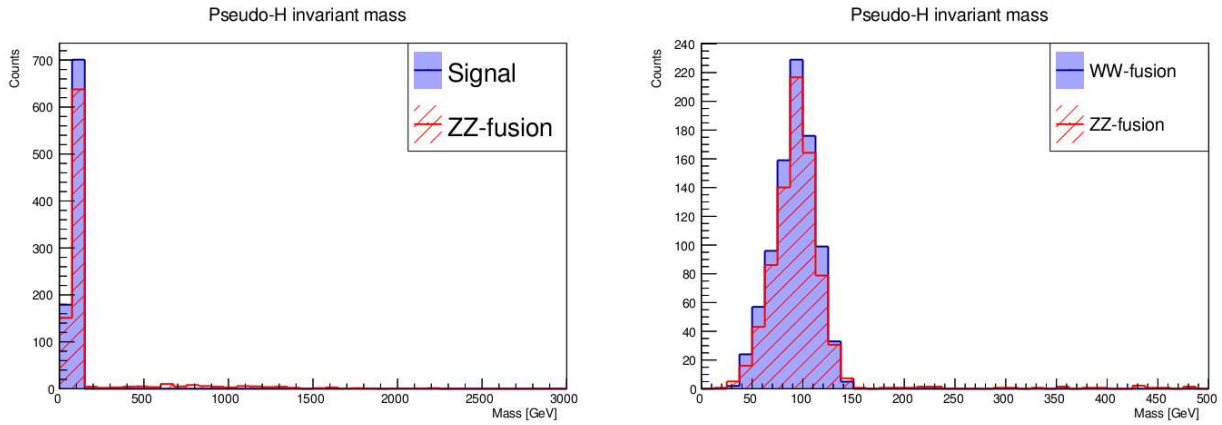

Figure A.2: Invariant mass of *pseudo H* for WW-fusion sample (blue) and ZZ-fusion sample (red). On left the full distribution, on the right the zoom around the region of Higgs boson nominal mass. The histograms are normalized to the same area.

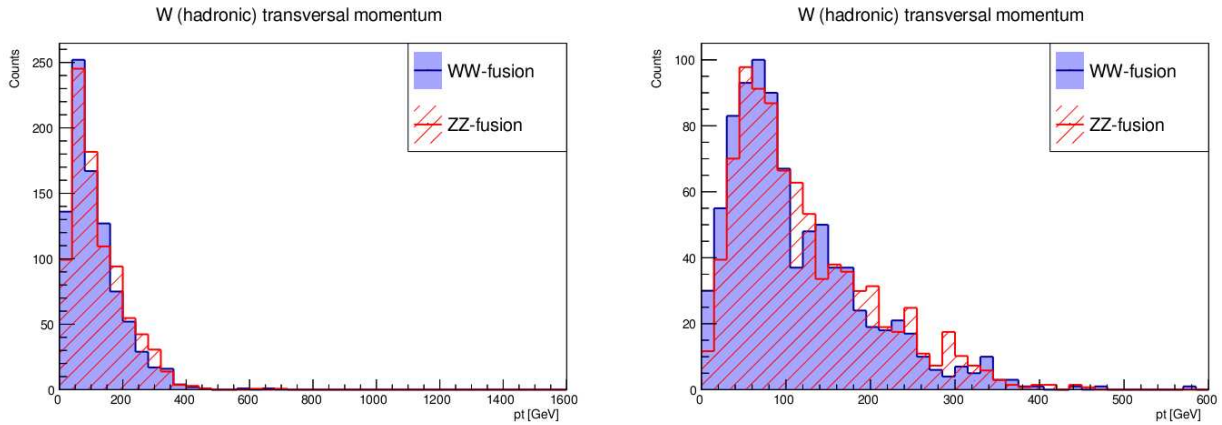

Figure A.3: Transversal momentum of W for WW-fusion sample (blue) and ZZ-fusion sample (red). On left the full distribution, on the right the zoom on the region of low pt. The histograms are normalized to the same area.

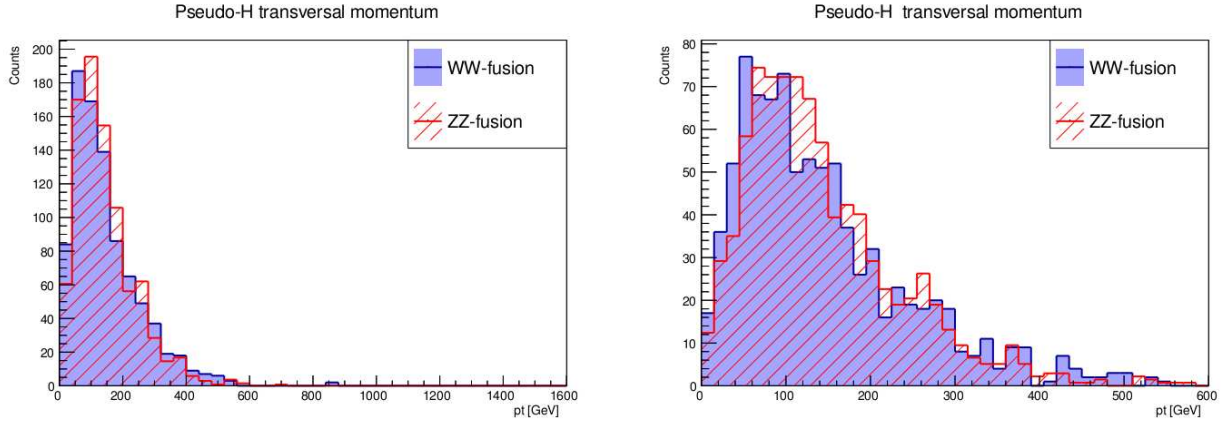

Figure A.4: Transversal momentum of *pseudo H* for WW-fusion sample (blue) and ZZ-fusion sample (red). On left the full distribution, on the right the zoom on the right the zoom on the region of low pt. The histograms are normalized to the same area.

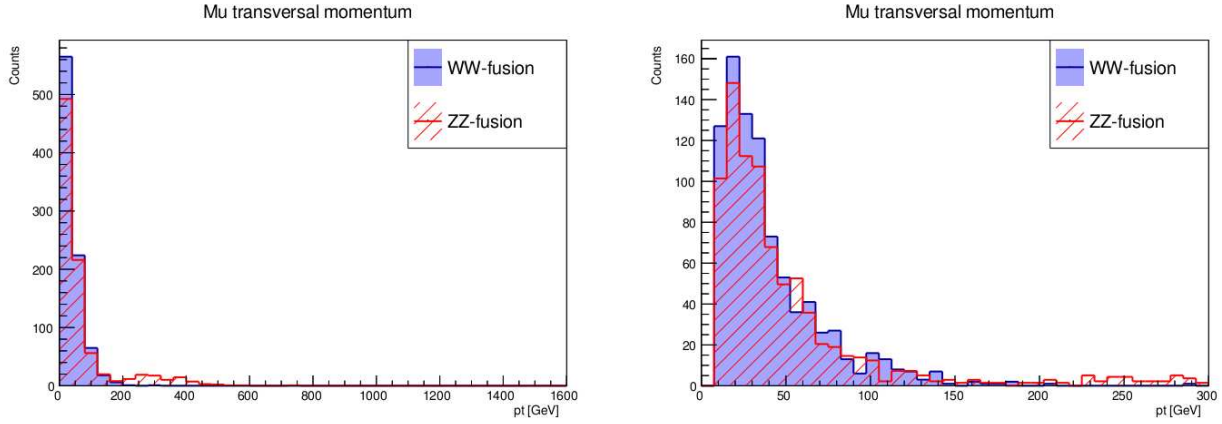

Figure A.5: Transversal momentum of μ for WW-fusion sample (blue) and ZZ-fusion sample (red). On left the full distribution, on the right the zoom on the right the zoom on the region of low pt. The histograms are normalized to the same area.

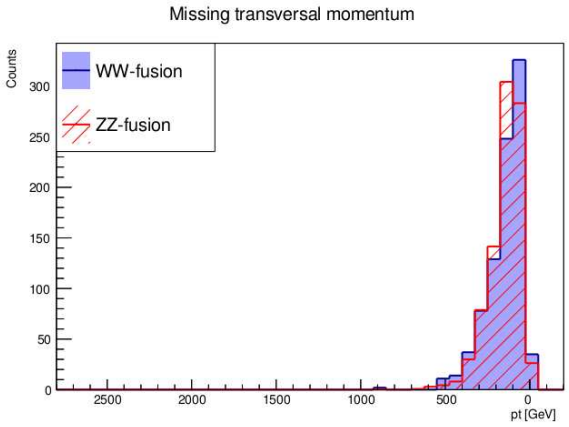

Figure A.6: Missing transversal momentum of the events for WW-fusion sample (blue) and ZZ-fusion sample (red). The histograms are normalized to the same area.

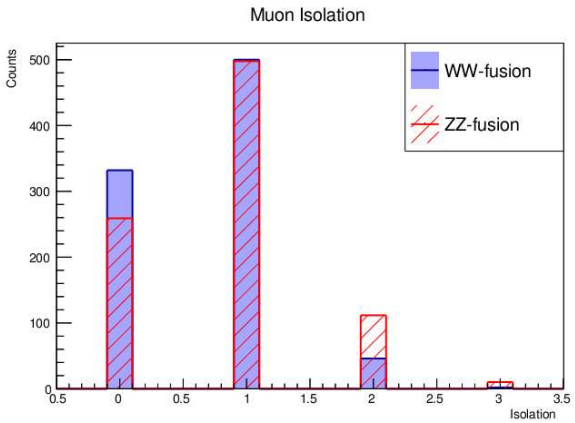

Figure A.7: Number of isolated muons in the events for for WW-fusion sample (blue) and ZZ-fusion sample (red). The histograms are normalized to the same area.

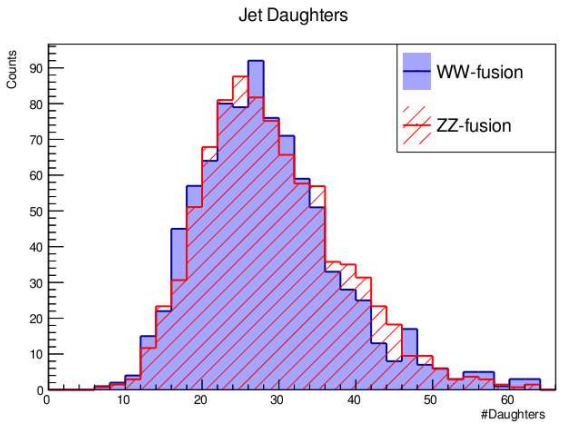

Figure A.8: Total number of daughter particles in the jets selected for the W boson reconstruction for for WW-fusion sample (blue) and ZZ-fusion sample (red). The histograms are normalized to the same area.

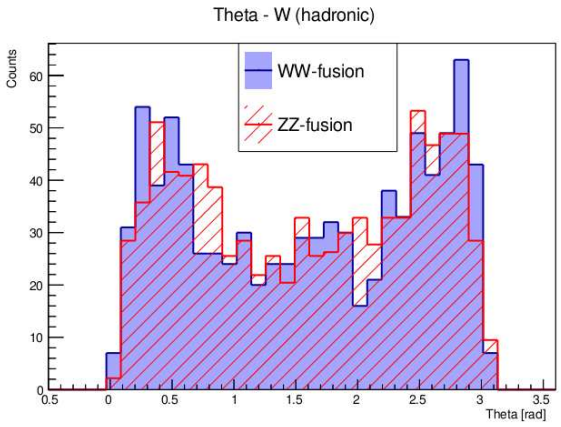

Figure A.9: Polar angle of W boson for WW-fusion sample (blue) and ZZ-fusion sample (red). The histograms are normalized to the same area.

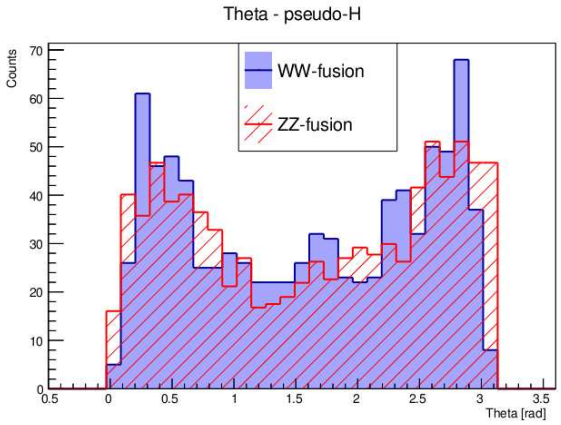

Figure A.10: Polar angle of *pseudo H* for WW-fusion sample (blue) and ZZ-fusion sample (red). The histograms are normalized to the same area.

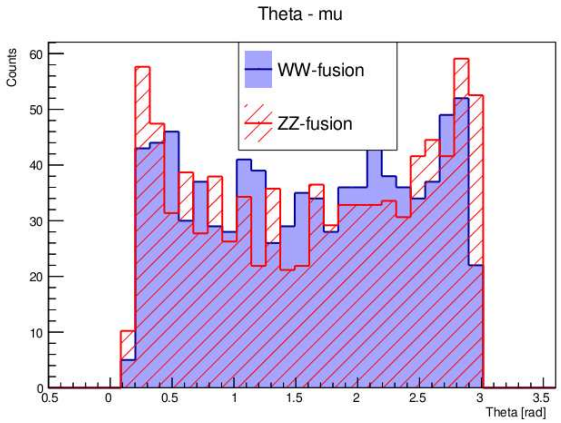

Figure A.11: Polar angle of μ for for WW-fusion sample (blue) and ZZ-fusion sample (red). The histograms are normalized to the same area.

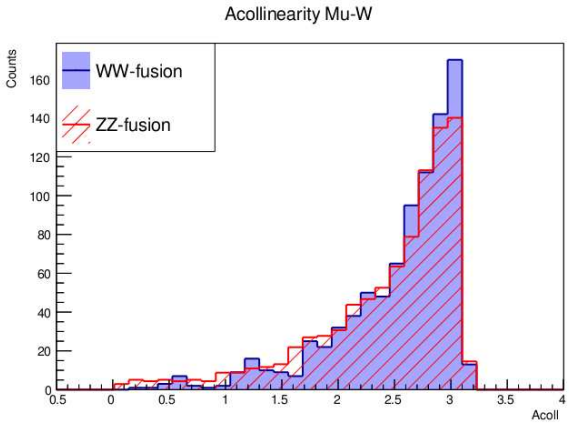

Figure A.12: Acollinearity between μ and W for WW-fusion sample (blue) and ZZ-fusion sample (red). The histograms are normalized to the same area.

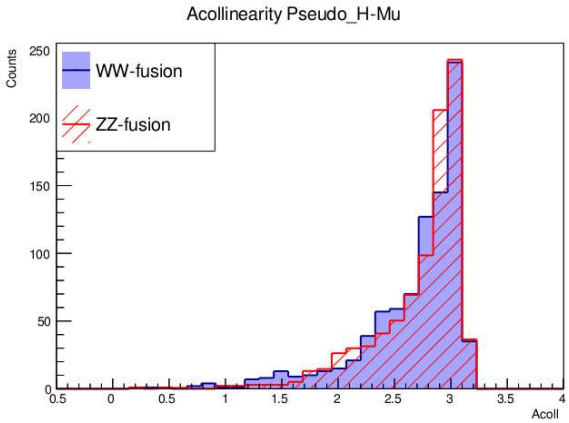

Figure A.13: Acollinearity between μ and *pseudo H* for WW-fusion sample (blue) and ZZ-fusion sample (red). The histograms are normalized to the same area..

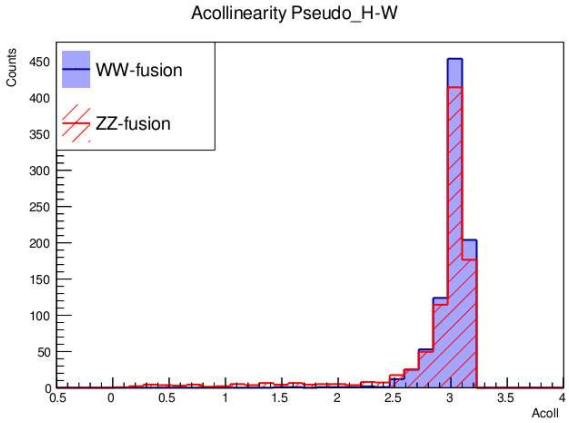

Figure A.14: Acollinearity between W and *pseudo H* for WW-fusion sample (blue) and ZZ-fusion sample (red). The histograms are normalized to the same area.

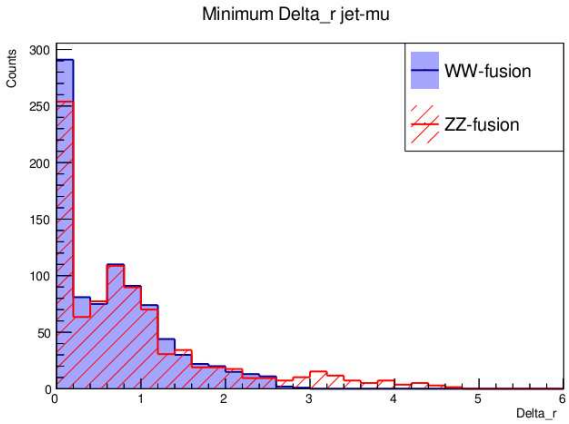

Figure A.15: Minimum ΔR between the muon and jets for WW-fusion sample (blue) and ZZ-fusion sample (red). The histograms are normalized to the same area.

Thanks

First of all I would like to thank my parents, Marco and Donatella, who swiped the card for five and half years, and, together with my sister Chiara, endured through my freaks out before almost every exam. Thank also to my grandpa Carlo, who taught me that math is important for a physicist. He obviously did not study “Analisi 3”.

Thanks to my grandma Anna Maria, my aunties Rina and Marcella, because their prayers are the only reason why I passed “theoretical” exam.

Beside my family, lots of people walked by my side in this dark and long journey, my colleagues Matteo and Federica, who supported my freaks out during labs, Daniele who was my partner during ”Briscola” matches, Riccardo called BBBolzo who shared with me anxiety issues, Veronica and her perfectly written notes and the all the other members of the “Pescul” group.

Thanks to Andrea, president of “La Festa di Fisica” and my guide along this journey.

Thanks also to Rodrigo, Matteo and Tommaso who bullied me since high school and I hope they will never stop.

Thanks to the “FEC”, world leaders in “popi popi”. Thanks to Giorgio and Loris, happy birthday Fecchio.

Thanks to Lin and his Campari.

Thanks to the one who was always there: prof. Mantovani.

Last, thanks to the ones I wish they were here, my grandpa Nino and my grandma Laura.

Bibliography

[1] Guido Altarelli and James Wells. "Gauge Theories and the Standard Model". In: *Collider Physics within the Standard Model: A Primer*. Ed. by James Wells. Cham: Springer International Publishing, 2017, pp. 1–25. DOI: 10.1007/978-3-319-51920-3_1. URL: https://doi.org/10.1007/978-3-319-51920-3_1.

[2] John Ellis. *Higgs Physics*. 2013. arXiv: 1312.5672 [hep-ph].

[3] Kien Nguyen. *The Higgs Mechanism*. 2009. URL: https://www.theorie.physik.uni-muenchen.de/lsfrey/teaching/archiv/sose_09/rng/higgs_mechanism.pdf.

[4] Heather E. Logan. *TASI 2013 lectures on Higgs physics within and beyond the Standard Model*. 2017. arXiv: 1406.1786 [hep-ph].

[5] J. de Blas et al. "Higgs Boson studies at future particle colliders". In: *Journal of High Energy Physics* 2020.1 (Jan. 2020). ISSN: 1029-8479. DOI: 10.1007/jhep01(2020)139. URL: http://dx.doi.org/10.1007/JHEP01(2020)139.

[6] Julien Baglio, Abdelhak Djouadi, and Jérémie Quevillon. "Prospects for Higgs physics at energies up to 100 TeV". In: *Reports on progress in physics. Physical Society (Great Britain)* 79 (Nov. 2015). DOI: 10.1088/0034-4885/79/11/116201.

[7] G. Aad et al. "Measurements of the Higgs boson production and decay rates and constraints on its couplings from a combined ATLAS and CMS analysis of the LHC pp collision data at s = 7

$$\sqrt{s} = 7$$

and 8 TeV". In: *Journal of High Energy Physics* 2016.8 (Aug. 2016). ISSN: 1029-8479. DOI: 10.1007/jhep08(2016)045. URL: http://dx.doi.org/10.1007/JHEP08(2016)045.

[8] European Strategy for Particle Physics Preparatory Group. *Physics Briefing Book*. 2020. arXiv: 1910.11775 [hep-ex].

[9] Michael Benedikt et al. "Future Circular Colliders succeeding the LHC". In: *Nature Physics* 16.4 (Apr. 2020), pp. 402–407. ISSN: 1745-2481. DOI: 10.1038/s41567-020-0856-2. URL: https://doi.org/10.1038/s41567-020-0856-2.

[10] CEPC collaboration. *CEPC Input to the European Particle Physics Strategy Update 2018-2020 - Physics and Detector*. URL: http://cepc.ihep.ac.cn/CEPC_Accelerator_Addendum/CEPC_Physics_Detector_MainText.pdf.

[11] Jonathan Bagger et al. Hiroaki Aihara. *The International Linear Collider. A Global Project*. 2019. arXiv: 1901.09829 [hep-ex].

[12] Jan Klamka. *The CLIC potential for new physics*. 2021. arXiv: 2111.04787 [hep-ex].

[13] Heather M. Gray. "Future colliders for the high-energy frontier". In: *Reviews in Physics* 6 (2021), p. 100053. ISSN: 2405-4283. DOI: https://doi.org/10.1016/j.revip.2021.100053. URL: https://www.sciencedirect.com/science/article/pii/S2405428321000022.

[14] Tessa Charles et al. "The Compact Linear Collider (CLIC) - 2018 Summary Report". In: (Jan. 2018).

[15] J-P. Delahaye et al. *Enabling Intensity and Energy Frontier Science with a Muon Accelerator Facility in the U.S.: A White Paper Submitted to the 2013 U.S. Community Summer Study of the Division of Particles and Fields of the American Physical Society*. 2014. arXiv: 1308.0494 [physics.acc-ph].

[16] U. Amaldi et al. *Charting the European Course to the High-Energy Frontier*. 2019. arXiv: 1912.13466 [hep-ex].

[17] N. Bartosik et al. "Detector and Physics Performance at a Muon Collider". In: *Journal of Instrumentation* 15.05 (May 2020), P05001–P05001. DOI: 10.1088/1748-0221/15/05/p05001. URL: https://doi.org/10.1088/1748-0221/15/05/p05001.

[18] J. de Blas et al. "Higgs Boson studies at future particle colliders". In: *Journal of High Energy Physics* 2020.1 (Jan. 2020). ISSN: 1029-8479. DOI: 10.1007/jhep01(2020)139. URL: http://dx.doi.org/10.1007/JHEP01(2020)139.

[19] Hind Al Ali et al. *The Muon Smasher's Guide*. 2021. arXiv: 2103.14043 [hep-ph].

[20] D. Buttazzo et al. *Letter of Interest: Muon Collider Physics Potential*. URL: https://indico.cern.ch/event/944012/contributions/3989516/attachments/2091456/3518021/Physics_SnowMass_LoI.pdf.

[21] J. C. Gallardo R. B. Palmer. *High energy colliders*. 2018. URL: https://arxiv.org/pdf/physics/9702016.pdf.

[22] Jean Pierre Delahaye et al. *Muon Colliders*. 2019. arXiv: 1901.06150 [physics.acc-ph].

[23] N.V. Mokhov and S.I. Striganov. "Detector Backgrounds at Muon Colliders". In: *Physics Procedia* 37 (2012). Proceedings of the 2nd International Conference on Technology and Instrumentation in Particle Physics (TIPP 2011), pp. 2015–2022. ISSN: 1875-3892. DOI: https://doi.org/10.1016/j.phpro.2012.03.761. URL: https://www.sciencedirect.com/science/article/pii/S187538921201927X.

[24] *Accelerator Physics of Colliders*. URL: https://pdg.lbl.gov/2017/reviews/rpp2017-rev-accel-phys-colliders.pdf.

[25] *Beta and emittance*. URL: https://www.lhc-closer.es/taking_a_closer_look_at_lhc/0.beta___emittance.

[26] Helmut Wiedemann. *Particle Accelerator Physics*. Springer Nature, 2015. ISBN: 9783319183176.

[27] Manuela Boscolo, Jean-Pierre Delahaye, and Mark Palmer. "The Future Prospects of Muon Colliders and Neutrino Factories". In: *Reviews of Accelerator Science and Technology* (Sept. 2019), pp. 189–214. DOI: 10.1142/9789811209604_0010. URL: http://dx.doi.org/10.1142/9789811209604_0010.

[28] D. Alesini et al. *Positron driven muon source for a muon collider*. 2019. arXiv: 1905.05747 [physics.acc-ph].

[29] M. A. Palmer. *The US muon accelerator program*. 2015. arXiv: 1502.03454 [physics.acc-ph].

[30] S. D. Holmes et al. *Status and Opportunities at Project X: A Multi-MW Facility for Intensity Frontier Research*. 2014. arXiv: 1409.5809 [physics.acc-ph].

[31] D. Neuffer and C. Yoshikawa. *Muon capture for the front end of a muon collider*. 2012. arXiv: 1202.5335 [physics.acc-ph].

[32] Daniel M. Kaplan. *Overview of muon cooling*. URL: https://inspirehep.net/files/203ff4641541d944658

[33] Rolland P. Johnson. *Ionization coolingr*. 2007. eprint: 1905.05747. URL: https://accelconf.web.cern.ch/cl07/papers/tum2i04.pdf.

[34] Alexander Wu Chao and Maury Tigner. *Handbook of Accelerator Physics and Engineering*. WORLD SCIENTIFIC, 1999. DOI: 10.1142/3818. eprint: https://www.worldscientific.com/doi/pdf/10.1142/3818. URL: https://www.worldscientific.com/doi/abs/10.1142/3818.

[35] Maurizio Bonesini. "Emittance exchange in MICE". In: *PoS* EPS-HEP2019 (2020), p. 025. DOI: 10.22323/1.364.0025.

[36] Yves R. Roblin et al. "Recirculating linear accelerators for future muon facilities". In: *AIP Conference Proceedings* 1423.1 (2012), pp. 425–430. DOI: 10.1063/1.3688840. eprint: https://aip.scitation.org/doi/pdf/10.1063/1.3688840. URL: https://aip.scitation.org/doi/abs/10.1063/1.3688840.

[37] D. J. SUMMERS. "MUON ACCELERATION USING FIXED FIELD, ALTERNATING GRADIENT (FFAG) RINGS". In: *International Journal of Modern Physics A* 20.16 (June 2005), pp. 3861–3864. ISSN: 1793-656X. DOI: 10.1142/s0217751x05027813. URL: http://dx.doi.org/10.1142/S0217751X05027813.

[38] J. Eldred, V. Lebedev, and A. Valishev. "Rapid-cycling synchrotron for multi-megawatt proton facility at Fermilab". In: *Journal of Instrumentation* 14.07 (July 2019), P07021–P07021. DOI: 10.1088/1748-0221/14/07/p07021. URL: https://doi.org/10.1088/1748-0221/14/07/p07021.

[39] A. V. Zlobin et al. *Storage Ring And Interaction Region Magnets For A $\mu^+\mu^-$ Higgs Factory*. 2014. arXiv: 1409.5461 [physics.acc-ph].

[40] A. V. Zlobin et al. *Magnet designs for muon collider ring and interactions regions*. 2012. arXiv: 1202.0270 [physics.acc-ph].

[41] Y. Alexahin and E. Gianfelice-Wendt. "A 3 TeV Muon Collider Lattice Design". In: (Jan. 2012).

[42] M-H Wang et al. "Design of a 6 TeV muon collider". In: *Journal of Instrumentation* 11 (Sept. 2016), P09003–P09003. DOI: 10.1088/1748-0221/11/09/P09003.

[43] J-P. Delahaye et al. *Enabling Intensity and Energy Frontier Science with a Muon Accelerator Facility in the U.S.: A White Paper Submitted to the 2013 U.S. Community Summer Study of the Division of Particles and Fields of the American Physical Society*. 2014. arXiv: 1308.0494 [physics.acc-ph].

[44] Francesco Collamati et al. *Advanced assessment of Beam Induced Background at a Muon Collider*. 2021. arXiv: 2105.09116 [physics.acc-ph].

[45] Dominik Arominski et al. *A detector for CLIC: main parameters and performance*. 2018. arXiv: 1812.07337 [physics.ins-det].

[46] Muon Collider collaboration. URL: https://confluence.infn.it/display/muoncollider/Tracking+detector.

[47] Laura Buonincontri. "Study of mitigation strategies of beam induced background and Higgs boson couplings measurements at a muon collider". 2020.

[48] Massimo Casarsa et al. "Detector Performance Studies at a Muon Collider". In: *PoS* ICHEP2020 (2021), p. 826. DOI: 10.22323/1.390.0826.

[49] Hannsjörg Weber. *Study on tracker occupancy for a Muon Collider Experiment*. URL: https://indico.fnal.gov/event/46571/contributions/202676/attachments/137580/171585/20201119_TrackerOccupancy.pdf.

[50] Artur Apresyan. *Tracker overview*. URL: https://indico.cern.ch/event/1037447/contributions/4379016/attachments/2256962/3829840/Trackers_Apresyan_MC.pdf.

[51] *Textual description of the geometry*. URL: https://github.com/MuonColliderSoft/detector-simulation/blob/master/geometries/MuColl_v1/text_description.md.

[52] Alessandro Montella. "Study of the Physics Potential of the $H \to \mu\mu$ Direct Decay Channel at a 3 TeV Muon Collider". 2021.

[53] C J Johnstone and N V Mokhov. "Optimization of a muon collider interaction region with respect to detector backgrounds and the heat load to the cryogenic systems". In: (Oct. 1996). URL: https://www.osti.gov/biblio/406119.

[54] N: Bartosik et al. P. Andreetto. *BIB mitigation at Muon Collider - 2021*. URL: https://indico.cern.ch/event/1028474/contributions/4318440/attachments/2225479/3774867/2021_04_07_bartosik_v1.pdf.

[55] Nikolai V. Mokhov and Sergei I. Striganov. "Simulation of backgrounds in detectors and energy deposition in superconducting magnets at $\mu^+\mu^-$ colliders". In: *AIP Conference Proceedings* 372.1 (1996), pp. 234–256. DOI: 10.1063/1.50907. eprint: https://aip.scitation.org/doi/pdf/10.1063/1.50907. URL: https://aip.scitation.org/doi/abs/10.1063/1.50907.

[56] V. Di Benedetto et al. "A study of muon collider background rejection criteria in silicon vertex and tracker detectors". In: *Journal of Instrumentation* 13.09 (Sept. 2018), P09004–P09004. ISSN: 1748-0221. DOI: 10.1088/1748-0221/13/09/p09004. URL: http://dx.doi.org/10.1088/1748-0221/13/09/P09004.

[57] Donatella Lucchesi. *Beam Induced Background Issues*. URL: https://indico.fnal.gov/event/48995/contributions/214443/attachments/143241/181133/MDI-Forum052021.pdf.

[58] N: Bartosik et al. P. Andreetto. *BIB mitigation at Muon Collider - 2020*. URL: https://indico.cern.ch/event/957299/contributions/4023405/attachments/2106163/3542069/2020_09_21_bartosik_v1.pdf.

[59] Torbjörn Sjöstrand, Stephen Mrenna, and Peter Skands. "A brief introduction to PYTHIA 8.1". In: *Computer Physics Communications* 178.11 (June 2008), pp. 852–867. ISSN: 0010-4655. DOI: 10.1016/j.cpc.2008.01.036. URL: http://dx.doi.org/10.1016/j.cpc.2008.01.036.

[60] Pascal Stienemeier et al. *WHIZARD 3.0: Status and News*. 2021. arXiv: 2104.11141 [hep-ph].

[61] Nicola Mori. "GGS: A Generic Geant4 Simulation package for small- and medium-sized particle detection experiments". In: *Nuclear Instruments and Methods in Physics Research Section A: Accelerators, Spectrometers, Detectors and Associated Equipment* 1002 (June 2021), p. 165298. ISSN: 0168-9002. DOI: 10.1016/j.nima.2021.165298. URL: http://dx.doi.org/10.1016/j.nima.2021.165298.

[62] M Frank et al. "DD4hep: A Detector Description Toolkit for High Energy Physics Experiments". In: *Journal of Physics: Conference Series* 513.2 (June 2014), p. 022010. DOI: 10.1088/1742-6596/513/2/022010. URL: https://doi.org/10.1088/1742-6596/513/2/022010.

[63] N. Bartosik. *Full detector simulation with unprecedented background occupancy at a Muon Collider*. URL: https://indico.cern.ch/event/948465/contributions/4323702/attachments/2246302/3809598/2021_05_17_bartosik_v1.pdf.

[64] Thomas Kramer. *Track Parameters in LCIO*. URL: http://flc.desy.de/lcnotes/notes/localfsExplorer_read?currentPath=/afs/desy.de/group/flc/lcnotes/LC-DET-2006-004.pdf.

[65] E. Brondolin et al. "Conformal tracking for all-silicon trackers at future electron–positron colliders". In: *Nuclear Instruments and Methods in Physics Research Section A: Accelerators, Spectrometers, Detectors and Associated Equipment* 956 (2020), p. 163304. ISSN: 0168-9002. DOI: https://doi.org/10.1016/j.nima.2019.163304. URL: https://www.sciencedirect.com/science/article/pii/S0168900219315517.

[66] M Hansroul, H Jeremie, and D Savard. "Fast circle fit with the conformal mapping method". In: *Nucl. Instrum. Methods Phys. Res., A* 270 (Nov. 1988), 498–501. 5 p. URL: http://cds.cern.ch/record/192472.

[67] A. Glazov et al. "Filtering tracks in discrete detectors using a cellular automaton". In: *Nuclear Instruments and Methods in Physics Research Section A: Accelerators, Spectrometers, Detectors and Associated Equipment* 329.1 (1993), pp. 262–268. ISSN: 0168-9002. DOI: https://doi.org/10.1016/0168-9002(93)90945-E. URL: https://www.sciencedirect.com/science/article/pii/016890029390945E.

[68] Greg Welch and Gary Bishop. *An Introduction to the Kalman Filter*. 1995.

[69] N. Bartosik. *Track-reconstruction considerations for the Muon Collider*. URL: https://agenda.infn.it/event/26135/contributions/132719/attachments/79910/104092/2021_03_10_bartosik.pdf.

[70] *Filter Double Layer Hits*. URL: https://github.com/MuonColliderSoft/MarlinTrkProcessors/tree/master/source/Utils.

[71] M.A. Thomson. "Particle flow calorimetry and the PandoraPFA algorithm". In: *Nuclear Instruments and Methods in Physics Research Section A: Accelerators, Spectrometers, Detectors and Associated Equipment* 611.1 (Nov. 2009), pp. 25–40. ISSN: 0168-9002. DOI: 10.1016/j.nima.2009.09.009. URL: http://dx.doi.org/10.1016/j.nima.2009.09.009.

[72] Trong Hieu TRAN. *Pandora PFA - a brief introduction Pandora PFA - a brief introduction*. URL: https://indico.in2p3.fr/event/7483/contributions/42227/attachments/33987/41889/PandoraPFA.pdf.

[73] Matteo Cacciari, Gavin P. Salam, and Gregory Soyez. "FastJet user manual". In: *The European Physical Journal C* 72.3 (Mar. 2012). ISSN: 1434-6052. DOI: 10.1140/epjc/s10052-012-1896-2. URL: http://dx.doi.org/10.1140/epjc/s10052-012-1896-2.

[74] E van der Kraaij and J Marshall. "Development of the PANDORAPFANEW muon reconstruction algorithm". In: (June 2011). URL: https://cds.cern.ch/record/1443539.

[75] C. Aimè et al. *Muon reconstruction performance and detector-design consideration for a Muon Collider*. URL: https://indico.desy.de/event/28202/contributions/105657/attachments/67677/84359/EPSHEP2021_IlariaVai_V2.pdf.

[76] *2021 Summary Tables*. URL: https://pdg.lbl.gov/2021/tables/contents_tables.html.

[77] Louise Heelan. *Calculating Efficiency Uncertainties*. URL: https://indico.cern.ch/event/66256/contributions/2071577/attachments/1017176/1447814/EfficiencyErrors.pdf.

[78] T. Ullrich and Z. Xu. *Treatment of Errors in Efficiency Calculations*. 2012. arXiv: physics/0701199 [physics.data-an].

[79] A. Hoecker et al. *TMVA - Toolkit for Multivariate Data Analysis*. 2009. arXiv: physics/0703039 [physics.data-an].

[80] Yann Coadou. *Boosted decision trees*. URL: https://indico.cern.ch/event/472305/contributions/1982360/attachments/1224979/1792797/ESIPAP_MVA160208-BDT.pdf.

[81] Mila Pandurović. *Measurement of Higgs decay to WW* in Higgsstrahlung at $\sqrt{s}$=500 GeV ILC and in WW-fusion at $\sqrt{s}$=3 TeV CLIC*. 2017. arXiv: 1703.08871 [hep-ex].

[82] H. Abramowicz et al. "Higgs physics at the CLIC electron–positron linear collider". In: *The European Physical Journal C* 77.7 (2017). ISSN: 1434-6052. DOI: 10.1140/epjc/s10052-017-4968-5. URL: http://dx.doi.org/10.1140/epjc/s10052-017-4968-5.